Technical Report
TR-99-13

Site-scale groundwater flow modelling of Ceberg

Douglas Walker
Duke Engineering & Services

Björn Gylling
Kemakta Konsult AB

June 1999

Svensk Kärnbränslehantering AB
Swedish Nuclear Fuel
and Waste Management Co
Box 5864
SE-102 40 Stockholm Sweden
Tel 08-459 84 00
+46 8 459 84 00
Fax 08-661 57 19
+46 8 661 57 19

ISSN 1404-0344
CM Gruppen AB, Bromma, 1999

Site-scale groundwater flow modelling of Ceberg

Douglas Walker
Duke Engineering & Services

Björn Gylling
Kemakta Konsult AB

June 1999

Keywords: Canister flux, computer modelling, F-ratio, groundwater flow, Monte Carlo simulation, repository, stochastic continuum, SR 97, travel time.

Abstract

The Swedish Nuclear Fuel and Waste Management Company (SKB) SR 97 study is a comprehensive performance assessment illustrating the results for three hypothetical repositories in Sweden. In support of SR 97, this study examines the hydrogeologic modelling of the hypothetical site called Ceberg, which adopts input parameters from the SKB study site near Gideå, in northern Sweden. This study uses a nested modelling approach, with a deterministic regional model providing boundary conditions to a site-scale stochastic continuum model. The model is run in Monte Carlo fashion to propagate the variability of the hydraulic conductivity to the advective travel paths from representative canister locations. A series of variant cases addresses uncertainties in the inference of parameters and the model of conductive fracture zones. The study uses HYDRASTAR, the SKB stochastic continuum (SC) groundwater modelling program, to compute the heads, Darcy velocities at each representative canister position, and the advective travel times and paths through the geosphere.

The Base Case simulation takes its constant head boundary conditions from the deterministic regional scale model of Boghammar et al. (1997). The volumetric flow balance between the regional and site-scale models suggests that the nested modelling and associated upscaling of hydraulic conductivities preserve mass balance only in a general sense. In contrast, a comparison of the Base and Deterministic (Variant 4) Cases indicates that the upscaling is self-consistent with respect to median travel time and median canister flux. These suggest that the upscaling of hydraulic conductivity is approximately self-consistent but the nested modelling could be improved. The Base Case yields the following results for a flow porosity of $\varepsilon_f = 1\times10^{-4}$ and a flow-wetted surface area of $a_r = 0.1$ m^2/(m^3 rock):

- The median travel time is 1720 years.
- The median canister flux is 3.27×10^{-5} m/year.
- The median F-ratio is 1.72×10^{6} years/m.

The Base Case and the Deterministic Variant suggest that the variability of the travel times within individual realisations is due to the position of the hypothetical canisters relative to the discharge areas, rather than to the spatial variability of the host rocks. Consequently, the variability between realisations is comparatively low. The flow patterns, travel times and simulated heads appear to be consistent with on-site observations and simple scoping calculations. The study uncertainties are addressed by a series of variant cases that evaluate the sensitivity of the results to changes in assumptions regarding the structural model and the hydraulic conductivities. The performance measures are most sensitive to highly conductive features such as fracture zones or intrusive dykes, particularly if such features directly intersect the waste canisters. The regional models for variant cases with highly conductive features have large mass balance residuals that are attributed to post-processing interpolation.

Sammanfattning

SR 97 är en säkerhetsanalys av tre hypotetiska djupförvar i Sverige. Denna rapport, utförd som en del av SR 97, beskriver den hydrogeologiska modelleringen av Ceberg. Ceberg är en hypotetisk plats där indata och parametrar baseras på förhållanden vid en plats där SKB utfört undersökningar i närheten av Gideå, som är beläget i norra Sverige. I den här beräkningsstudien har en nästlad modellering använts där en deterministisk regional modell ger randvillkor till en stokastisk kontinuum modell i platsskala. Monte Carlo simulering har använts för att propagera variabiliteten i hydraulisk konduktivitet till advektiva partikelbanor som utgår från representativa kapselpositioner. I en serie varianter har osäkerheter vid tolkandet av parametrar och överförandet av randvillkor analyserats. För att beräkna tryck, Darcy-hastigheter (specifkt flöde) vid kapselpositioner, advektiva gångtider samt partikelbanor genom geosfären har SKB:s stokastiska kontinuumprogram för grundvattenmodellering, HYDRASTAR, använts.

I basfallet har randvillkor i form av tidsoberoende tryck från en deterministisk regional modell (Boghammar et al., 1997) använts. Överensstämmelsen i flödesbalanserna mellan den regionala modellen och modellen i platsskala indikerar att den nästlade modelleringen och den därvid använda uppskalningen av hydrauliska konduktiviteter endast bevarar massbalansen i en generell mening. En jämförelse mellan basfallet och det deterministiska fallet indikerar emellertid att uppskalningen av hydrauliska konduktiviteter ger konsistenta resultat för medianvärden av gångtider och specifkt flöde vid kapselpositioner. Detta indikerar att uppskalningen approximativt ger det eftersträvade resultatet, men att den nästlade modelleringen kan förbättras. Resultaten för basfallet ger mätetal för förvarsfunktionen i Ceberg enligt följande när flödesporositeten $\varepsilon_f = 1\times10^{-4}$ och flödesvätta ytan $a_r = 0.1$ $m^2/(m^3$ rock) används:

- Medianen för gångtiderna är 1720 år
- Medianen för specifkt flöde vid kapselpositioner är 3.27×10^{-5} m/år
- Medianen för F-faktorn är 1.72×10^{6} år/m

Basfallet och den deterministiska varianten indikerar att variabiliteten i gångtider inom en enskild realisering beror av läget på den hypotetiska kapseln relativt utströmningsområden snarare än den rumsliga variabiliteten i det omgivande berget. Därmed blir variabiliteten i de beräknade mätetalen mellan olika realiseringar förhållandevis låg. Flödesmönstren, gångtider och simulerade tryck är i överensstämmelse med observationer gjorda på platsen och med förenklade överslagsberäkningar. Osäkerheter i studien behandlas genom att utföra en serie av varianter för att utröna känsligheten i resultat relaterat till ändringar i strukturmodellen och konduktivitetsvärden. Mätetalen för förvarsfunktionen påverkas i hög grad av förekomst av högkonduktiva strukturer i form av sprickzoner eller intrusioner, speciellt om dessa strukturer träffar kapselpositioner. De regionala modellerna för de variationsfall där konduktiviteten har ökats för strukturerna är behäftade med stora residualer i massbalanserna. Residualerna uppkommer i efterbehandlingsprocessen där massbalanserna uppskattas genom interpolation.

Contents

List of Figures

List of Tables

1 Introduction

1.1 SR 97

Swedish Nuclear Fuel and Waste Management Company (SKB) is responsible for the safe handling and disposal of nuclear wastes in Sweden. This responsibility includes conducting studies into the siting of a deep repository for high-level nuclear waste. The Safety Report 1997 (SR 97) will present a comprehensive performance assessment (PA) of the long-term safety of three hypothetical repositories in Sweden. The PA of each repository will include geosphere modelling to examine groundwater flow in the repository and the possible transport of radionuclides from the emplaced waste packages through the host rock to the accessible environment. The hypothetical repositories, arbitrarily named Aberg, Beberg and Ceberg, take their data from sites previously investigated by SKB.

This report is one of three SR 97 reports regarding site-scale groundwater flow modelling. Walker and Gylling (1998) presents a similar study for the Aberg hypothetical repository, and Gylling et al. (1999b) presents another similar study for the Beberg hypothetical repository.

1.2 Study Overview

This report presents the groundwater flow modelling study of the Ceberg hypothetical repository. The Ceberg site adopts input parameters from Gideå in northern Sweden, a site previously investigated by SKB. Walker et al. (1997b) summarises the site characterisation studies at Äspö and presents several possible representations for the site hydrogeology. This study applies a nested modelling approach to Ceberg, with a deterministic regional model providing boundary conditions to a site-scale stochastic continuum model. The model is run in Monte Carlo fashion to propagate the variability of the hydraulic conductivity to the advective travel paths from representative canister locations. A series of variant cases address uncertainties in the inference of parameters and the model of fracture zones.

The study uses HYDRASTAR, the SKB stochastic continuum (SC) groundwater modelling program, to compute the heads, Darcy velocities at each representative canister position, and the advective travel paths through the geosphere. The tasks involved in applying HYDRASTAR to Ceberg include the interpretation of the hydrogeologic model into HYDRASTAR format, upscaling of parameters, simulation and sensitivity analysis, interpretation and illustration of results, and summary reporting. The report is organised into the following sections:

Sections 1 and 2 introduce SR 97 and the methods used in this study.

Section 3 describes the hydrogeologic interpretation of the Ceberg data, and any adjustments to these data relative to previous reports.

Section 4 presents the Base Case simulation and examines several individual realisations and starting positions in detail.

Section 5 presents the variant case simulations.

Section 6 summarises and discusses the study results.

Appendix A defines the summary statistics.

Appendix B summarises additional regional model calculations specific to this study.

Appendix C presents supplemental calculations for rescaling, geostatistical inference and scoping calculations for travel times.

Appendix D summarises all input parameters used in this report.

Appendix E documents the data sources and data deliveries (e.g., SICADA log files for downloading the borehole data).

Appendix F summarises the additional software used in this study for statistical analysis, error checking and graphical display.

Appendix G presents the HYDRASTAR main input file used for the Base Case simulations in this study.

Appendix H documents the coordinate transforms used in this study and in Munier et al. (1997).

2 Modelling Approach

This study uses a stochastic continuum model of the fractured crystalline host rocks to analyse the groundwater flow and advective flow paths. Geostatistical analysis of hydraulic test data is used to infer a model of spatial correlation for the hydraulic conductivity of the site. Geostatistical simulation is used to create hydraulic conductivity fields for a numerical groundwater flow model, which provides groundwater velocities and stream tubes (flow paths) from the hypothetical waste canisters (Neuman, 1988). The model is run in Monte Carlo fashion for a large number of simulated hydraulic conductivity fields to create an ensemble of possible stream tubes and Darcy groundwater velocities at the representative canister positions (canister fluxes). Separate reports address the subsequent use of these stream tubes and fluxes in transport and biosphere modelling.

The site-scale HYDRASTAR model requires a model domain of adequate grid density to represent the known fractures and adequate extent so that the model reflects the regional flow conditions. These conflicting requirements force this study to adopt a nested modelling approach, with the site-scale model taking its boundary conditions from a regional scale model. This permits the site-scale model to use a relatively dense grid while incorporating the regional flow patterns through constant head (Dirichlet) boundaries on the site-scale domain (Ward et al., 1987). The Base Case and several variants examine this nested approach and the resulting mass balances across the site-scale boundaries.

This study uses SKB's Convex 220 computer to run the HYDRASTAR version 1.7.2 code under a strict source code control system. Several additional SKB programs are used for pre- and post-processing of HYDRASTAR input and output. These include INFERENS, a geostatistical analysis and inference program that is used to regularise the variogram of the data to the model scale; TRAZON, which verifies the stream tube starting positions versus the fracture zones; and HYDRAVIS, a graphical post-processor developed from the commercial software package AVS. The commercial software package STATISTICA post-processes and summarises the statistics of HYDRASTAR output. These pre- and post-processing programs are summarised in Appendix F.

2.1 The PA Model Chain

The software tool for the geosphere portion of the safety analysis consists of a chain of PA models, HYDRASTAR – COMP23 – FARF31 – BIO42, developed by SKB for use as a computational tool in the 1995 SKB safety analysis project (SR 95). The end product of the PA model chain is the calculation of the probable dose to the biosphere (Figure 2.1-1). This modular approach allows each component of the repository system to be studied separately, with the results combined at the finish to evaluate the performance. The hydrogeologic model, HYDRASTAR, determines the Darcy groundwater velocities at each stream tube starting position (canister flux) and the advective travel paths through the geosphere. COMP23 is the near-field model, which uses the canister fluxes to determine the release rate for radionuclides from the representative canisters and into the groundwater flow system. FARF31 uses the release rates from the representative canisters and the travel paths through the groundwater flow system to determine the radionuclide flux through the geosphere. BIO42 is the biosphere module, which takes the radionuclide fluxes from the geosphere and determines the dose to potential receptors (SKB, 1996a). Monte Carlo simulations of the PA chain address uncertainty in the input parameters (e.g., hydraulic conductivity, porosity, etc.).

Note that this report presents only the hydrogeologic modelling study, and consequently discusses only the HYDRASTAR portion of the PA model chain.

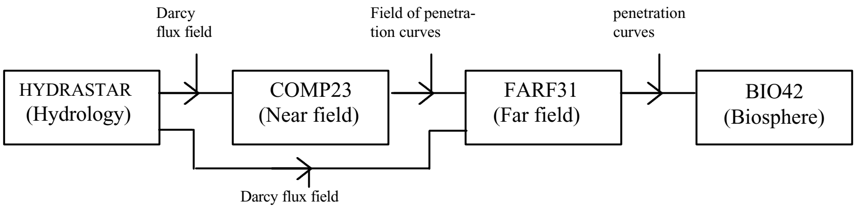

Figure 2.1-1. SKB PA model chain.

2.2 HYDRASTAR

HYDRASTAR is a stochastic groundwater flow and transport modelling program developed as a quantitative tool for support of the SKB 91 safety analysis project (SKB, 1992). A flow chart summarising the HYDRASTAR algorithm is presented in Figure 2.2-1. The current version, 1.7.2, uses the Turning Bands algorithm (Journel and Huijbregts, 1978) to generate realisations of the hydraulic conductivity field conditioned on the observed hydraulic conductivities. Trends in the data may be included implicitly through the use of ordinary kriging neighbourhoods or prescribed explicitly for specific regions. Hydraulic conductivity measurements at the borehole scale are upscaled to the model calculation scale using a regularisation scheme based on Moye's formula (a corrected arithmetic mean of the packer test hydraulic conductivities within a block; see Norman, 1992a, for details). HYDRASTAR uses the governing equation for either time-dependent or steady-state groundwater flow in three dimensions, assuming constant density. The solution to this governing equation is approximated by a node-centred finite-difference method to create a linear system of equations. A pre-conditioned conjugate-gradient algorithm solves the system of equations to arrive at a solution for the hydraulic head at each node. The pilot point inverse method (de Marsily et al., 1984) can be used to calibrate the input hydraulic conductivity field to minimise the error between the simulated and observed hydraulic heads. Transport in the resulting velocity field is modelled as pure advection using a particle tracking scheme. The process of conditional geostatistical simulation of hydraulic conductivity, calibration via inverse modelling, and particle tracking can be repeated in Monte Carlo fashion to develop empirical probability distributions for the hydraulic conductivity field, and the travel paths and arrival times for advected contaminants (SKB, 1996b).

Starprog AB developed and tested the code under contract to SKB, beginning in 1989 (Norman 1991 and 1992a). Various authors have contributed to the development and testing of the code, most notably Norman (1991 and 1992a); Morris and Cliffe (1994); Lovius and Eriksson (1993, 1994); Walker et al. (1997a); and Walker and Bergman (1998). The test problems include comparisons to well-known analytical and numerical solutions, or are taken from the HYDROCOIN series of test problems (OECD, 1983; Hodgkinson and Barker, 1985). The code also has been applied successfully to the Finnsjön site, as part of the SKB 91 Project (Norman, 1992a and SKB, 1992).

This study does not make use of all the available features in the current version of HYDRASTAR. Conditional geostatistical simulation using borehole data is not used. The Moye’s formula upscaling of borehole data is only used as part of INFERENS analysis of the data to infer a variogram model. Trends in the hydraulic conductivity are included only as discrete, stepwise changes to represent fracture zones and rock units (i.e., no use of a continuous function as a model of decrease in hydraulic conductivities with depth). The calibration algorithm is not used, nor is the transient simulation of pumping tests.

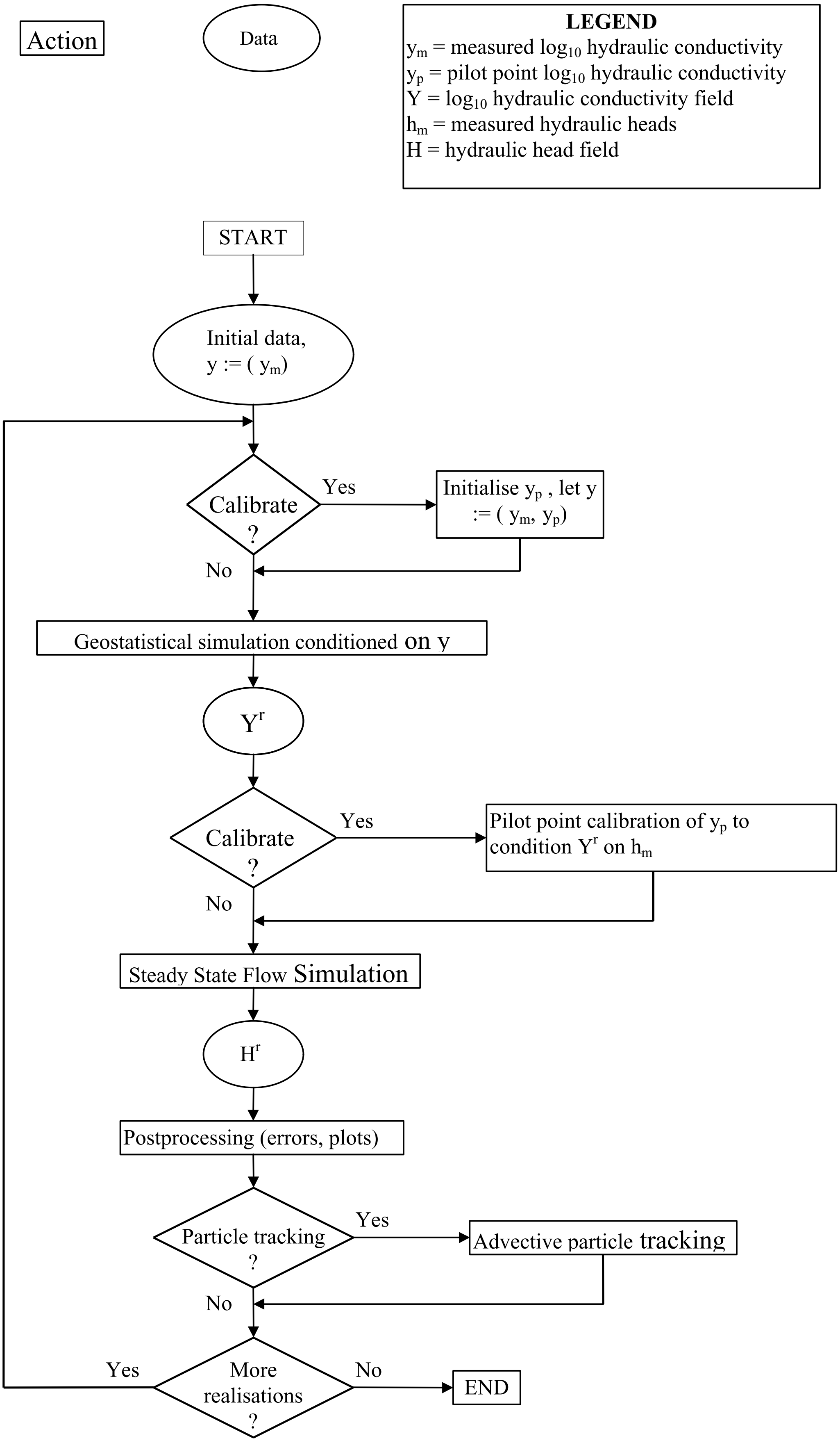

Figure 2.2-1. *HYDRASTAR version 1.7 flow chart. Superscript 'r' denotes realisation.*

2.3 Development of Modelled Cases

In addition to data analysis, computer simulation, and post-processing of results, the modelling process also requires that a set of relevant cases be analysed. In practice, expert judgement determines which assumptions to test and which uncertainties to evaluate. This results in a Base Case that represents the expected site conditions, and several variation cases that assess the uncertainty of inferences and assumptions. For this study, a separate group of scientists was convened by SKB, consisting of:

- Johan Andersson, Golder Grundteknik KB;
- Sven Follin, Golder Grundteknik KB;
- Jan-Olof Selroos, SKB;
- Anders Ström, SKB; and
- Douglas D. Walker, INTERA KB / Duke Engineering & Services.

This group met several times between November 1997 and March 1998, to discuss the reasoning behind the modelling assumptions, the derivation of model parameters and the modelling uncertainties. These discussions resulted in the parameters and assumptions that constitute the Base Case and variant cases addressed in this report.

3 Model Application

Walker et al. (1997b) summarises the hydrogeology of the site and proposes a series of preliminary parameter sets for the base (expected) variant cases. In addition to these parameter sets, HYDRASTAR also requires a geostatistical description of the hydraulic conductivity that is appropriate for the grid scale of interest. Appendix C presents additional computations for rescaling hydraulic conductivities and the inference of additional geostatistical parameters. Where possible, input parameters describing the repository layout, structural model, hydraulic conductivities, etc. are taken directly from SICADA or the authors of the respective reports (See Appendices D and E).

The site-scale HYDRASTAR model also requires a model domain of adequate extent and boundary conditions that reflect the regional flow conditions. This modelling study uses a nested modelling approach, taking the boundary conditions of the site-scale model from a much larger regional scale model. Appendix B summarises the specific regional model simulations used to generate the boundary conditions for the local scale model. The extent of the model domain was evaluated as part of preliminary modelling studies (Gylling et al., 1999a).

The following sections describe the application of HYDRASTAR to the Ceberg site, including the hydrogeologic conditions and modelling assumptions.

3.1 Site Description

Ceberg is modelled after the Gideå site, located in northern Sweden in the northern part of Ångermanland. The site is approximately 8 km inland from the Baltic Sea (Figure 3.1-1). The area corresponds to LMV map sheet 19J NV Husum and parts of sheets 20J SV and 19I NO. From a hydrogeologic perspective, the region is characterised by a strong topographic relief, ranging from sea level to over 300 masl. This creates a regional groundwater flow pattern of recharge in the upland areas and discharge to streams in the fault valleys. This dominant flow pattern also contributes to the low salinity in the site. Another notable characteristic of the site is the low hydraulic conductivity at repository depth in comparison to other sites studied by SKB.

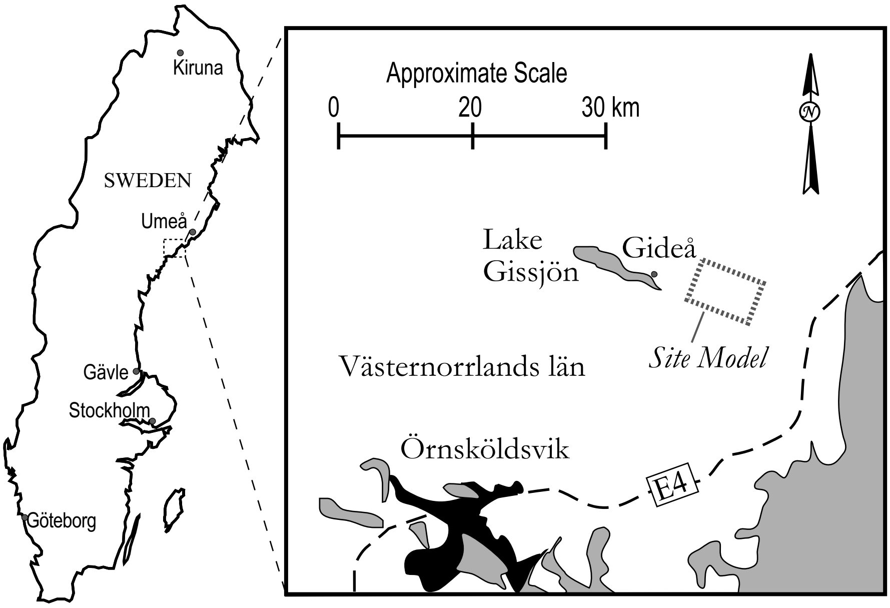

Figure 3.1-1. *Location of the Gideå site. Dashed line represents roads.*

3.2 Hydrogeology

The geology and hydrogeology of the Gideå site have been studied in detail and are summarised in a series of reports (Ahlbom et al., 1991; Ahlbom et al., 1983; Hermanson et al., 1997; Askling, 1997; Timje, 1983). Walker et al. (1997b) presents a summary of site conditions emphasising continuum modelling.

The bedrock in the Gideå region is migmatised-veined gneiss, dominated by greywacke with subordinate schist, phyllite and slate with varying degrees of metamorphosis. Dolerite intrusive dykes are common in the region and have been observed at the site, typically as subvertical thin dykes with east-west strikes. South of the Gideå site is a body of granite gneiss and to the west is a body of granite (Hermanson et al., 1997). The region continues to experience isostatic rebound as a consequence of the last period of continental glaciation and exhibits landrise rates amongst the fastest in Sweden, approximately 7.7 mm/yr (Björck and Svensson, 1992). The soil cover is thin generally (less than a metre) with numerous bedrock outcrops, but is somewhat deepert in valleys and larger depressions. Glacial till occurs only sparsely at ground surface, and the soil cover is dominated by marine sediments. Peatlands are found in some depressions, as are wave-washed gravel and sand (Lundqvist et al., 1990).

Regional lineaments have been interpreted from air photos and topographical maps at a scale of 1: 50,000 (Ahlbom et al., 1983; Askling, 1997; Lundqvist et al., 1990). These lineaments have been interpreted as subvertical fractured zones, striking primarily west-northwest and northwest. In general, however, very little information is available for the regional lineaments, and their inferred characteristics should be regarded as uncertain (Ahlbom et al., 1983; Ericsson and Ronge, 1986; Askling, 1997; Hermanson et al., 1997). On site, a number of steeply dipping fracture zones has been observed, whose hydraulic conductivity is inferred to be somewhat higher than the surrounding rock mass.

The groundwater chemistry in the Gideå area is characterised by an overall downward recharge of precipitation, typical of upland areas with strong topographic drive (Laaksoharju et al., 1998).

Timje (1983) summarised the Swedish Meteorological and Hydrological Institute (SMHI) data and constructed a rainfall-runoff model for this region. The resulting simulations suggest that the mean annual net distributed recharge to the regional groundwater system is 10 mm, but may vary locally depending on topography. Timje (1983) constructed a water table map that indicates that the shallow groundwater system is dominated by recharge on the plateau and discharge to the streams that occupy fault valleys. The effects of this topographically driven system on the site-scale model are discussed in the next section.

3.3 Regional Model and Boundary Conditions

The model uses a nested modelling approach, relying on boundary conditions derived from the regional groundwater flow modelling study of Boghammar et al. (1997; Figure 3.3-1). That study used a finite element continuum model, NAMMU, to study ground water recharge and regional flow patterns. The results of that study included the steady-state heads along the limits of the site-scale model domain. Figure 3.3-2 presents the hydraulic heads estimated by the regional model on the boundaries of the site-scale model. The smaller regional model of Boghammar et al. (1997) provides the constant head boundary conditions for the Base Case site-scale model.

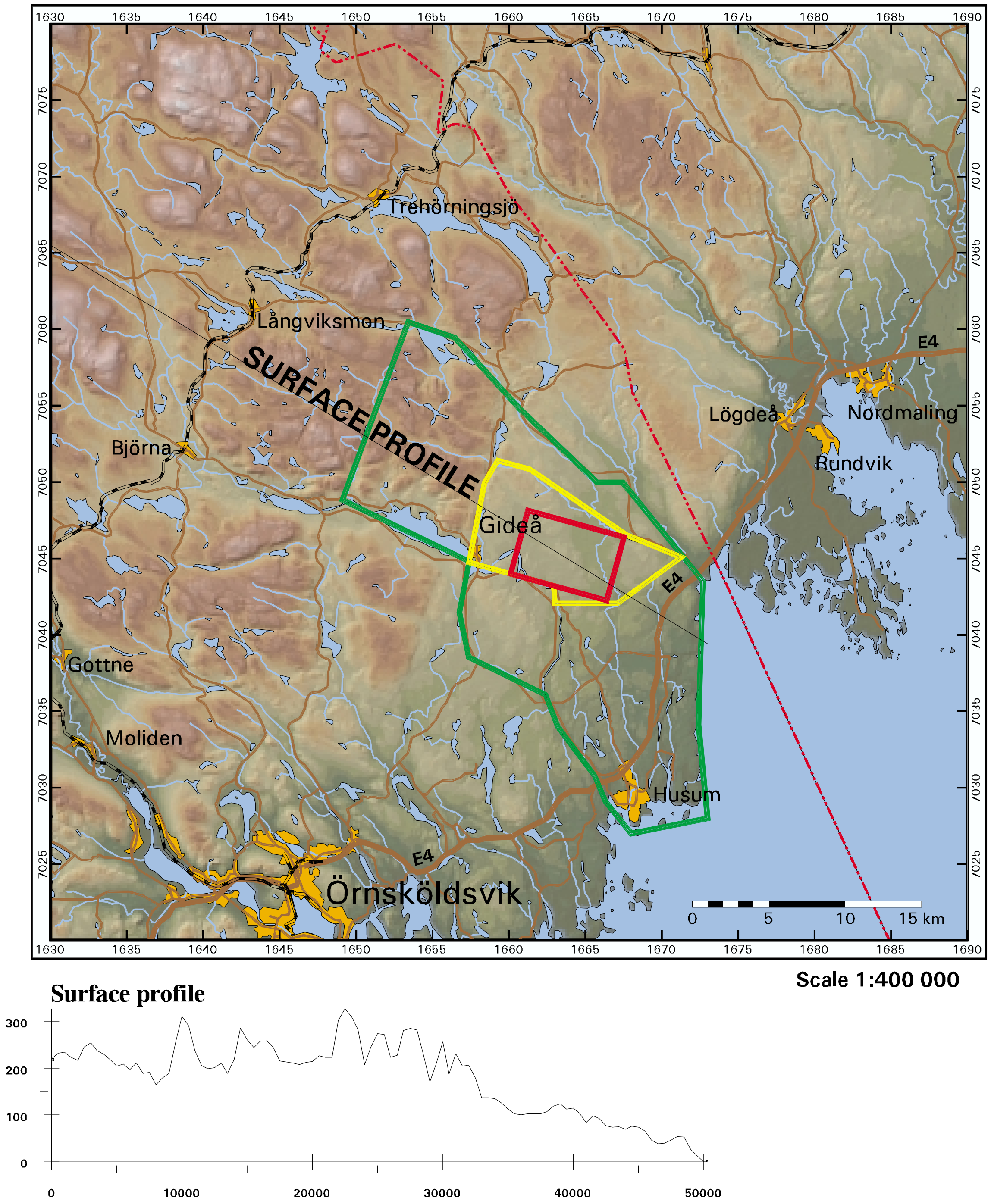

Figure 3.3-1. *Gideå site map, showing the large and small regional models of Boghammar et al. (1997) in green and yellow, respectively. The site-scale model is shown in red.*

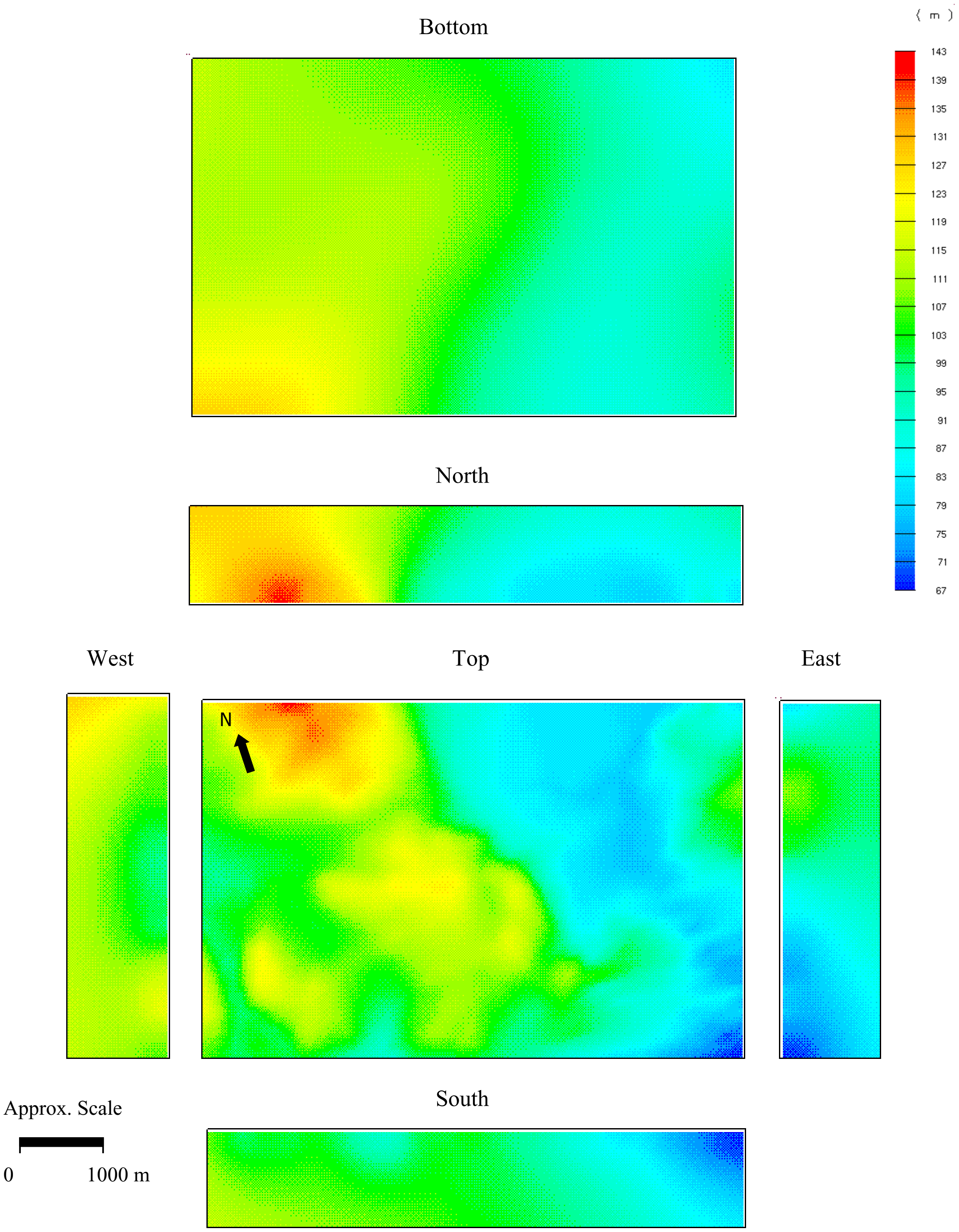

Figure 3.3-2. *Constant head boundary conditions for each face of the model domain for Ceberg (hydraulic head, in metres).*

Variant 1, with fracture zone conductivities increased by a factor 100, and Variant 2, with additional fracture zones, require slightly different regional models than the Base Case to generate appropriate site-scale boundary conditions. For Variant 1, an appropriate variant from Boghammar et al. (1997) is available to provide the constant head boundary conditions. For Variant 2, an additional simulation is performed, based on the regional model of Boghammar et al. (1997; see also Appendix B).

The heads predicted by the regional model along the boundaries of the site-scale model domain are used as Dirichlet (constant-head) boundary conditions for the site-scale model. The regional NAMMU model generates the head values using finite element basis functions to interpolate as necessary between the NAMMU nodes for the HYDRASTAR grid spacing of 35 m. A HYDRASTAR subroutine reads the interpolated heads and uses them as boundary conditions for the HYDRASTAR model domain. Although this approach is similar to that used in other nested groundwater models (e.g., Ward et al., 1987; Leake et al., 1998), it is also important to verify that the flows across the boundaries are the same (i.e., conservation of mass). The consistency of flow between the regional and site-scale model is discussed further in Section 4.0.

3.4 Model Grid and Repository Layout

The HYDRASTAR model for this application consists of a 3-dimensional finite difference grid with a uniform grid spacing of 35 m. The regional modelling study of Boghammar et al. (1997) examined the regional flow pattern to determine a model domain that would include the majority of exit locations for advective travel paths starting from the repository. Preliminary simulations by Gylling et al. (1999a) suggested that a small percentage (approximately 10%) of particles would fail to exit to the upper model surface and be intercepted by the southern model boundary. This application of HYDRASTAR uses a domain with an upper surface area of 6510 m by 4290 m, extending to a depth of 1190 m (Figure 3.4-1). The upper surface of the model is given 60 masl. The resulting grid of 187×124×35 nodes (width, length and depth, respectively) gives a relatively large size for HYDRASTAR models that can be run on the SKB CONVEX.

The performance assessment measures are based on distributions of canister flux, travel paths and travel times to exit locations in the accessible environment (i.e., ground surface). Ideally, the model grid upper surface would correspond to the ground surface. This is not possible in this study because HYDRASTAR uses a flat plane for the upper model surface. Consequently the observed ground surface is represented as a horisontal plane with the modelled domain lying below the minimum ground surface elevation (60 masl). The HYDRASTAR particle tracking algorithm requires a minimum distance of one grid spacing from any model boundary to calculate the velocity vectors, and thus the exit location for these simulations is 25 masl. That is, the performance assessment measures are based on exit locations on a horisontal plane at 25 masl.

Figure 3.4-1 also shows the hypothetical repository tunnel layout, a single-level design specified by Munier et al. (1997, recommended tunnel design). The tunnels of this repository design lie at an elevation of –500 masl, oriented perpendicular to the principal regional stress. The design avoids mapped fracture zones, allowing an exclusion zone whose width depends on the fracture zones' classification. The tunnels are placed no closer than 100 m to zones that are classified as certain (e.g., Zone 1), and no closer than 50 m to those classified as probable (e.g., Zone 7). Note that the tunnel design does not avoid fracture zones classified as possible, such as the dolerite dykes (see Section 5.2). This study represents the hypothetical waste canisters with 119 locations uniformly scattered over the repository tunnels (Figure 3.4-2). HYDRASTAR uses these 119 representative locations as starting positions for the stream tubes and the subsequent travel time, canister flux and F-ratio calculations.

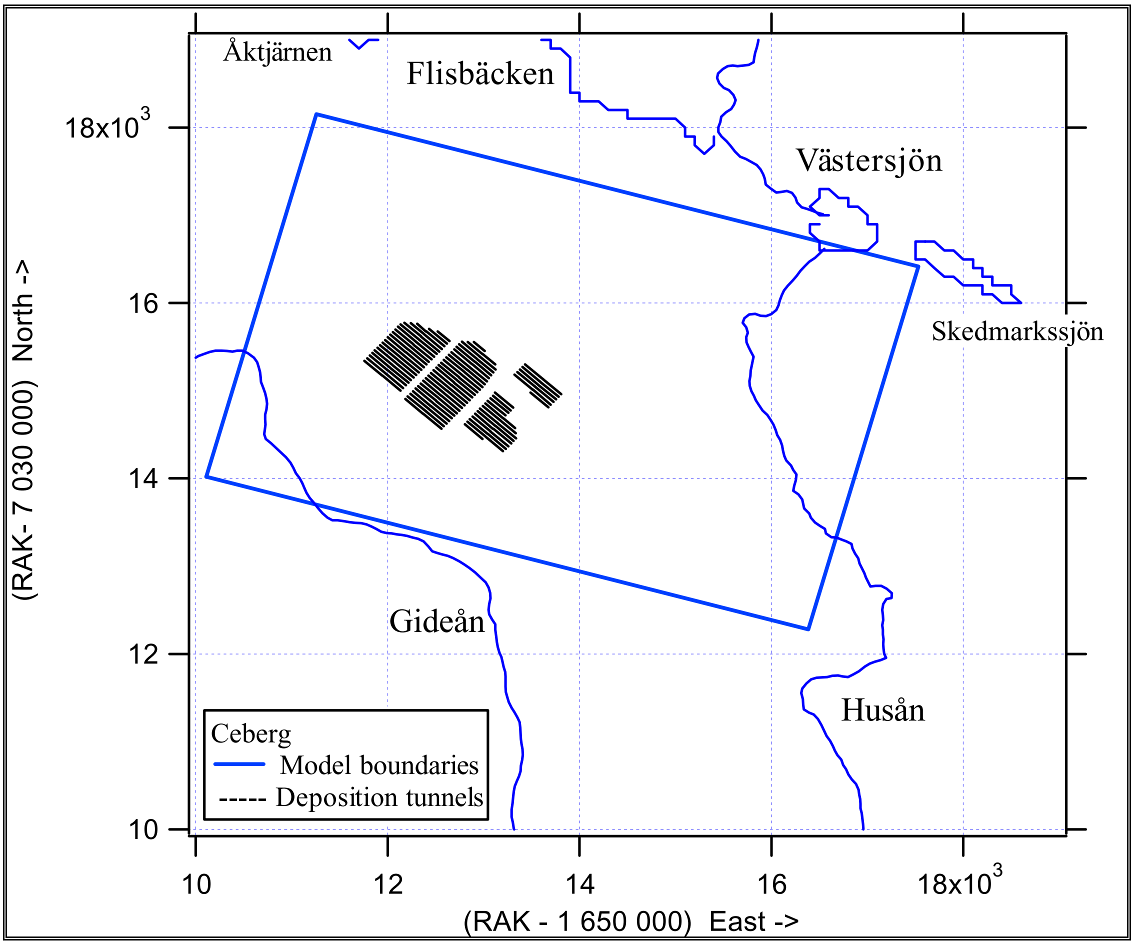

Figure 3.4-1. *Gideå site-scale model domain (blue line). Tunnels of the hypothetical repository at –500 masl are shown projected to ground surface (scale in metres).*

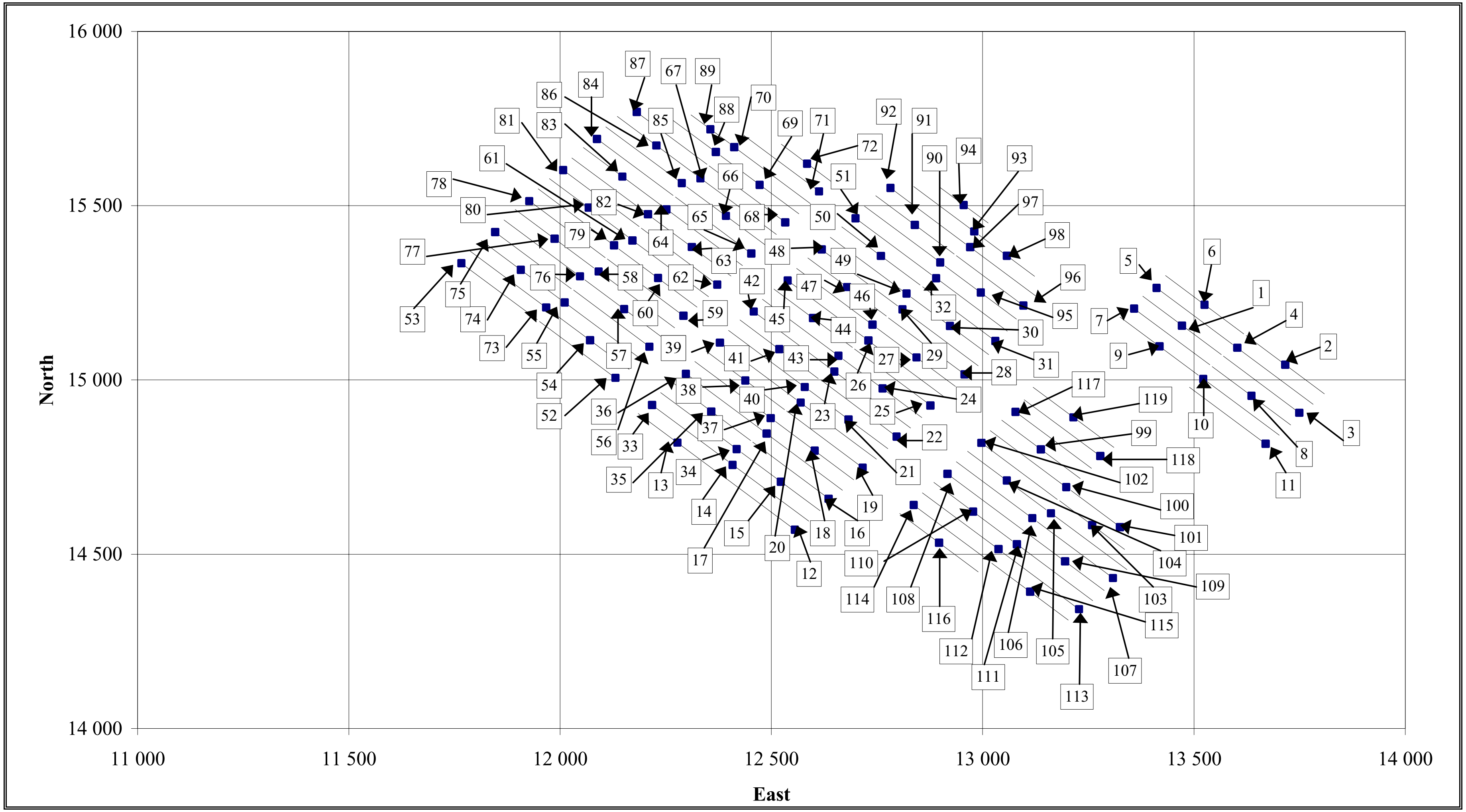

Figure 3.4-2. *Ceberg hypothetical repository tunnel layout at –500 masl. Numbered locations are 119 stream tube starting locations as representative canister positions.*

3.5 Input Parameters

HYDRASTAR's input parameters require a structural, hydraulic and geostatistical description of the site, all at an appropriate scale. This study uses the site-scale description based on hydrogeologic information found in Ahlbom et al. (1983), Timje (1983) and Walker et al. (1997b). The site investigations identified a number of relatively conductive fracture zones between 5 to 50 m in width. Preliminary reports by Ahlbom et al. (1983) and Ahlbom et al. (1991) suggested that some fractured zones are clay-altered with very low hydraulic conductivity, while others are highly conductive. Thus the assumption that the fracture zones are uniformly conductive features is uncertain at Ceberg. Fractures elsewhere in the site (i.e., those not included in the deterministic zones) are collectively included in the hydraulic conductivity estimates for the rock mass. Consequently, the hydraulic conductivity data are divided into two populations based on the site structural model (Walker et al., 1997b):

- Rock Domain (RD) – relatively unfractured rocks outside the deterministic conductors. On the site-scale, this is denoted SRD.

- Conductor Domain (CD) – fractured rocks within the deterministic conductors. On the site-scale, the set of conductors is collectively referred to as SCD.

The principal source of hydraulic conductivity data is the injection and pumping tests performed in the cored boreholes (Figure 3.5-1). These tests were interpreted and the measurements reported for various depths, rock types, etc. as described by Ahlbom (1983), Hermanson et al. (1997), and Walker et al. (1997b). The interpreted hydraulic conductivities for the 25 m packer tests were taken directly from the SKB SICADA database and analysed with the SKB geostatistical inference code INFERENS.

The scale of these measurements (as inferred from the packer length) is little different from the proposed model grid scale. However, as discussed in Walker et al. (1997b), hydraulic conductivity is a scale-dependent parameter, which requires that the measured hydraulic conductivities be upscaled to the finite difference grid scale of the model. This study uses the scaling approach described in Appendix C.1. The following sections present both the geometric means of the test-scale and model-scale hydraulic conductivities for the conductor domain and the rock domain.

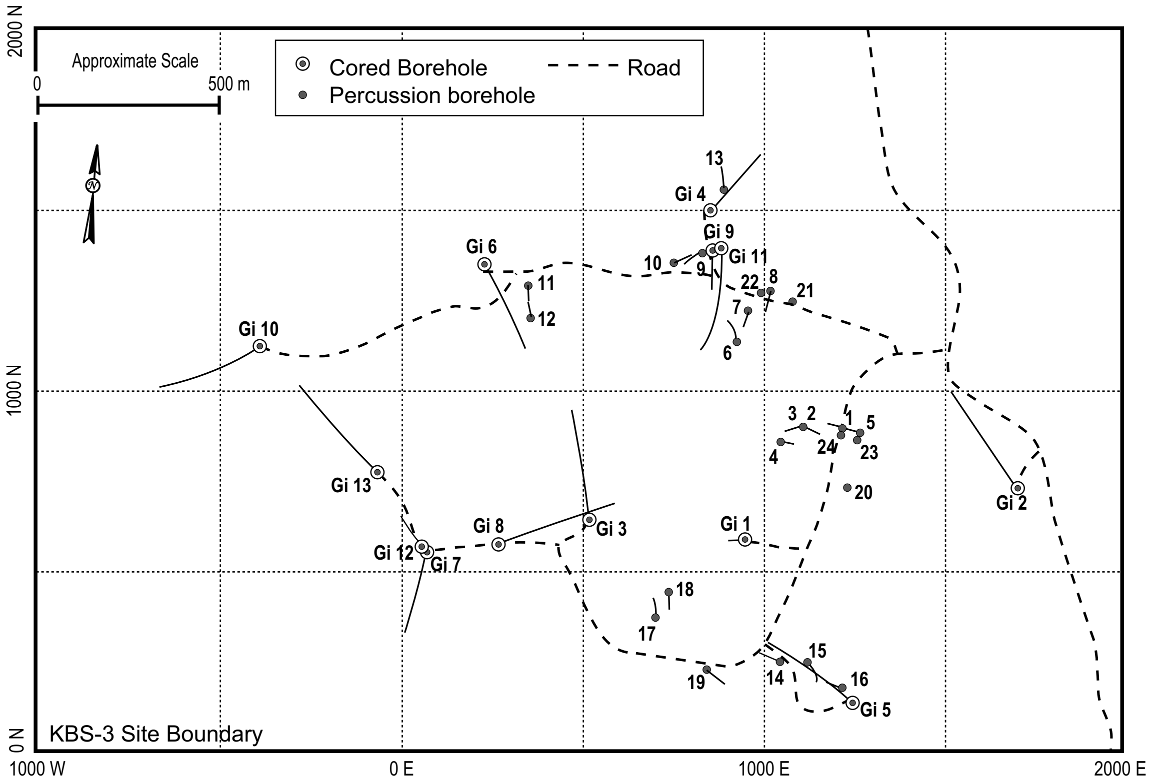

Figure 3.5-1. Gideå boreholes. Coordinates are a local system used in the KBS-3 study.

3.5.1 Site-Scale Conductor Domain (SCD)

The geometries of the hydraulic conductor domains on the site-scale (SCD) are defined by the major discontinuities described in Hermanson et al. (1997) and represented as planar features of constant width (Figure 3.5-2). Unlike Aberg and Beberg, only single-hole borehole tests have been performed at this site, with little additional examination of the individual conductive structures. Walker et al. (1997b) inferred a depth-dependant model of hydraulic conductivities, dividing the packer test data into a series of stepwise decreases with depth. Insufficient data are available to infer properties for individual fractures, so the $\log_{10}$ hydraulic conductivity of the fractures is assumed to come from a common distribution whose mean varies with depth. This study assumes that the measurement scale is 25 m, and correspondingly upscales the reported values to the finite difference block scale of 35 m using the relationship described in Appendix C.1. Table 3-1 presents the resulting parameter set, denoted SCD1 in Walker et al. (1997b).

Table 3-1. Depth dependence of hydraulic conductivity for Ceberg site-scale conductors (SCD1). Mean of 25 m $\log_{10}$ hydraulic conductivity (K) measurements from Walker et al. (1997b), scaled to 35 m.

Elevation (masl)	Arithmetic Mean Log_{10} K (m/s) at 25 m	Arithmetic Mean Log_{10} K (m/s) at 35 m
+110 to 0	–7.0	–6.9
0 to –100	–8.5	–8.4
–100 to –300	–9.5	–9.4
Below –300	–9.7	–9.6

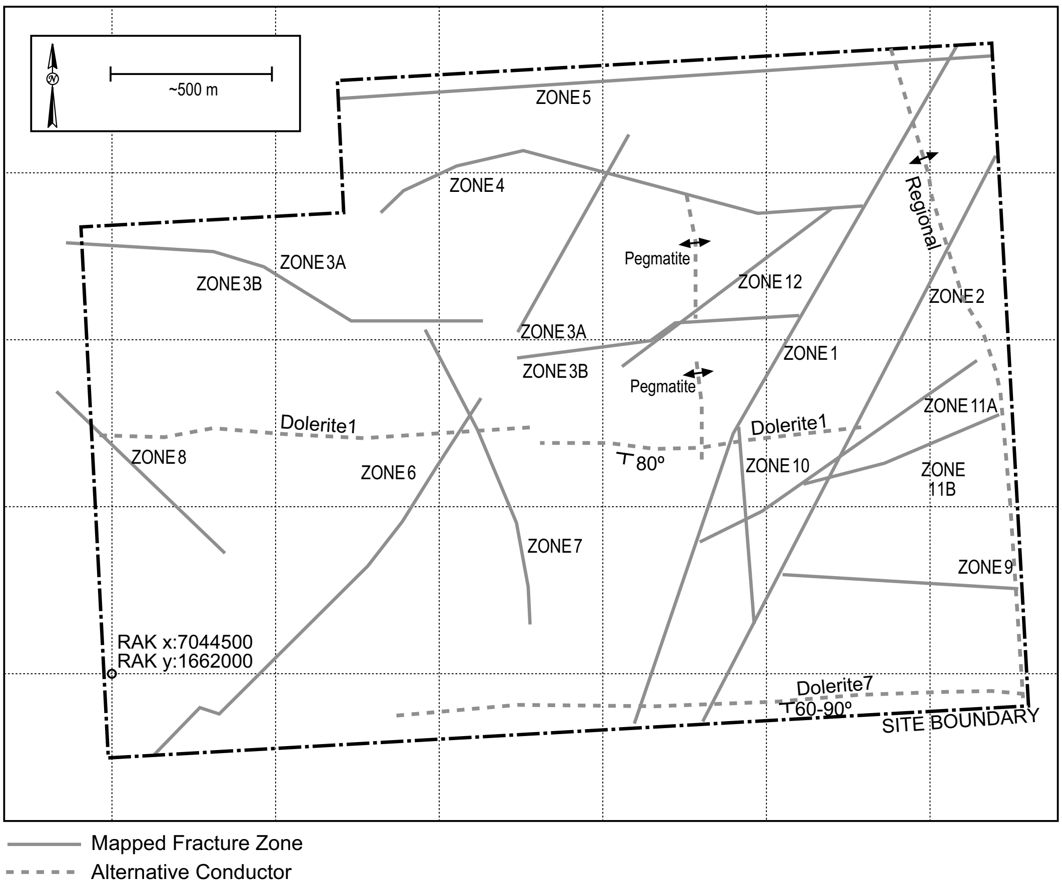

Figure 3.5-2. *Ceberg site-scale conductor domains (SCD) after Hermansson et al. (1997) and Saksa and Nummela (1998).*

3.5.2 Site-Scale Rock Domain (SRD)

Similar to the conductor domain, the rock domain on the site-scale (SRD) is divided into elevation zones as given by Walker et al. (1997b). The geometric mean hydraulic conductivities are based on the interpreted hydraulic conductivities of the 25 m packer tests. These values must be upscaled from 25 m-measurement scale to 35 m-finite difference grid scale. Table 3-2 presents the resulting parameter set, denoted SRD6 in Walker et al. (1997b), as the upscaled values used in this study.

Table 3-2. Depth dependence of hydraulic conductivity for Ceberg site-scale rock mass (SRD6). Mean of 25 m $\log_{10}$ hydraulic conductivity (K) measurements from Walker et al. (1997b), scaled to 35 m.

Elevation (masl)	**Arithmetic Mean Log_{10} K (m/s) at 25 m**	**Arithmetic Mean Log_{10} K (m/s) 35 m**
+110 to 0	–7.6	–7.4
0 to –100	–9.0	–8.9
–100 to –300	–10.0	–9.9
Below –300	–10.3	–10.1

3.5.3 Geostatistical Model

The Ceberg site-scale geostatistical model of hydraulic conductivity consists of depth zones for SRD6 and SCD1, the structural model of the zones and a single variogram model. As is discussed in Walker et al. (1997b), the variogram must be adjusted (regularised) to account for the difference between measurement and grid scales. Note that only one variogram model can be specified in HYDRASTAR for both domains. Because the data are most abundant for the rock domain, this study infers a regularised variogram model based on the upscaled 25 m packer test data in the rock domain SRD (Walker et al., 1997b). The interpreted conductivities are taken from 13 cored boreholes, as found in SICADA. The SKB code INFERENS was used to upscale the 25 m data to 50 m and fit a model variogram to the rock mass data (Walker et al., 1997b).

Linear interpolation between the 25 m and 50 m variogram suggests the following variogram model for the 35 m grid scale (Figure 3.5-3; see also Appendix C.1):

- Exponential model, isotropic,
- practical range of 68 m, and
- zero nugget, $\log_{10}$ K variance of 1.12.

The SRD and SCD are treated as step changes in K_b, the block conductivities (i.e., 0 order trends in $\log_{10} K_b$), with values provided in Tables 3-1 and 3-2. Figure 3.5-4 shows the representation of the SCD within the model domain, and Figure 3.5-5 is a deterministic realisation. Figure 3.5-6 is a plot of a single realisation (number 1) of the $\log_{10}$K field.

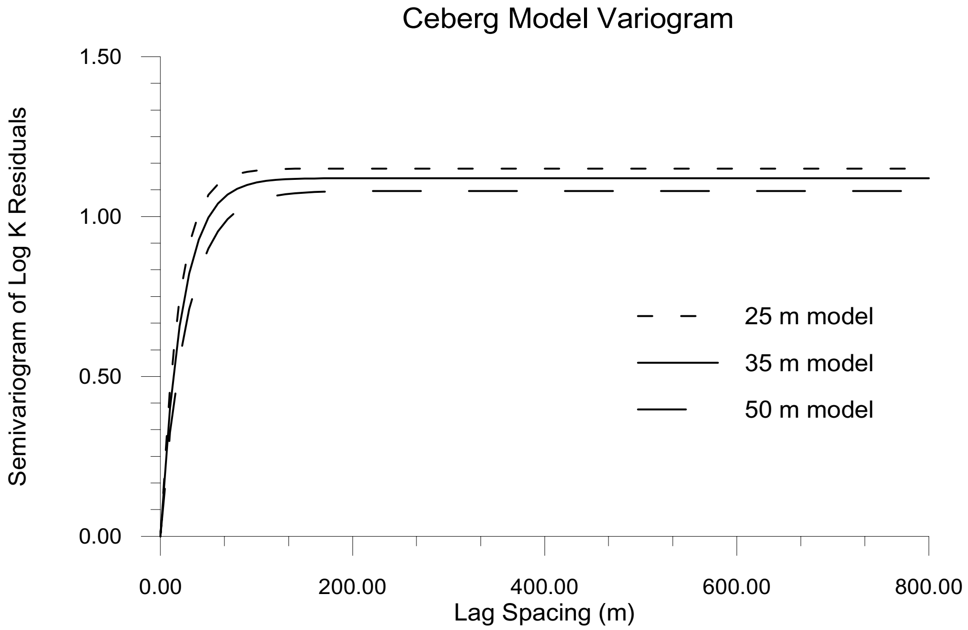

Figure 3.5-3. *Semivariograms of $\log_{10}$ hydraulic conductivity for Ceberg rock domain (SRD), for packer test data (25 m), INFERENS-fitted (50 m), and interpolated (35 m).*

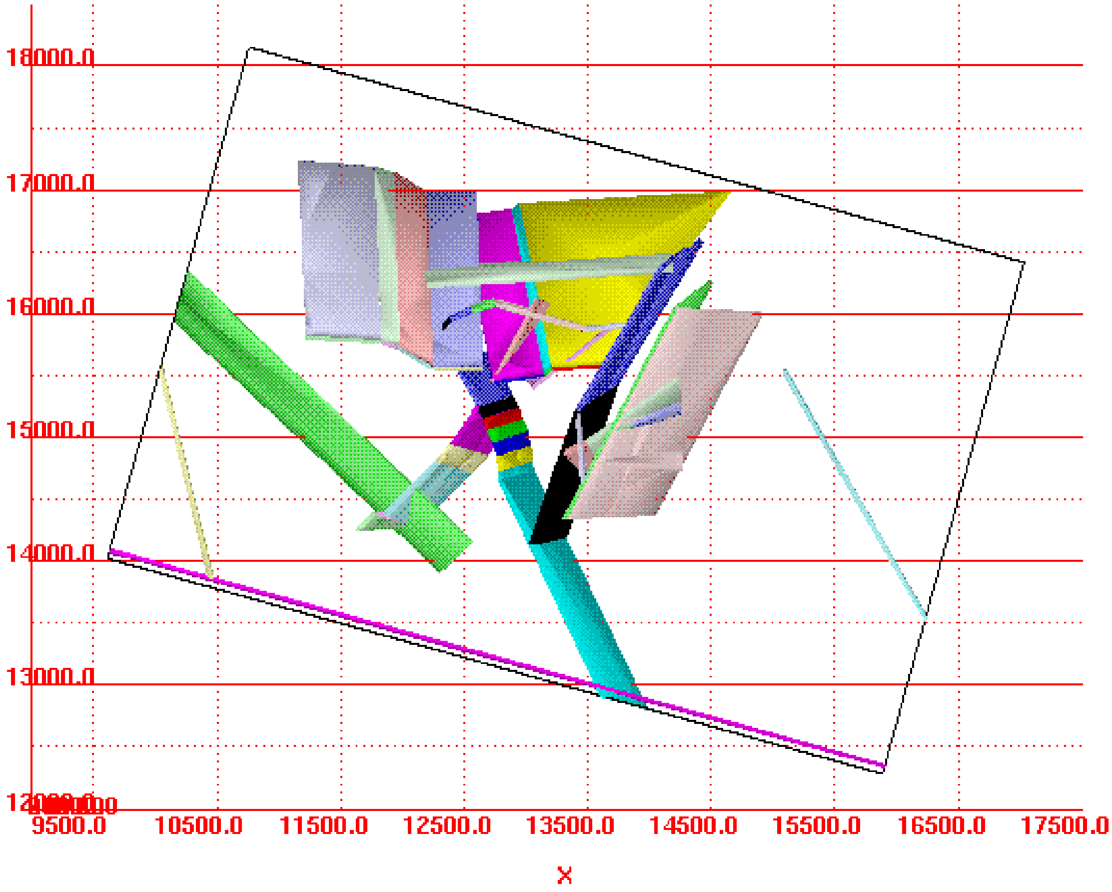

***Figure 3.5-4.** HYDRASTAR representation of Ceberg conductive fracture zones (SCD1). Coordinates are RAK system offset by 1,650,000 m in east-west and 7,030,000 m in north-south (view from above, with RAK North in the y-positive direction, scale in metres).*

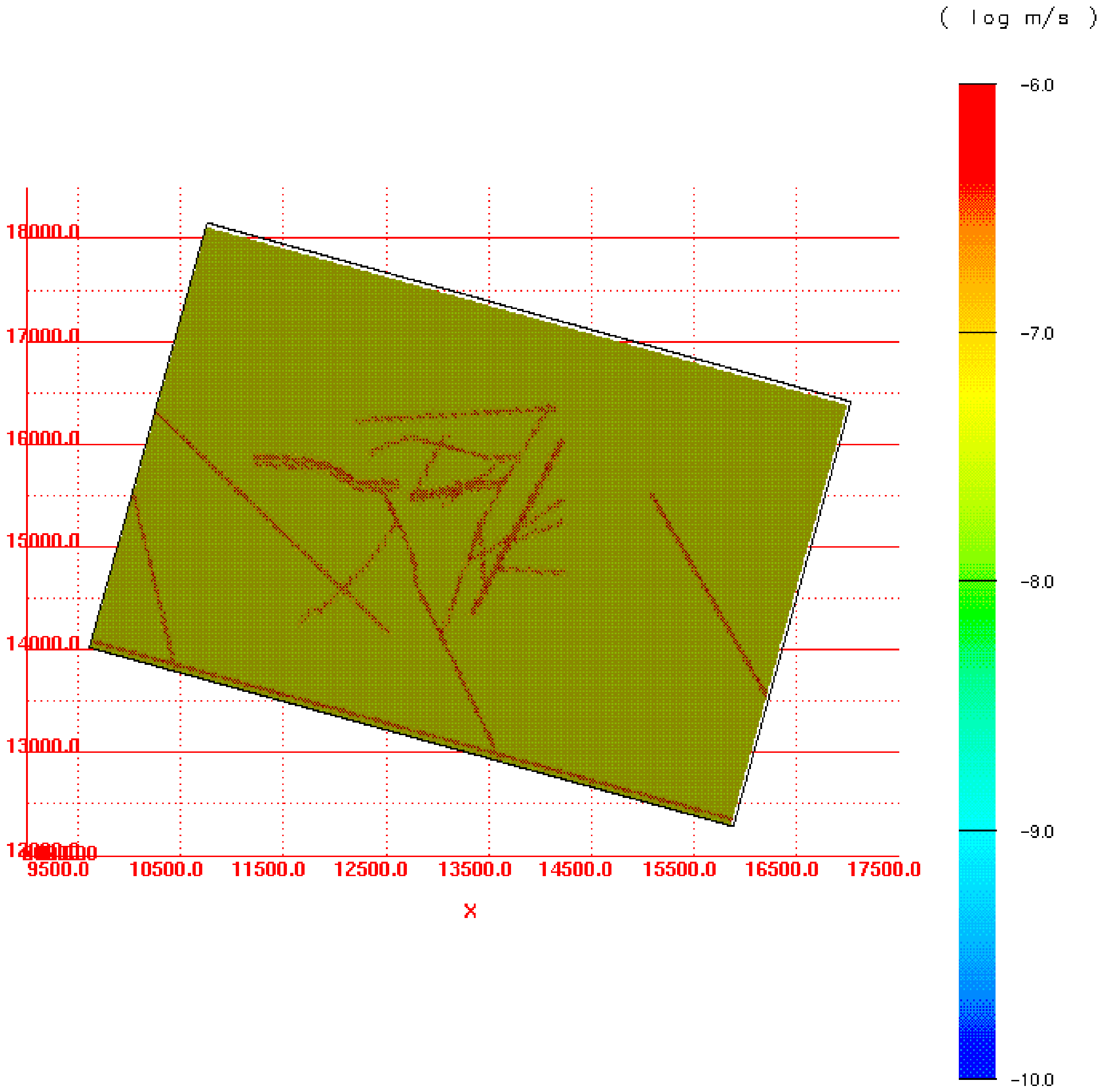

Figure 3.5-5. *Log$_{10}$ hydraulic conductivity on the upper model surface, Ceberg Variant 4 (deterministic representation of hydraulic conductivity, in plan view, with RAK North in the y-positive direction, scale in metres).*

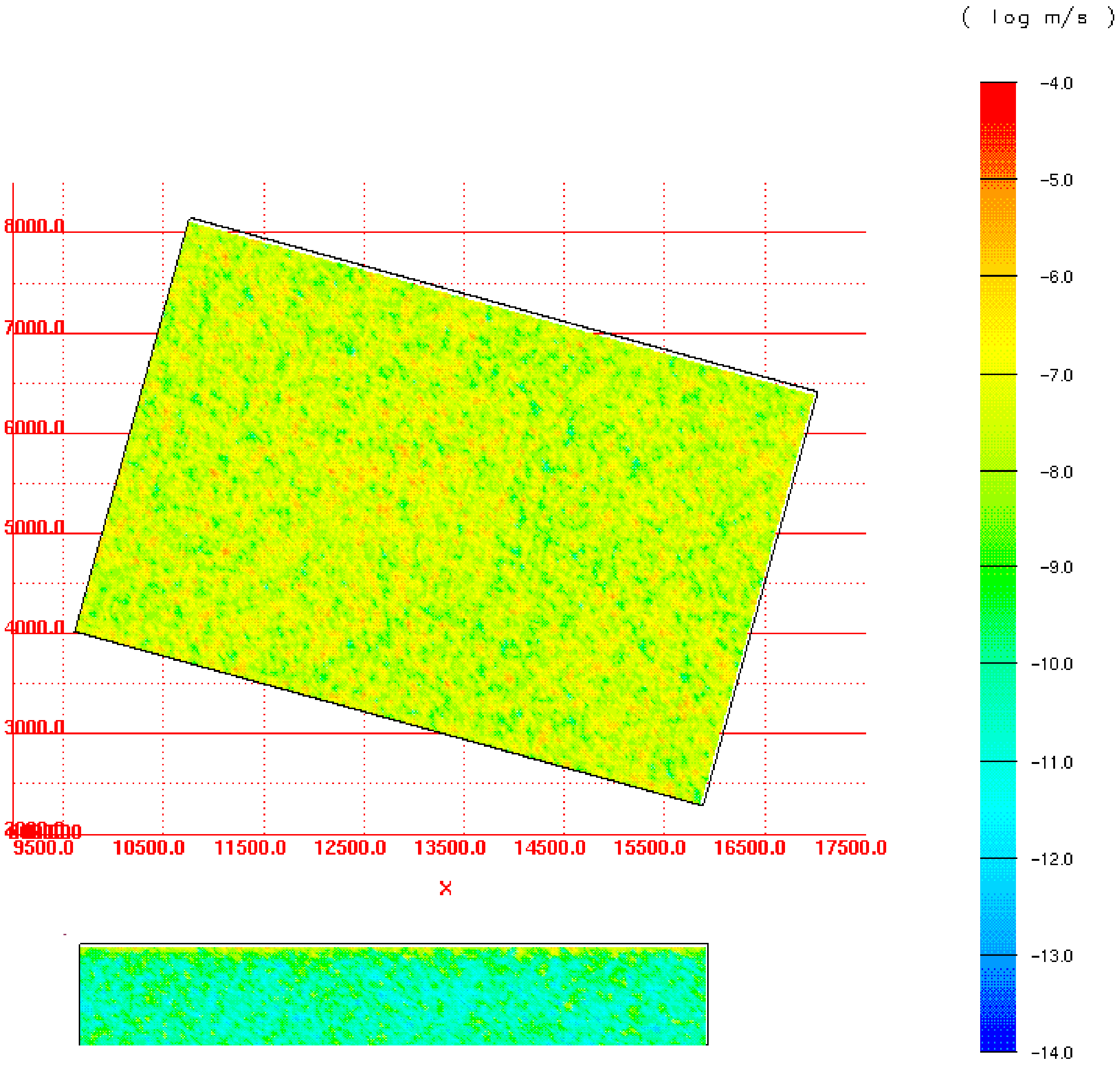

***Figure 3.5-6**. Log$_{10}$ of hydraulic conductivity for one realisation of Ceberg Base Case. Upper image is plan view, with North in the y-positive direction, scale in metres. Lower image is elevation view of the same field, looking North.*

3.5.4 Other Parameters

The remaining HYDRASTAR input parameters are hydraulic parameters required for the transport calculations and performance measures. One of these is the flow (or kinematic) porosity, ε_f, which is not easily characterised under the best of conditions. Based on analogue data at Äspö (Rhén et al., 1997), this study uses a flow porosity of $\varepsilon_f = 1\times10^{-4}$, uniform over the entire domain. It should be noted that the travel times reported in this study are directly proportional to this assumed flow porosity.

Another hard-to-define parameter is a_r, the flow-wetted surface area per rock volume. Similar to the flow porosity, the flow-wetted surface is assumed to be uniform over the entire model. For Ceberg, Andersson (1999) report a range of 1.0 to 0.01 and recommend the value $a_r = 0.1$ $m^2/(m^3$ rock) as the best estimate. This parameter is not used directly as model input for HYDRASTAR, but it is used in calculating the F-ratio, defined as:

$$F = \frac{d_w a_r}{q_w} = \frac{t_w a_r}{\varepsilon_f}$$

Where:

d_w = travel distance for a particle [metres]

q_w = Darcy velocity = $v \cdot \varepsilon_f$ [metres/year]

a_r = specific surface per rock volume for a travel path [$m^2/(m^3$ rock)]

ε_f = flow (kinematic) porosity [.]

The F-ratio [years / m] is a ratio of resisting to driving forces for transport, which has been used to compare model results in performance assessments (SKI, 1997). The F-ratio is useful in evaluating repository performance in the case of sorbing nuclides, where the transit time depends on both the surface area available for sorption and on the Darcy velocity. Although the F-ratio is calculated for all cases, it is a simple multiple of the travel time and is therefore plotted only for the Base Case. SR 97 uses the F-ratio to compare the geosphere performance for the three hypothetical repositories, where the flow-wetted surface varies from site to site.

4 Base Case

This section of the report presents the simulation and analysis for the Base Case, which represents the expected site conditions as described in Section 3, and it is the reference case for comparison to all other cases. A premodelling study by Gylling et al. (1999a) examined the extent of the domain and suggested a volume likely to contain all exit locations. Boundaries for this domain are specified head (Dirichlet) boundaries on all sides of the model domain, taken from the steady-state head values of a deterministic, freshwater simulation with the regional model of Boghammar et al (1997, case GRST). Mapped fracture zones are modelled as conductive features and included as deterministic conductor domains (SCD). The site-scale hydraulic conductivity field is created with an unconditional simulation (i.e., no direct use of measured hydraulic conductivities), prescribing the mean of $\log_{10}$ hydraulic conductivity for each rock unit.

One hundred realisations of the hydraulic conductivity field, each with 119 starting locations, are used to estimate the distributions of travel time and canister fluxes. All statistics are calculated with respect to the common logarithm transforms ($\log_{10}$) to facilitate summary and display. No formal test for the lognormality of these results has been performed or is inferred.

4.1 Monte Carlo Stability

A practical consideration in Monte Carlo simulation studies is that statistics of interest be stable with respect to the number of realisations. That is, the number of realisations should be adequate for reliable estimates of the results. This study monitored the stability of the estimators of the median travel time and median canister fluxes with respect to the number of realisations. Figures 4.1-1 and 4.1-2 present the medians of the logarithm of travel time and the logarithm of canister flux, respectively, versus the number of realisations. The plots indicate these statistics are approximately constant after 30 realisations, with less than 3% deviation for additional realisations. Thus, for the purposes of this study, a total number of 100 realisations were performed.

The stability of the sample median and arithmetic mean should not be taken to imply that higher moments such as the sample variance are also stable. Estimators of higher moments and the extreme quantiles of distributions are usually much less efficient than the median or the mean (Larsen and Marx, 1986). In general, estimating these moments with a similar degree of accuracy requires many more realisations than are needed for stable estimators of the median (Hammersley and Handscomb, 1975). Consequently, the higher-order statistics may not have stabilised and should be used cautiously.

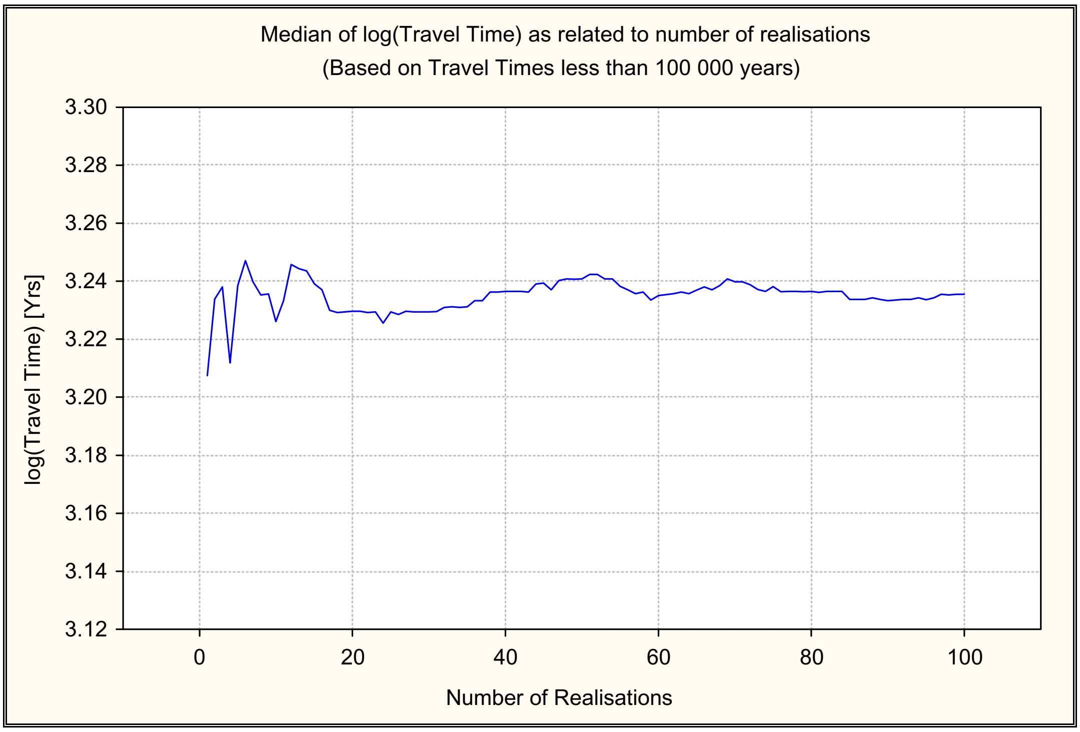

Figure 4.1-1. *Monte Carlo stability in the Ceberg Base Case. Median travel time versus number of realisations. Results are shown for 119 starting positions, a flow porosity of* $\varepsilon_f = 1\times10^{-4}$ *and travel times less than 100,000 years.*

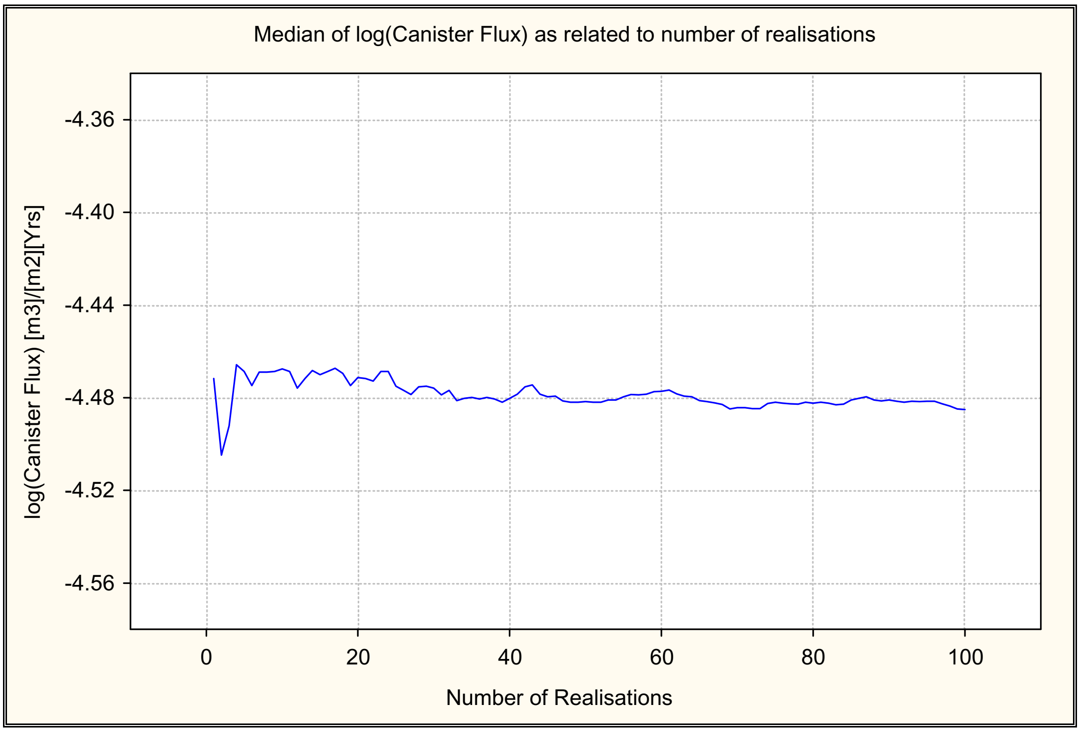

Figure 4.1-2. *Monte Carlo stability in the Ceberg Base Case. Median canister flux versus number of realisations. Results are shown for 119 starting positions.*

4.2 Boundary Flux Consistency

Stochastic continuum theory suggests that, under certain conditions, there is an effective hydraulic conductivity, K_e, which satisfies:

$$\langle \bar{q} \rangle = -K_e \nabla \langle \bar{h} \rangle$$

Where:

$\langle \bar{q} \rangle$ = the expected flux

$\nabla \langle \bar{h} \rangle$ = the expected gradient

K_e is useful for nested models in that it can be used to estimate the expected value of the flux in a smaller domain (Dagan, 1986; Rubin and Gómez-Hernández, 1990). This suggests that a regional model with a homogeneous hydraulic conductivity of K_e could be used to determine the expected boundary fluxes of a site-scale model. If the rescaling of the geometric mean hydraulic conductivity is correct, the boundary flux of the regional model should be consistent with the average boundary flux of the site-scale stochastic continuum model. That is, the site-scale stochastic continuum model should conserve mass in an average sense with respect to the regional model fluxes.

Walker et al. (1997) suggested that the upscaling of block scale hydraulic conductivity could be calibrated using this relationship, adjusting the mean block hydraulic conductivity until the boundary fluxes of the ensemble matched the regional scale fluxes. However, there are several drawbacks to that approach. For example, the existence of K_e requires that the domain be stationary, extensive and under uniform flow conditions. In addition, the regional models conserve mass over the entire domain in an average sense, but may not conserve mass over arbitrary subdomains. Because of these limitations, this study does not adjust the mean block hydraulic conductivity to improve the flow balance between the models. However, as a check on the nested modelling and the upscaling of hydraulic conductivity, this study calculates the net volumetric flow of water across the boundaries. These flows are also reported as a mass balance for the regional and site models individually as a check on model internal consistency.

As shown in Figure 4.2-1, both models indicate that the majority of the inflow to the domain comes from surface recharge, and the majority of the outflow occurs across the southern model boundary. These flows represent the net flow across a boundary, and consequently do not reflect the complex distribution of inflows and outflows on each of the surfaces. The top surface, for example, has a net recharge due to precipitation, but also discharges to the mires and streams near the site. Table 4-1 summarises the flow for each face of the model domain. Note that the site-scale mass balance calculations carry only three significant digits, and thus contribute some error (Lovius, 1998).

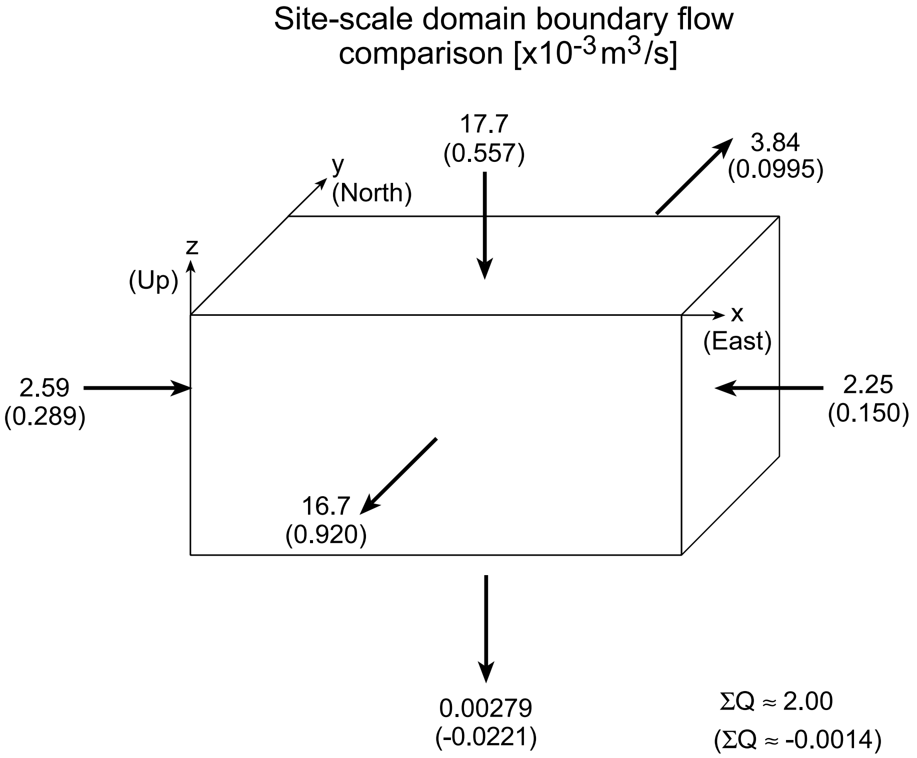

Figure 4.2-1. *Consistency of Ceberg boundary flow, regional versus site-scale models. The arithmetic mean flow for five realisations of the site-scale model is shown in parentheses. Arrows denote the regional flow direction.*

Table 4-1. Boundary flow consistency for Ceberg Base Case, regional model of Boghammar et al. (1997) versus site-scale.

	Net Flow Through Site Model Surfaces ($m^3/s \times 10^{-3}$)	
Model Surface	**Regional Base Case (GRST)**	**Site-scale Base Case (5 realisations)**
West	2.59 (in)	0.289 (in)
East	2.25 (in)	0.150 (in)
South	16.7 (out)	0.920 (out)
North	3.84 (out)	0.0995 (out)
Bottom	0.00279 (out)	0.0221 (in)
Top	17.7 (in)	0.557 (in)
Total Inflow	22.54	1.02
Total Outflow	20.54	1.02
Mass balance (In – Out)	2.00	–0.001

The average of 5 realisations of the site model suggests that the site model under-predicts the flow from the regional model by a factor of 20. In addition, the regional mass balance calculations show a 10% residual (inflow – outflow). Ideally, there should be no residual, and the boundary flows between the regional and site models should be an exact match. In practice, errors should be expected and evaluated.

To further investigate the boundary flows, this study constructs a mass balance for a reduced domain that omits the upper 200 m of the site-scale domain (i.e., the upper surface of the mass balance control volume is lowered to –100 masl for both models). Table 4-2 summarises the results of this computation, which show a dramatic improvement. The net inflow and ouflow over the site-scale domain for the regional and site-scale models are within 40%, suggesting that most of the discrepancy between the nested models occurs near the upper surface of the domain. This is attributed to mismatches in zone geometries and the use of calibrated conductivities in the upper surface of the Boghammar et al. (1997) regional model. For the regional mass balance over this reduced domain, the residual is reduced to approximately 6%. The regional mass balance residual is attributed to the approximate interpolation method used for calculating flows within finite elements of the regional model. When the control surfaces used for mass balance calculations do not coincide with element surfaces, the accuracy of this interpolation is limited. The accuracy of the interpolation also decreases as the contrast in hydraulic conductivities increases. It is important to note that this interpolation error is unrelated to the accuracy of the heads assigned to the site-scale model boundaries (Appendix B.2).

Table 4-2. Boundary flow consistency over a reduced domain at z = –100 m for Ceberg Base Case, regional model versus site-scale model.

	Net Flow Through Site Model Surfaces ($m^3/s \times 10^{-3}$)	
Model Surface	**Regional (GRST)**	**Base Case (5 realisations)**
Total Inflow	0.0413	0.0262
Total Outflow	0.0390	0.0262
Mass balance (In – Out)	0.0023	0.0000

These boundary flow comparisons suggest that the nested modelling and the upscaling of hydraulic conductivity qualitatively preserve mass balance between the models. Further discussion of the mass balance calculations can be found in Section 5.4 (regarding the Deterministic Variant).

4.3 Ensemble Results

4.3.1 Travel Time and F-ratio

In each realisation, HYDRASTAR calculates the travel times for a particle to be advected from each starting position (release position) to the model surface. The resulting stream tubes are used later in one-dimensional transport calculations in the PA model chain. Although the advective travel time is a common statistic for comparing variant simulations, it is important to note that HYDRASTAR allows only a homogenous flow porosity to be specified for the entire domain. Consequently, the travel time in any stream tube is directly proportional to this homogeneous flow porosity. This study simply uses the flow porosity of $\varepsilon_f = 1\times10^{-4}$, and leaves further analysis of the flow porosity to the transport modelling studies associated with SR 97.

Figure 4.3-1 presents the frequency histogram for the common logarithm of travel time for 100 realisations, each with 119 starting positions. A series of outliers are seen at the extreme upper tail of the histogram, corresponding to travel times of 100,000 years. These are the travel times for stream tubes that are intercepted by the southern, eastern and bottom surfaces of the model and that fail to exit the model's upper surface (approximately 10% of the total number of stream tubes; see Figure 4.4-1). In this circumstance, HYDRASTAR sets the travel times for these stream tubes to the default maximum travel time of 100,000 years.

The use of the default travel time does have noticeable effects on the performance measure statistics, as shown in Table 4-3 for the Base Case. To quantify this effect, this study calculates the statistics both with and without the travel times greater than 100,000 years. The means and variances of the travel time and F-ratio change slightly if stream tubes with the default travel time of 100,000 years are deleted. In contrast, the canister flux statistics are virtually unaffected by this censoring, as are the medians of travel time and F-ratio. For the remainder of this study, the performance measure statistics are calculated both with and without the travel times greater than 100,000 years. For the sake of brevity, the discussions will emphasise the medians of all measures and the statistics of travel time and F-ratio for travel times less than 100,000 years. The canister flux will be summarised with statistics computed for the full set of stream tubes (no deletions). The variances and medians of the performance measures are emphasised in bold in the summary tables (e.g., Table 4-3). The effects of this censoring on subsequent performance assessment calculations are beyond the scope of this study.

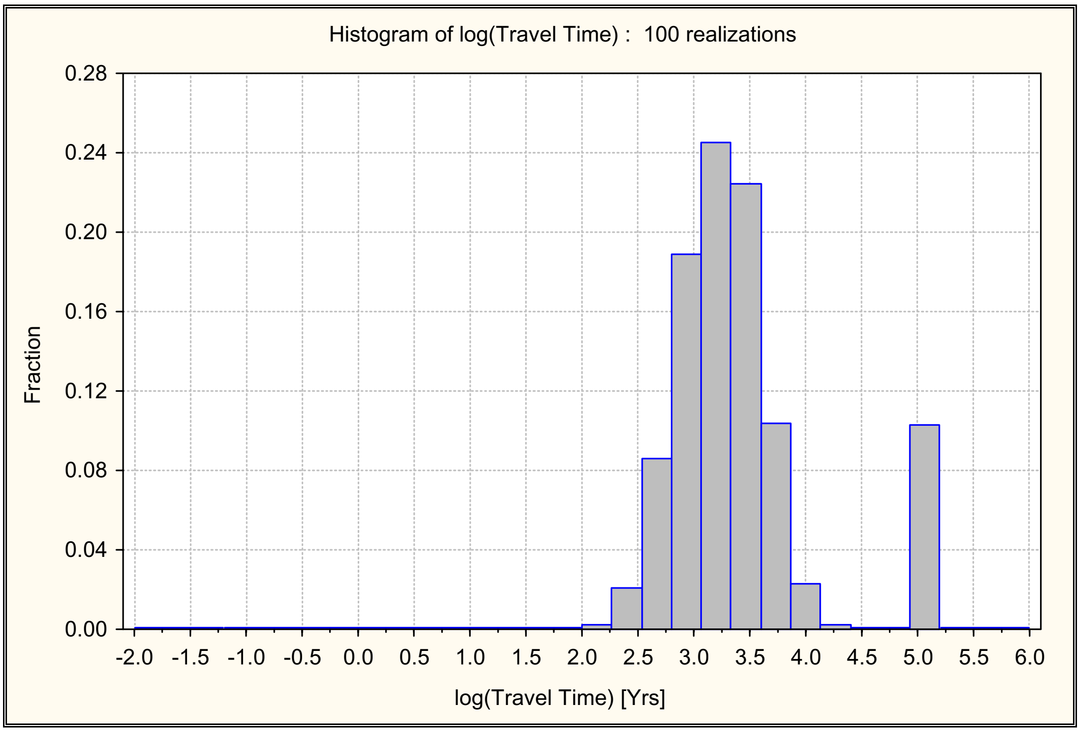

Figure 4.3-1. *Relative frequency histogram of $\log_{10}$ travel time for Ceberg Base Case. Results are shown for 100 realisations of 119 starting positions and a flow porosity of $\varepsilon_f = 1\times10^{-4}$.*

Table 4.3 summarises the ensemble results, presenting the statistics for the 100 Monte Carlo realisations of all 119 starting positions for travel time, canister flux and F-ratio. With the intercepted stream tubes deleted, the median travel time is 1720 years, with an interquartile range from 953 to 2965 years and a variance of $\log_{10}$ travel time of 0.123. Exclusive of the outliers, the distribution is almost perfectly symmetric. Figure 4.3-2 presents a box plot of the travel times by realisation, which indicates that the range of travel times in any single realisation can be extreme, ranging from a 5th percentile of 436 years to a 95th percentile of 6152 years.

Table 4-3. Summary statistics for Ceberg Base Case. Results are shown for 100 realisations of 119 starting positions, a flow porosity of $\varepsilon_f = 1\times10^{-4}$ and flow-wetted surface $a_r = 0.1$ m^2/(m^3 rock). Statistics in bold are discussed in the text. Approximately 10% of the stream tubes fail to reach the upper surface.

	All values			Travel Times > 100,000 years deleted		
	$\mathrm{Log_{10}}$ t_w	**$\mathrm{Log_{10}}$ q_c**	**$\mathrm{Log_{10}}$ F-ratio**	**$\mathrm{Log_{10}}$ t_w**	**$\mathrm{Log_{10}}$ q_c**	**$\mathrm{Log_{10}}$ F-ratio**
Mean	3.407	–4.499	6.407	3.224	–4.501	6.224
Median	3.288	**–4.485**	6.288	**3.236**	–4.488	**6.236**
Variance	0.401	**0.182**	0.401	**0.123**	0.182	**0.123**
5th percentile	2.654	–5.220	5.654	2.639	–5.225	5.639
25th percentile	3.011	–4.781	6.011	2.979	–4.785	5.979
75th percentile	3.572	–4.204	6.572	3.472	–4.205	6.472
95th percentile	5.000	–3.814	8.000	3.789	–3.815	6.789

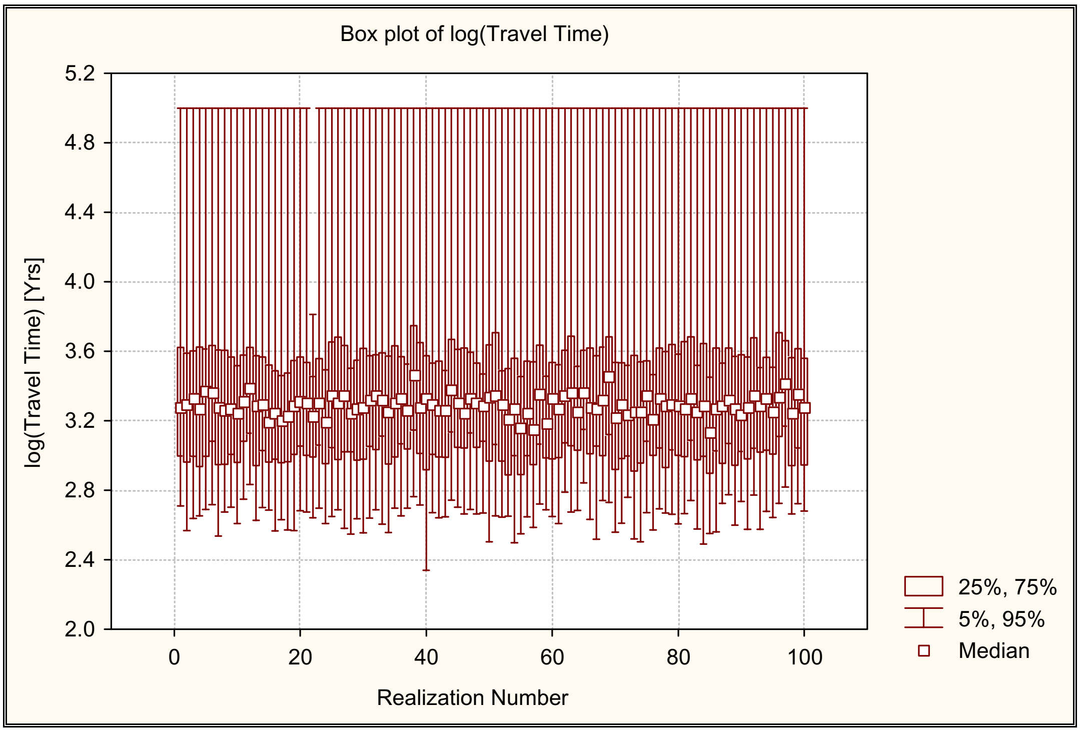

Figure 4.3-2. *Travel times by realisation for Ceberg Base Case. Results are shown for 119 starting positions and a flow porosity of* $\varepsilon_f = 1\times10^{-4}$.

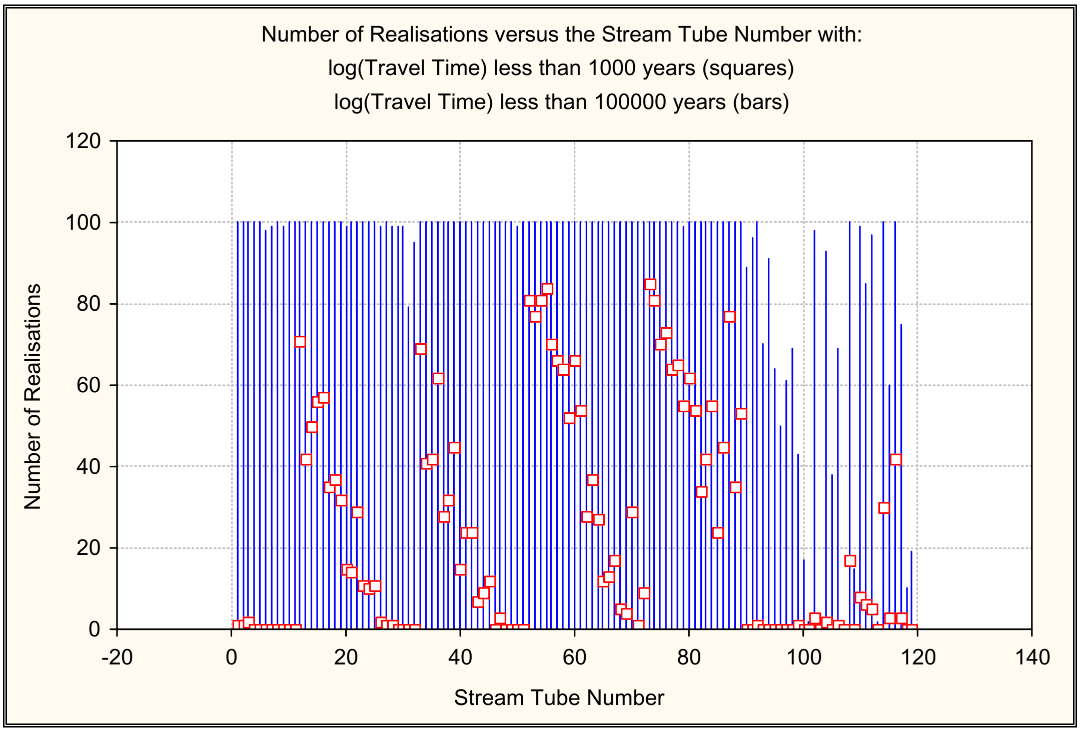

Figure 4.3-3. *Number of realisations with travel times less than 1000 years (squares) and 100,000 years (lines), by stream tube number for Ceberg Base Case. Results are shown for 100 realisations of 119 starting positions and a flow porosity of* $\varepsilon_f = 1\times10^{-4}$.

Figure 4.3-3 presents a box plot of the number of realisations with travel times less than a certain cut-off time, by stream tube (starting position number). There are several patterns that can be observed in this plot, for example the cycle of increasing travel time for certain sequences of starting position numbers (e.g., from location 11 to location 32). This pattern is an artefact of the numbering sequence of the stream tube starting positions, where the sequence of starting position numbers corresponds to a line running SW to NE in the repository. The SW side of the repository is relatively close to an important exit area, and the NE side of the repository is upgradient. Because the starting position numbers follow a sequence roughly parallel to the gradient in the central part of the repository (Figure 3.4-2), the sequence of starting position numbers 11 to 32 corresponds to an increase in travel path length. The other pattern that can be observed in Figure 4.3-3 is the reduced total number of realisations for some stream tubes with starting position numbers between 99 to 119. These stream tubes frequently are intercepted by the lateral boundaries of the model domain, and are consequently assigned the default maximum travel time (100,000 years). Stream tubes with starting position numbers between 90 to 98 are intercepted by the bottom surface of the model domain, and are likewise assigned the default maximum travel time.

The median F-ratio is 1.72×10^{6} year/m with an interquartile range from 9.53×10^{5} to 2.97×10^{6} year/m and a variance of $\log_{10}$ F-ratio of 0.123 (the same as the variance of $\log_{10}$ travel time; Table 4-3). Figure 4.3-4 presents the frequency histogram for the common logarithm of the F-ratio for 100 realisations, each with 119 starting positions for travel times less than 100,000 years. This histogram is essentially identical to the histogram of $\log_{10}$ travel times (Figure 4.3-1) because the F-ratio is a simple multiple of the travel time (see Section 3.5.4). This report presents the F-ratio for all variants, but in the interest of brevity will present the histogram of F-ratio only for the Base Case.

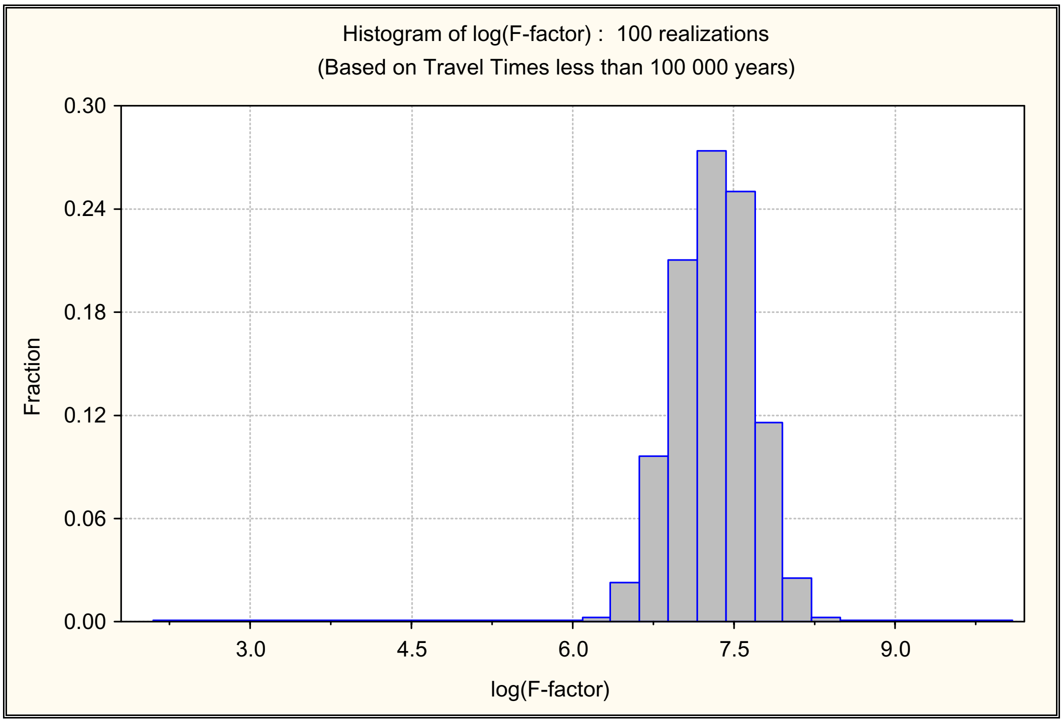

Figure 4.3-4. *Relative frequency histogram of $\log_{10}$ F-ratio for Ceberg Base Case. Results are shown for 100 realisations of 119 starting positions, a flow porosity of $\varepsilon_f = 1\times10^{-4}$ and a flow-wetted surface of $a_r = 0.1$ $m^2/(m^3$ rock).*

4.3.2 Canister Flux

HYDRASTAR calculated the canister fluxes (Darcy groundwater velocity) at each of the 119 starting positions. Table 4-3 summarises the results for the canister flux, which indicate a median canister flux of 3.27×10^{-5} m/year with an interquartile range from 1.66×10^{-5} to 6.25×10^{-5} m/year and a $\log_{10}$ canister flux variance of 0.182. Figure 4.3-5 presents the frequency histogram for $\log_{10}$ canister for the ensemble of 100 realisations. The distribution is nearly symmetric, reflecting the single mean and variance of the rock domain (i.e., there is no obvious mixing of populations resulting in a bimodal or skewed distribution). Figure 4.3-6 presents a box plot of $\log_{10}$ canister flux, which indicates no obvious pattern in the canister fluxes and that the values range over 1.5 orders of magnitude. Figure 4.3-7 presents a plot of $\log_{10}$ travel times vs. $\log_{10}$ canister flux, indicating that they have a weak inverse correlation. This might not be true for models with a stronger correlation structure or greater contrast between RD and CD conductivities. This is discussed further in Section 5.2.

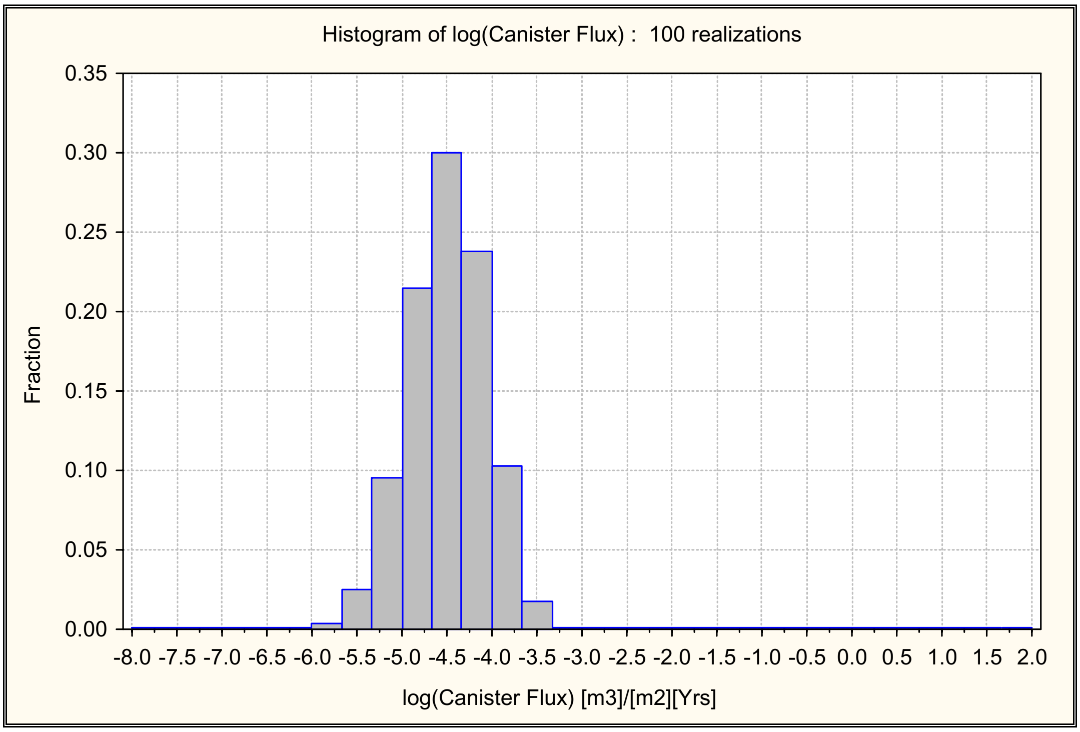

Figure 4.3-5. *Relative frequency histogram of log$_{10}$ canister flux for Ceberg Base Case. Results are shown for 100 realisations of 119 starting positions.*

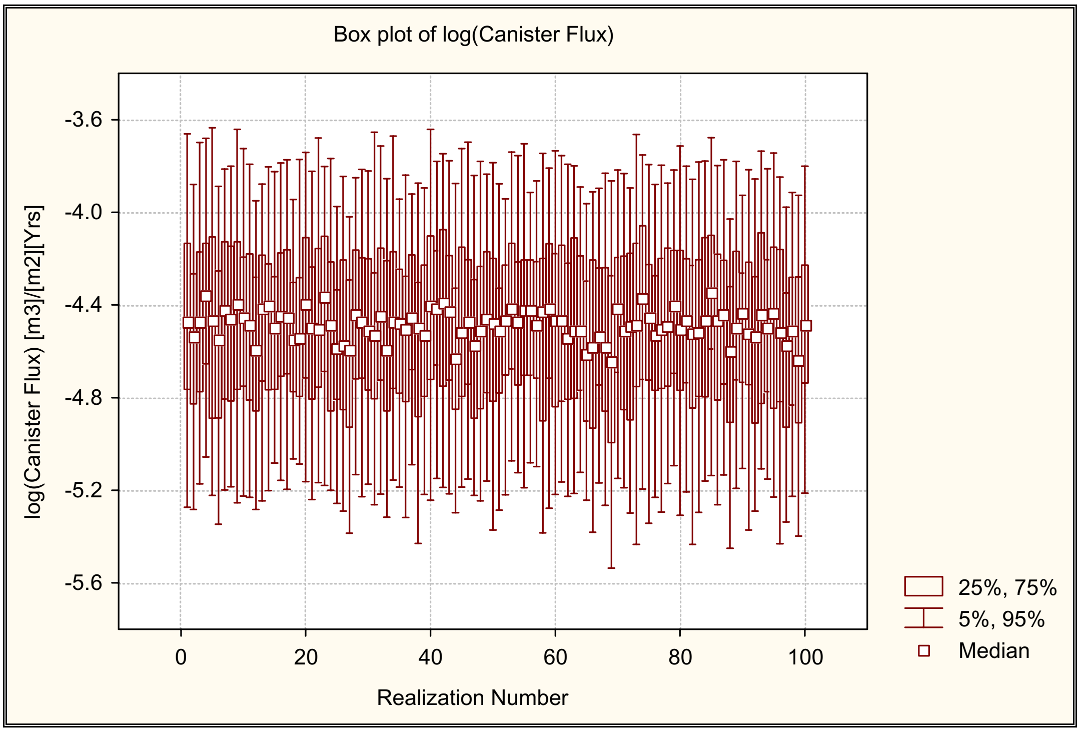

Figure 4.3-6. *Box plot of log$_{10}$ canister flux for Ceberg Base Case, by realisation. Results are shown for 119 starting positions.*

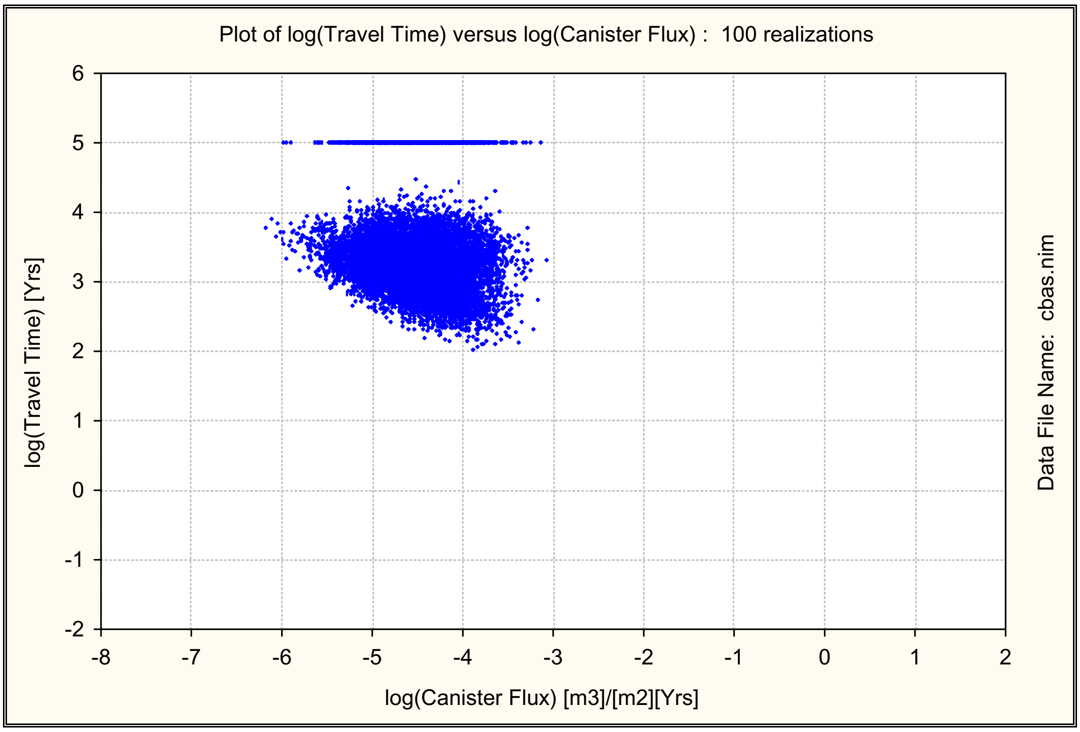

Figure 4.3-7. *Log$_{10}$ travel time versus log$_{10}$ canister flux for Ceberg Base Case. Results are shown for 100 realisations of 119 starting positions and a flow porosity of* $\varepsilon_f = 1\times10^{-4}$.

4.3.3 Flow Pattern and Exit Locations

The regional groundwater flow pattern is one of precipitation recharge on upland areas, discharging to streams and mires in lowlands (Sections 3 and 4.2). This flow pattern is reflected in the pattern of stream tubes calculated by HYDRASTAR, as shown in Figure 4.3-8. The stream tubes are directed predominantly downward, then radiating outward to discharge areas in to the east and southwest. The major discharge areas are the mires to the southwest of the repository (Tremyrorna, Högmyrån) and the mires and stream to the east of the repository (Husån).

As discussed in Section 3, the mapped fracture zones have a low hydraulic conductivity compared to fracture zones at other SKB sites. In addition, the spatial correlation is short relative to the block length, so that the conductive features representing the fracture zones will have little continuity. Thus we should expect the fracture zones as represented in the model to have relatively little influence on the stream tubes. Figure 4.3-8 also shows the stream tubes for a single realisation relative to the CD. The stream tubes are diverted by the fracture zones, but in many instances stream tubes pass directly through the fracture zones.

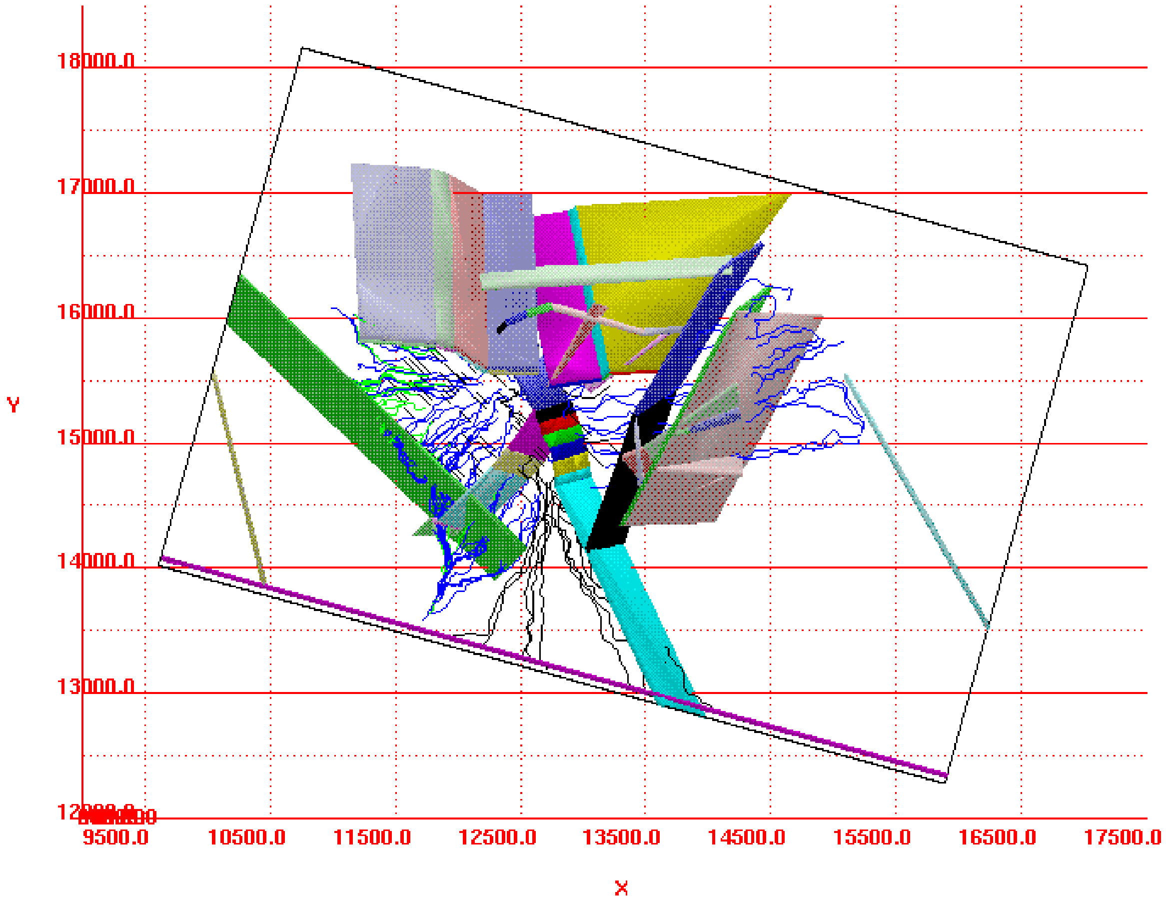

Figure 4.3-8. *Stream tubes in one realisation of the Ceberg Base Case. Conductive fracture zones (CD) are represented as planes (view from above, with North in the y-positive direction, scale in metres).*

Figure 4.3-9 presents a map of the model domain exit locations calculated by HYDRASTAR for each of the stream tubes. The exit locations plotted in Figure 4.3-9 are the points where the stream tubes are intercepted by the model boundary. Note that the exit level at the top of the model is actually 35 m inside the domain, at an elevation of 25 masl (Section 3.4) due to restrictions of the HYDRASTAR particle tracking algorithm and the model grid size. As discussed in Section 4.3.1, approximately 90% of the stream tubes exit the upper surface of the model. Approximately 8.8% of the stream tubes exit the southern model boundary, 0.076% exit the eastern model boundary and 1.3% exit the bottom boundary of the model. A small percentage (0.076%) of stream tubes become trapped in regions of converging flow and reach the maximum number of iterations in the particle tracking routine.

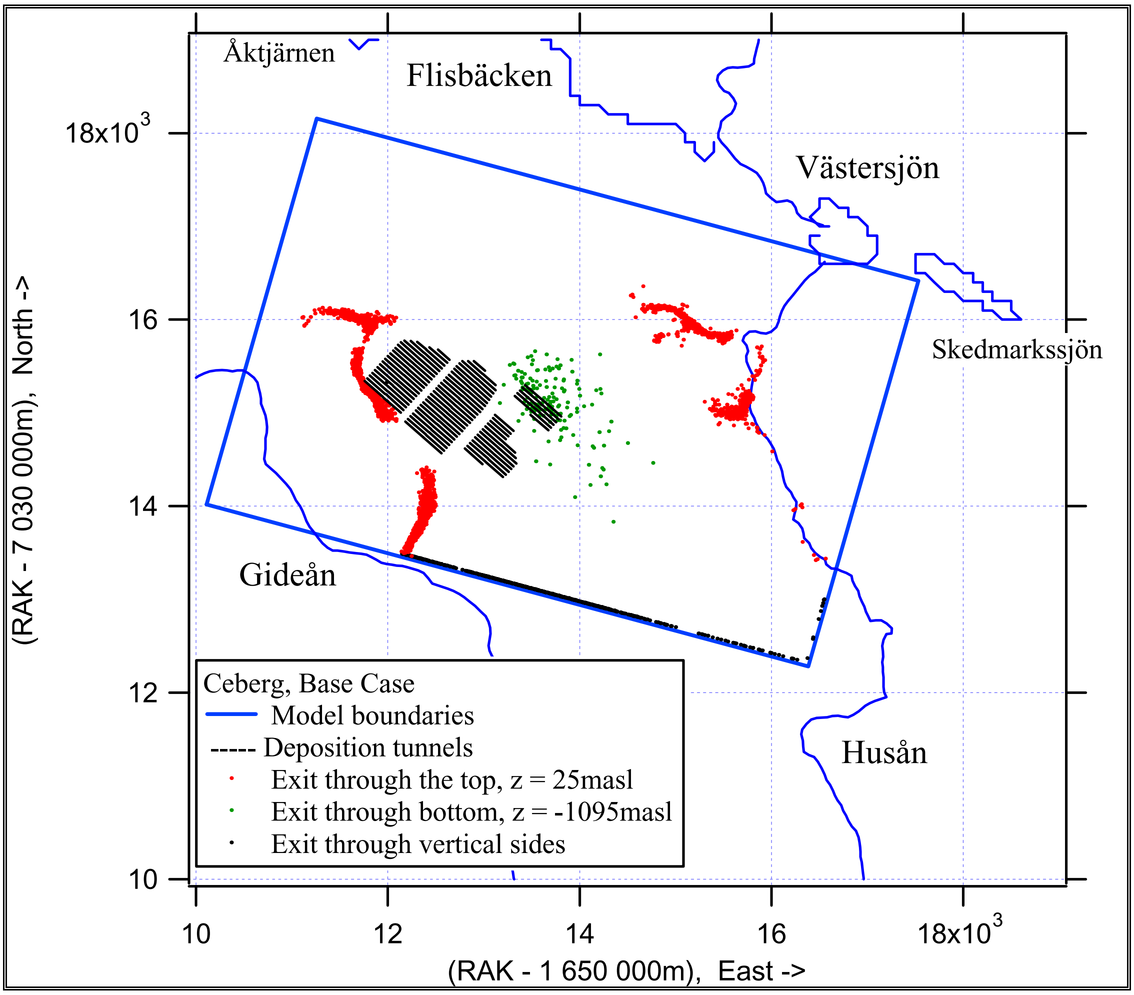

Figure 4.3-9. *Exit locations for Ceberg Base Case, 100 realisations of 119 starting positions. Repository tunnels at –500 masl shown projected up to the model surface (plan view, scale in metres).*

The exit locations are further examined by separating the first 100 realisations of the exit locations into four discharge areas (Figure 4.3-10). Floating histograms of $\log_{10}$ travel time for each of these discharge areas are shown in Figure 4.3-11 (Appendix A.1). Discharge Area 2 includes stream tubes that exit both the southern and top surfaces of the model. Because stream tubes exiting the southern boundary are set to the default maximum travel time of 100,000 years, the $\log_{10}$ travel time distribution for discharge Area 2 is bimodal. Discharge Area 3 receives stream tubes that are intercepted by the bottom surface of the model (approximately 1.28% of all the stream tubes). Because these stream tubes are set to the default maximum travel time, the $\log_{10}$ travel time histogram for Discharge Area 3 is a uniform distribution centred around 100,000 years. The stream tubes exiting in Area 3 originate from starting position numbers 90 to 98 in the northeastern part of the repository, and they reflect the downward recharge and flow at the centre of the site (see also Table 4-1).

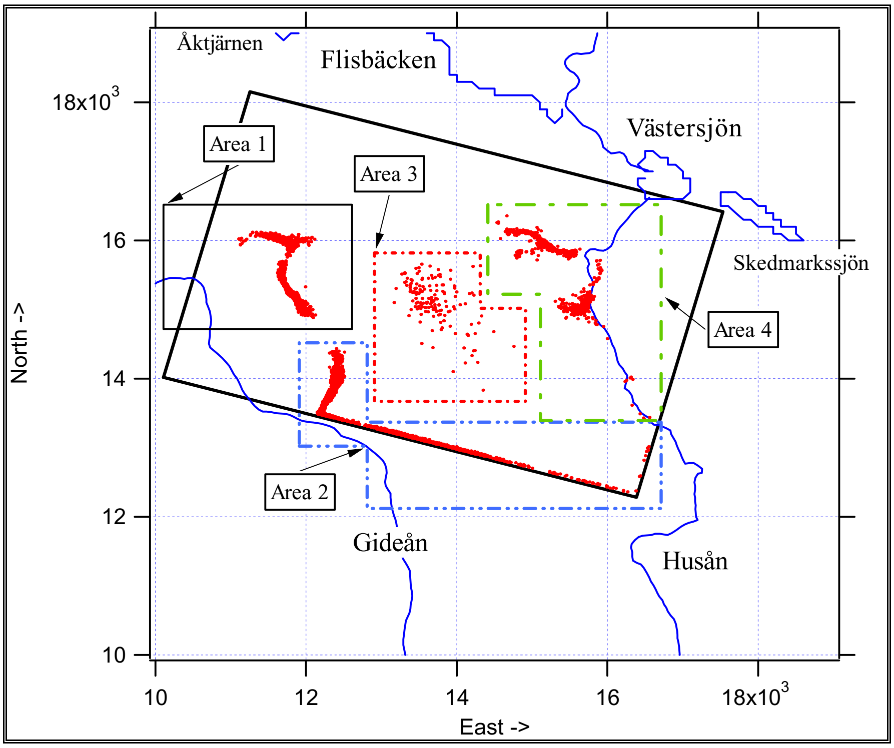

Figure 4.3-10. *Discharge areas and exit locations for the Ceberg Base Case. Results are shown for 100 realisations of 119 starting positions (plan view, scale in metres).*

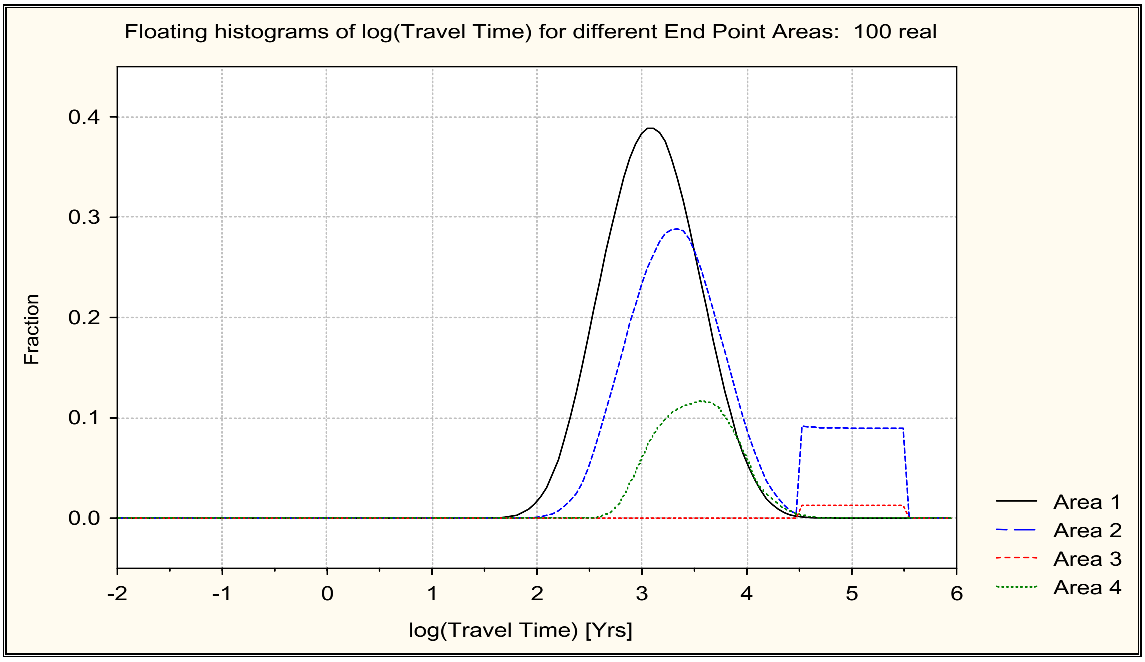

Figure 4.3-11. *Floating histogram of $\log_{10}$ travel time for stream tubes exiting to the discharge areas shown in Figure 4.3-10. Results are shown for 100 realisations of 119 starting positions and a flow porosity of $\varepsilon_f = 1\times10^{-4}$.*

As discussed above, HYDRASTAR does not explicitly report the travel times for stream tubes that are intercepted by the side and bottom boundaries of the model. In this circumstance, HYDRASTAR sets the travel time to the default maximum of 100,000 years. It is possible to post-process the stream tube output of HYDRASTAR using MatLab scripts to determine the exit locations and the travel time to the southern boundary. Figure 4.3-12 presents the exit locations on the southern boundary. Although there is a linear pattern suggesting that a fracture zone is controlling the flow pattern, this is exclusively the effect of the regional flow pattern. The median travel time of the stream tubes intercepted by this boundary is 5082 years, with an interquartile range from 3758 to 7145 years. For the stream tubes intercepted by the bottom boundary of the site, the median travel time is 4055 years, with an interquartile range from 2655 to 5888 years.

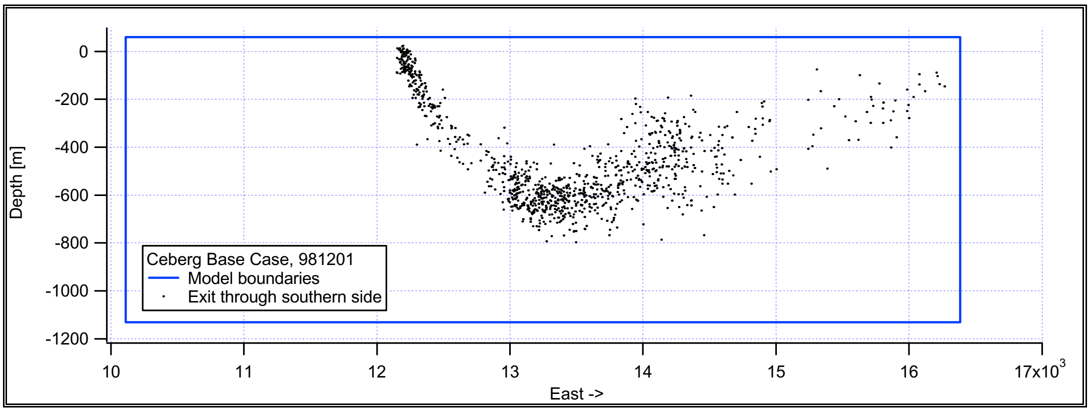

Figure 4.3-12. *Exit locations on the southern model surface for the Ceberg Base Case. Results are shown for 100 realisations of 119 starting positions (elevation view looking North, scale in metres).*

4.3.4 Validity of Results

An approximate calculation of the travel time was performed as a check on the validity of the model. These computations used Darcy's Law, the estimated gradient, a simple flow path, and the mean hydraulic conductivities to estimate the advective travel time from the centre of the repository to the exit locations to the south and east of the site (Appendix C.2). The results showed that the travel time should be on the order of 1000 years, roughly in agreement with the median travel time of the Base Case.

In a previous modelling study of the Gideå site, Carlsson et al. (1983) determined the advective travel times from –500 depth to ground surface. Using a flow porosity of $\varepsilon_f = 4\times10^{-3}$, they found that the travel times ranged from 1000 to 300,000 years. Although the range of their results is extreme, the results of the Carlsson et al. study suggest that the travel times of this study are reasonable.

It is also useful to compare the observed heads from boreholes at Gideå site versus the simulated heads. Although a limited amount of head data are available, it is from a relatively short monitoring interval and is therefore not believed to be representative of the long-term steady-state conditions represented by the Base Case (Ahlbom et al., 1991). Consequently, this study does not directly compare model-simulated heads versus observed heads.

4.4 Individual Realisations

There are several strategies that could be used to select several realisations that are in some sense representative of the ensemble. For example, we could select a realisation whose travel time or canister flux is close to the median of the ensemble of the realisations. However, the probability of each realisation in a Monte Carlo set is equal by definition, so that no single realisation can be said to be representative of the ensemble. This study examines three random realisations to illustrate the variability in and among individual realisations.

Figure 4.4-1 presents the stream tubes in realisation number one of the Base Case. The stream tubes reflect the overall downward and lateral flow pattern at the site, as a result of the regional flow pattern.

As an illustration of the variability within and between realisations, the first three realisations of the Base Case are examined in more detail (note that these realisations are randomised by the random number generation). Figure 4.4-2 presents plan views of the stream tubes for the first three realisations of the Base Case. Although the general flow pattern remains the same from realisation to realisation, the exit locations can vary widely for any particular stream tube.

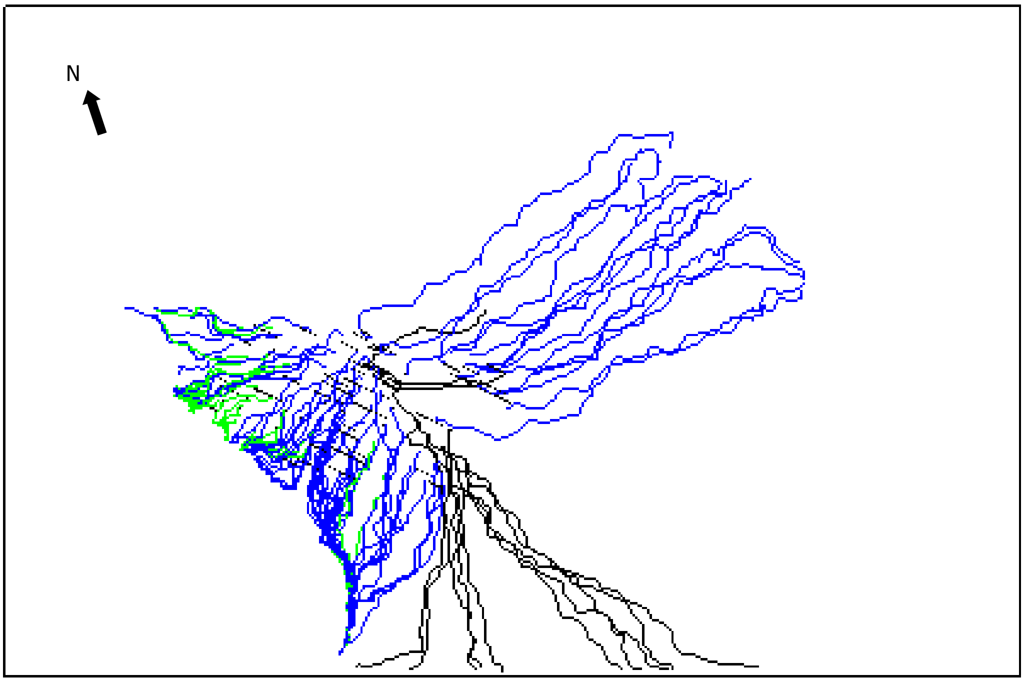

a) Plan view

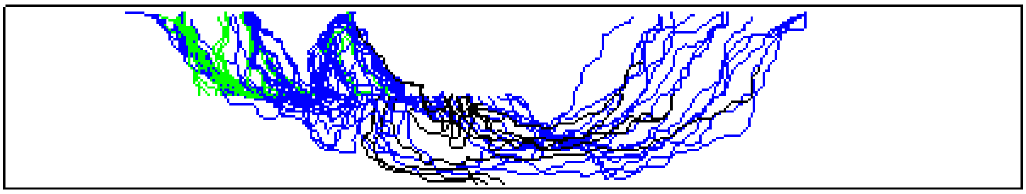

b) Elevation view, from South

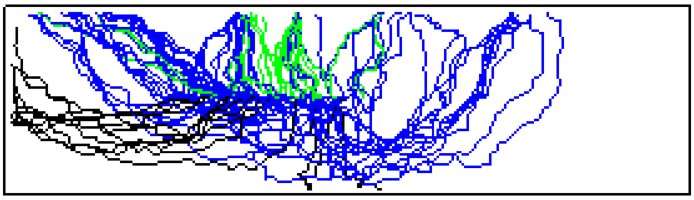

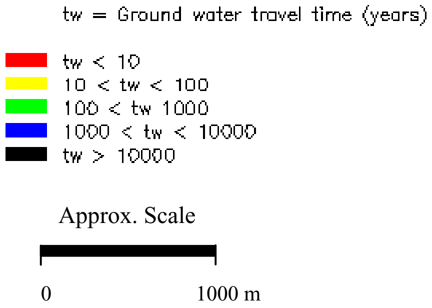

c) Elevation view, from East

Figure 4.4-1. *Stream tubes in realisation number 1 of Ceberg Base Case. The y-positive axis of a) is rotated cw from North. Results are shown for 119 starting positions and a flow porosity of* $\varepsilon_f = 1\times10^{-4}$.

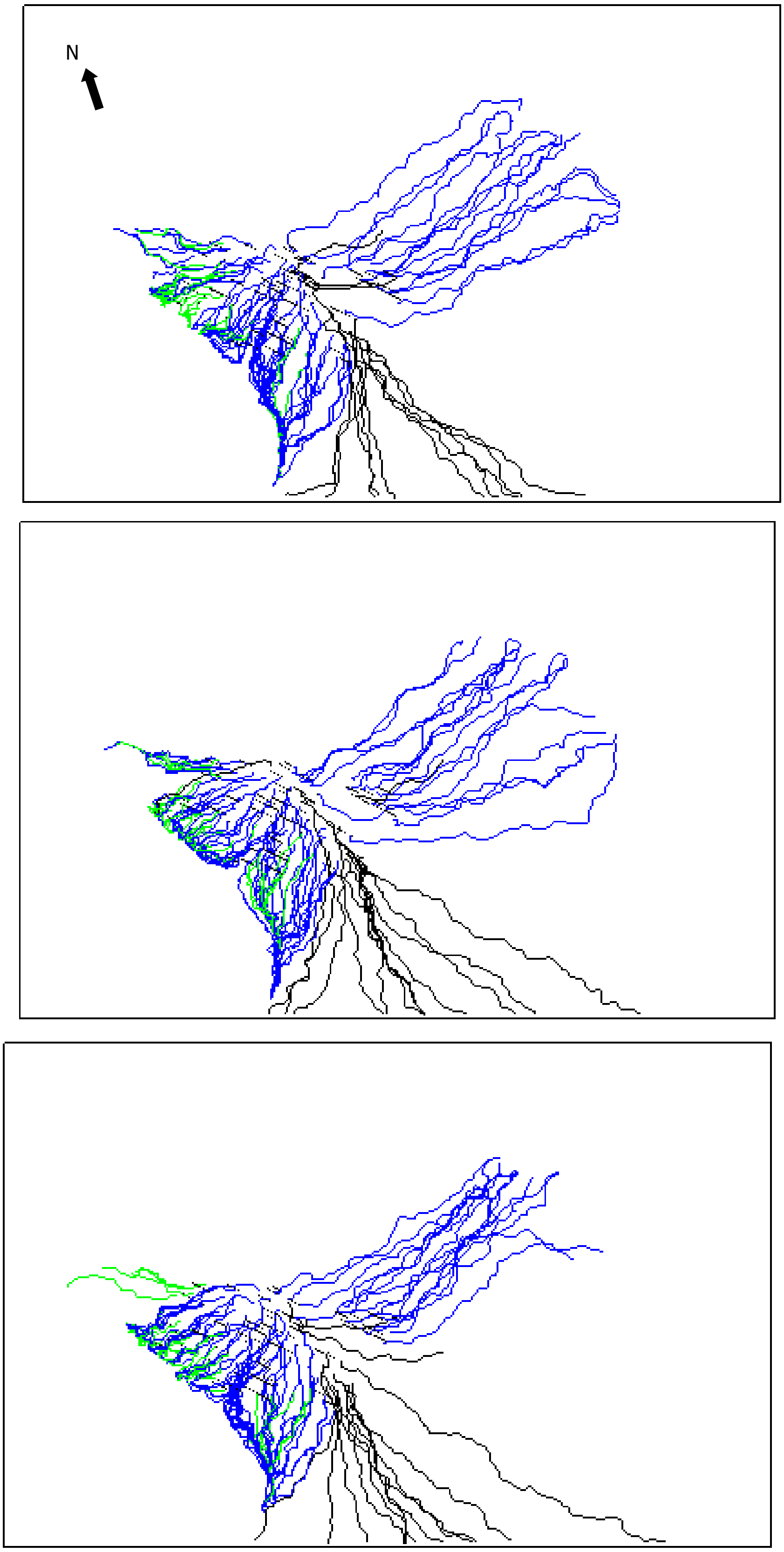

Figure 4.4-2. *Stream tubes for Ceberg Base Case realisation numbers 1 through 3, plan view (looking downward). Results are shown for 119 starting positions and a flow porosity of* $\varepsilon_f = 1\times10^{-4}$. *(Not to scale; refer to Figure 4.4-1 for legend).*

Table 4.4 presents the summary statistics for the realisations shown in Figure 4.4-2. The statistics suggest that the variances of $\log_{10}$ travel time and $\log_{10}$ canister flux are rather high within a realisation. In contrast, the medians of these performance measures change very little from one realisation to the next. This suggests that the variability of performance measures is the result of spatial variability within a realisation, and not the variability between realisations. This suggestion is confirmed by the floating histograms of these performance measures, which show little difference in shape or location from realisation to realisation (Figure 4.4-3; Appendix A.1).

Within each realisation, the travel time and canister flux can vary widely. Figures 4.4-4 and 4.4-5 present plots of travel time and canister flux, respectively, versus starting position number. Although the canister fluxes show no specific pattern (Figure 4.4-5), the travel times show a cyclical pattern that reflects the travel path length (Figure 4.4-4; see also Section 4.3.1).

Table 4-4. Summary statistics over all starting positions for three realisations. Results are shown for 119 starting positions, a flow porosity of $\varepsilon_f = 10^{-4}$ and flow-wetted surface of $a_r = 0.1$ m^2/(m^3 rock). Bold statistics are discussed in the text.

	Realisation 1	**Realisation 2**	**Realisation 3**
Log$_{10}$ Travel Time (years, for times less than 100,000 years)			
Mean	3.220	3.203	3.244
Median	**3.207**	**3.238**	**3.252**
Variance	**0.123**	**0.129**	**0.135**
5th percentile	2.710	2.577	2.643
25th percentile	2.984	2.946	2.973
75th percentile	3.483	3.481	3.540
95th percentile	3.815	3.698	3.867
Log$_{10}$ Canister Flux (m/year, for full set of travel times)			
Mean	–4.476	–4.557	–4.459
Median	**–4.472**	**–4.537**	**–4.470**
Variance	**0.216**	**0.173**	**0.183**
5th percentile	–5.267	–5.171	–5.121
25th percentile	–4.736	–4.821	–4.761
75th percentile	–4.142	–4.276	–4.177
95th percentile	–3.670	–3.891	–3.708
Log$_{10}$ F-ratio (year/m, for times less than 100,000 years)			
Mean	6.220	6.203	6.244
Median	**6.207**	**6.238**	**6.252**
Variance	**0.123**	**0.129**	**0.135**
5th percentile	5.710	5.577	5.643
25th percentile	5.984	5.946	5.973
75th percentile	6.483	6.481	6.540
95th percentile	6.815	6.698	6.867

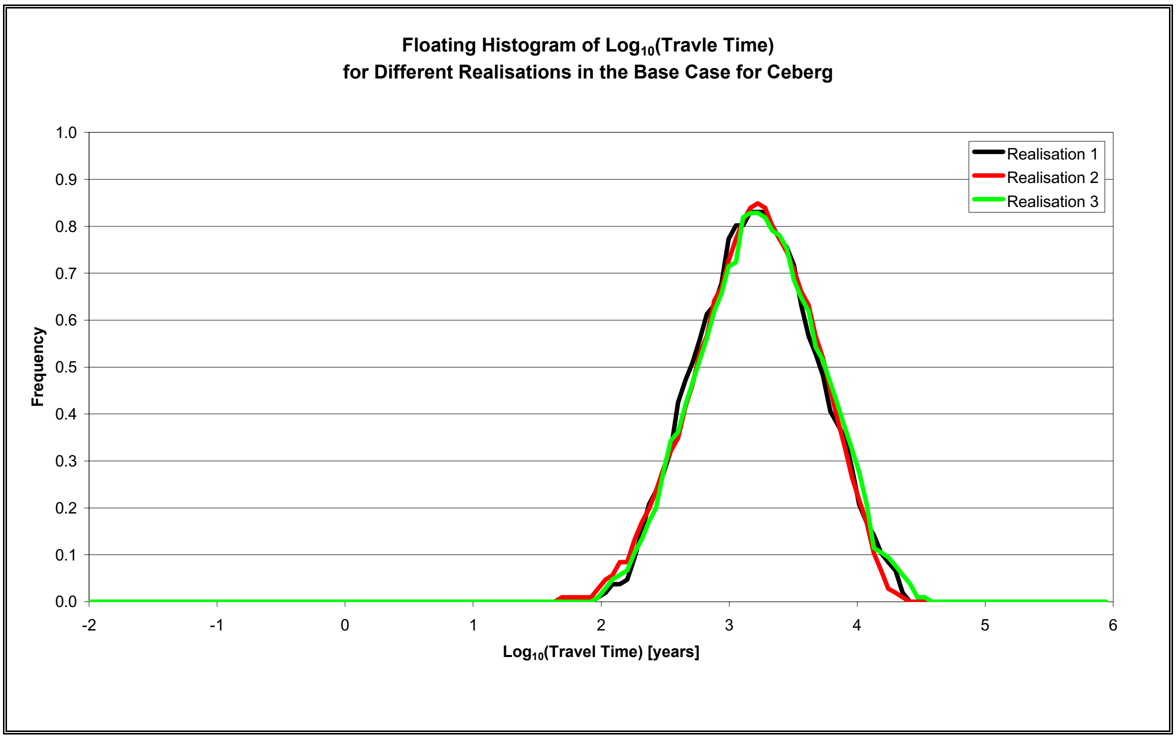

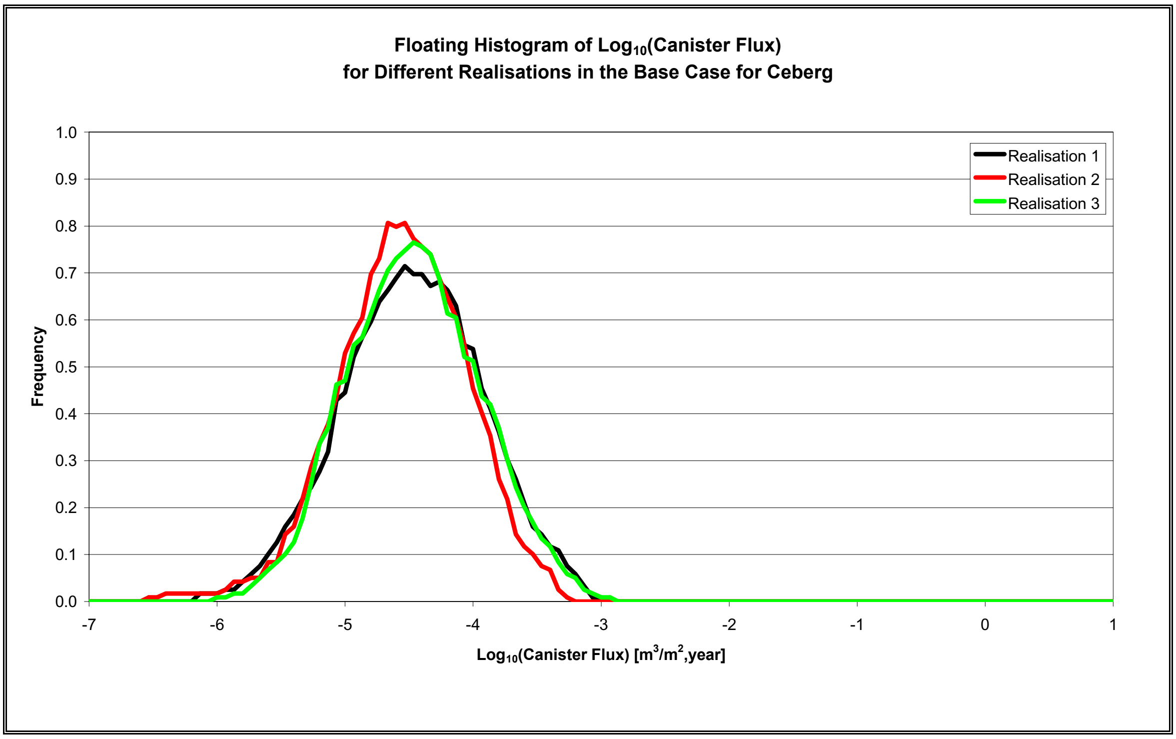

Figure 4.4-3. *Realisations 1, 2, and 3 of the Ceberg Base Case, floating histograms of log*$_{10}$ *travel time (upper plot) and log*$_{10}$ *canister flux (lower plot). Results are shown for 119 starting positions and a flow porosity of* $\varepsilon_f = 1\times10^{-4}$.

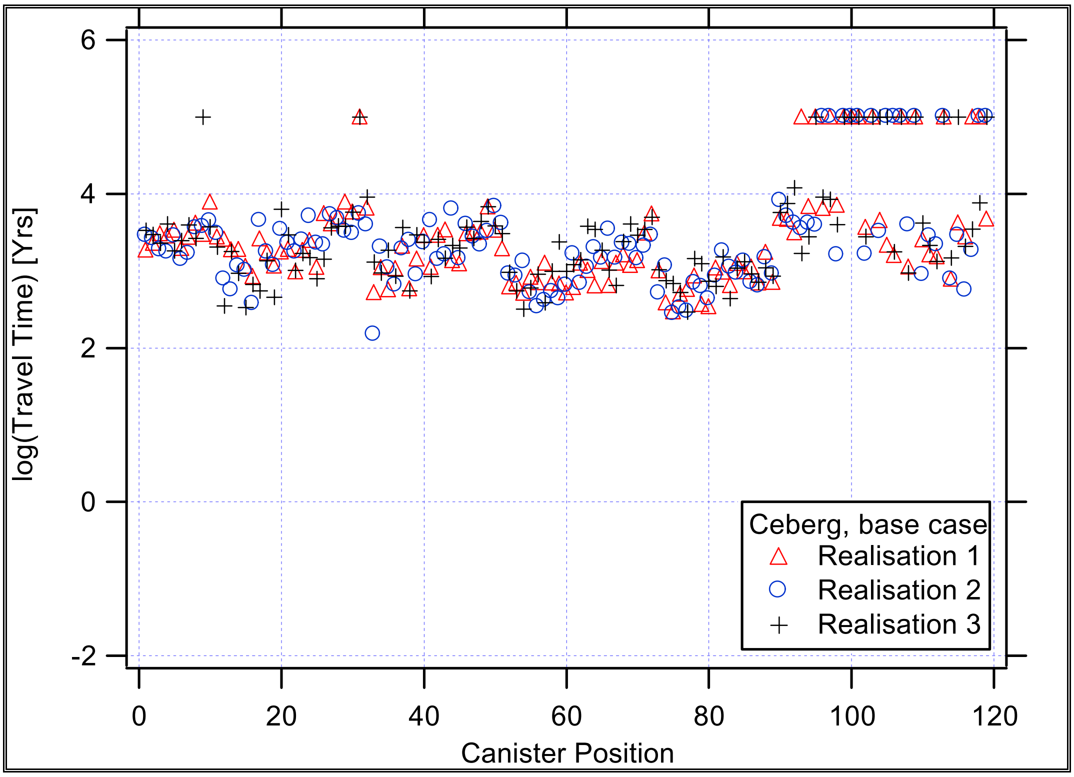

Figure 4.4-4. *Log$_{10}$ travel time versus starting position for three realisations of the Ceberg Base Case. Results are shown for 119 starting positions and a flow porosity of $\varepsilon_f = 1\times10^{-4}$.*

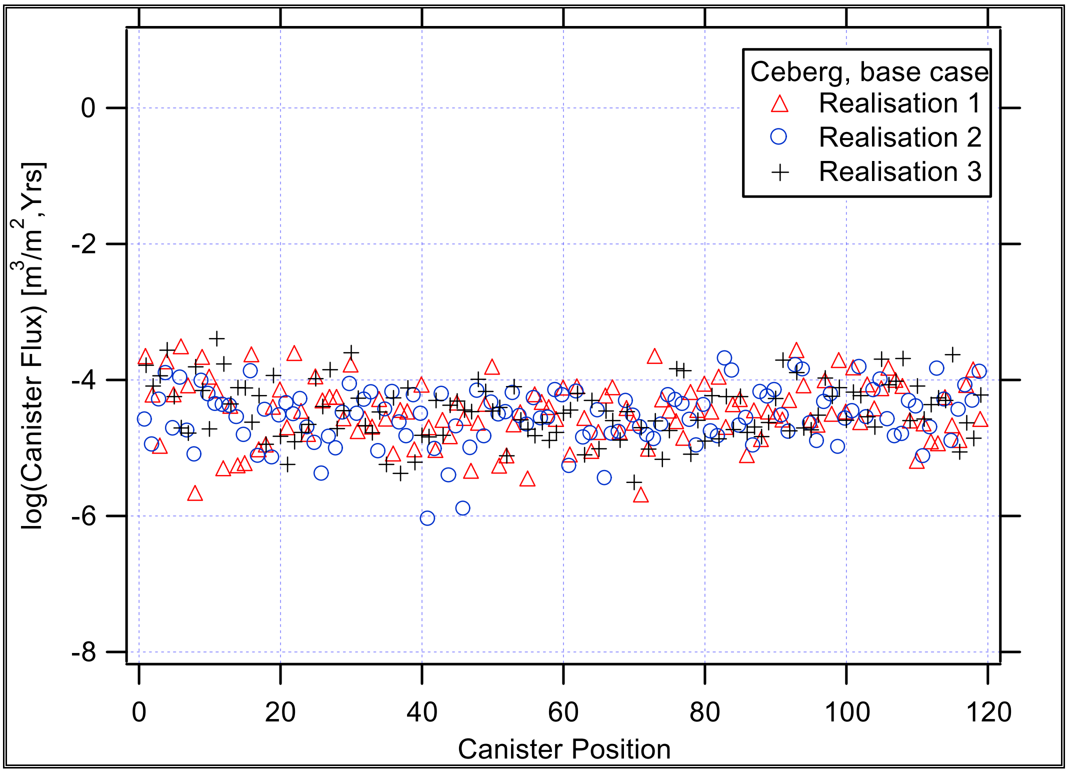

Figure 4.4-5. *Log$_{10}$ canister flux versus starting position for three realisations of the Ceberg Base Case. Results are shown for 119 starting positions.*

4.5 Individual Starting Positions

This study examines three individual starting positions to illustrate the performance of three specific repository areas. Starting position number 1 is located in block 13 and has relatively long travel times, position 52 is located in the southern part of block 2 and has relatively short travel times, and position 71 is located in northern part of block 2 and has relatively long travel times. Positions 52 and 71 were chosen to illustrate the differences due to location in the north versus the south, and position 1 was chosen to represent the starting positions in block 13 (on the eastern side of the repository). The stream tubes from these three starting positions are shown for the first 50 realisations.

For each of these starting positions, floating histograms (Appendix A) and summary statistics are compiled over all realisations. Figure 4.5-1 presents the Monte Carlo stability of the median of $\log_{10}$ travel time for each starting position. These plots suggest that, after 40 realisations, the estimates of the median of $\log_{10}$ travel time are essentially constant with respect to the number of realisations.

Figures 4.5-2, 4.5-3 and 4.5-4 present the stream tubes for starting positions 1, 52 and 71, respectively, and Table 4-5 summarises the statistics of the performance measures compiled over 100 realisations. Figures 4.5-5 and 4.5-6 are plots of the $\log_{10}$ travel time and $\log_{10}$ canister flux, respectively, versus the realisation number for these three starting positions. Both plots illustrate a high degree of variability from realisation to realisation, but there is an important difference illustrated by these plots. While the $\log_{10}$ travel time shows that the starting positions have different average travel times, the canister flux plot shows that the starting positions have approximately the same average canister flux. This suggests that the differences in median travel time noted previously are due to the difference in travel path length, not to rock type or local variations in recharge rate. The smoothed histograms of $\log_{10}$ travel time and $\log_{10}$ canister flux for these starting positions (Figures 4.5-7 and 4.5-8) reinforce this conclusion. At position 52, for example, the travel times are relatively short even though the canister flux is relatively moderate. This is attributed to the short travel path from this position, where the flow path is essentially vertical in all realisations (Figure 4.5-3). Note that Figures 4.5-7 and 4.5-8 are smoothed relative frequency histograms, constructed somewhat differently than the floating histograms used elsewhere in this report. These smoothed histograms are constructed using Igor by plotting a continuous line for the frequency within chosen bin widths, then smoothing the line via a gaussian-weighted average within a moving window. Although smoothed histograms are a somewhat subjective filtering of the results, the smoothing algorithm is a useful alternative when the default floating histogram window of ± one order of magnitude is wider than the standard deviation of the results.

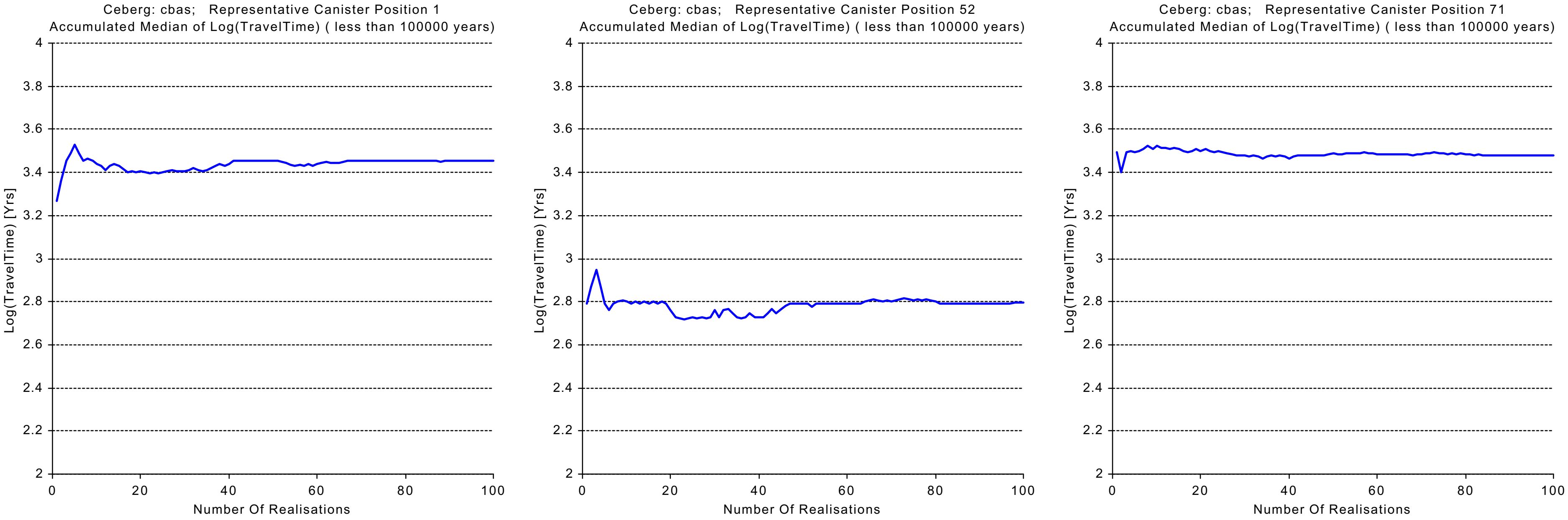

Figure 4.5-1. *Monte Carlo stability at starting positions 1, 52, and 71 in the Ceberg Base Case: median* $\log_{10}$ *travel time versus number of realisations. Results are shown for a flow porosity of* $\varepsilon_f = 1\times10^{-4}$.

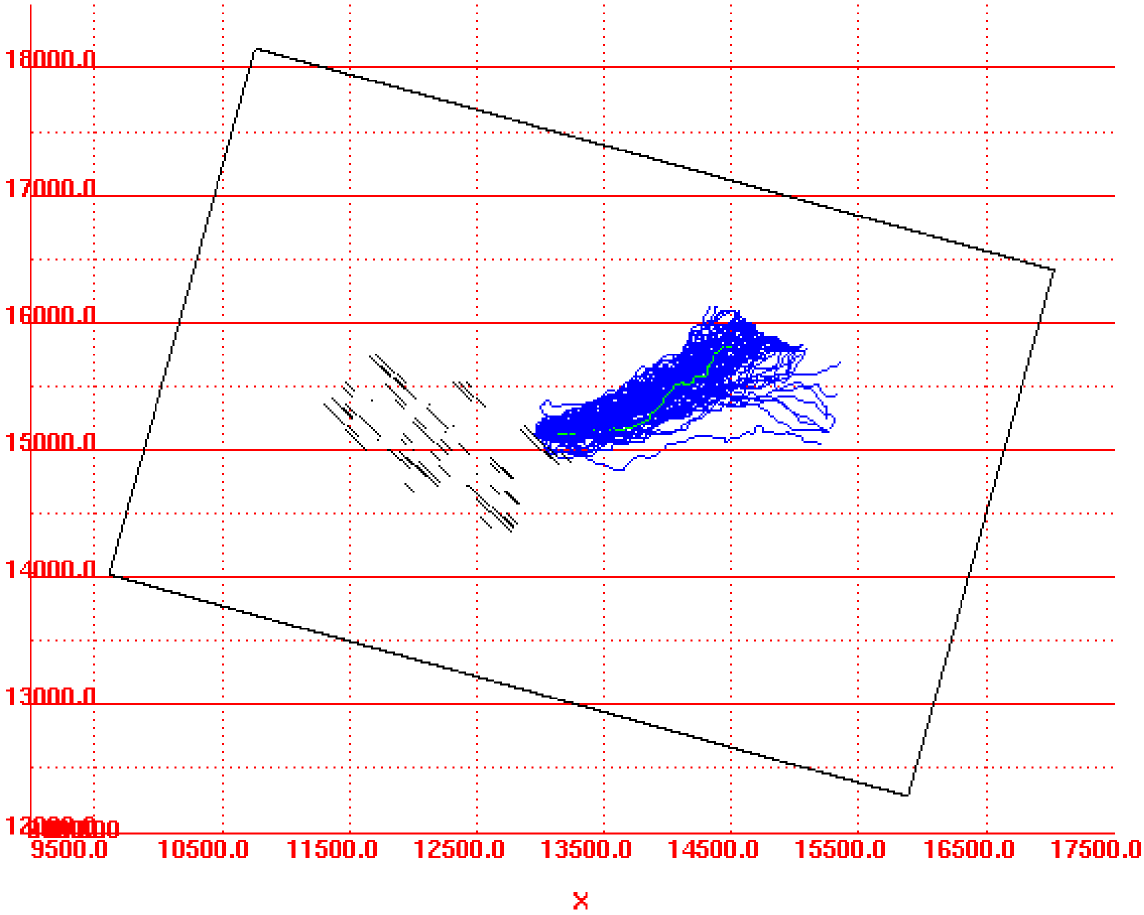

Figure 4.5-2. *Stream tubes from starting position 1, Ceberg Base Case. Results are shown for the first 50 realisations and a flow porosity of* $\varepsilon_f = 1\times10^{-4}$ *(plan view, with North in the y-positive direction, scale in metres).*

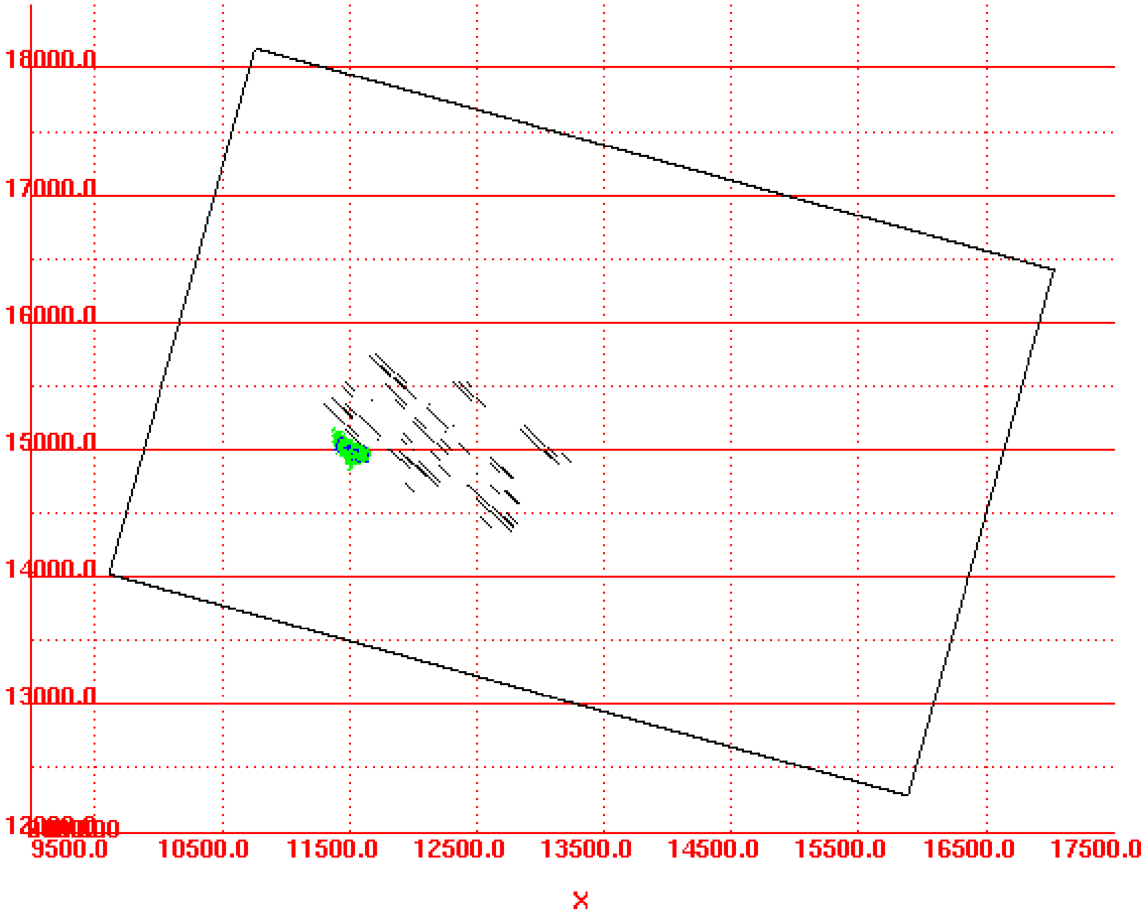

Figure 4.5-3. *Stream tubes from starting position 52, Ceberg Base Case. Results are shown for the first 50 realisations and a flow porosity of* $\varepsilon_f = 1\times10^{-4}$ *(plan view, with North in the y-positive direction, scale in metres).*

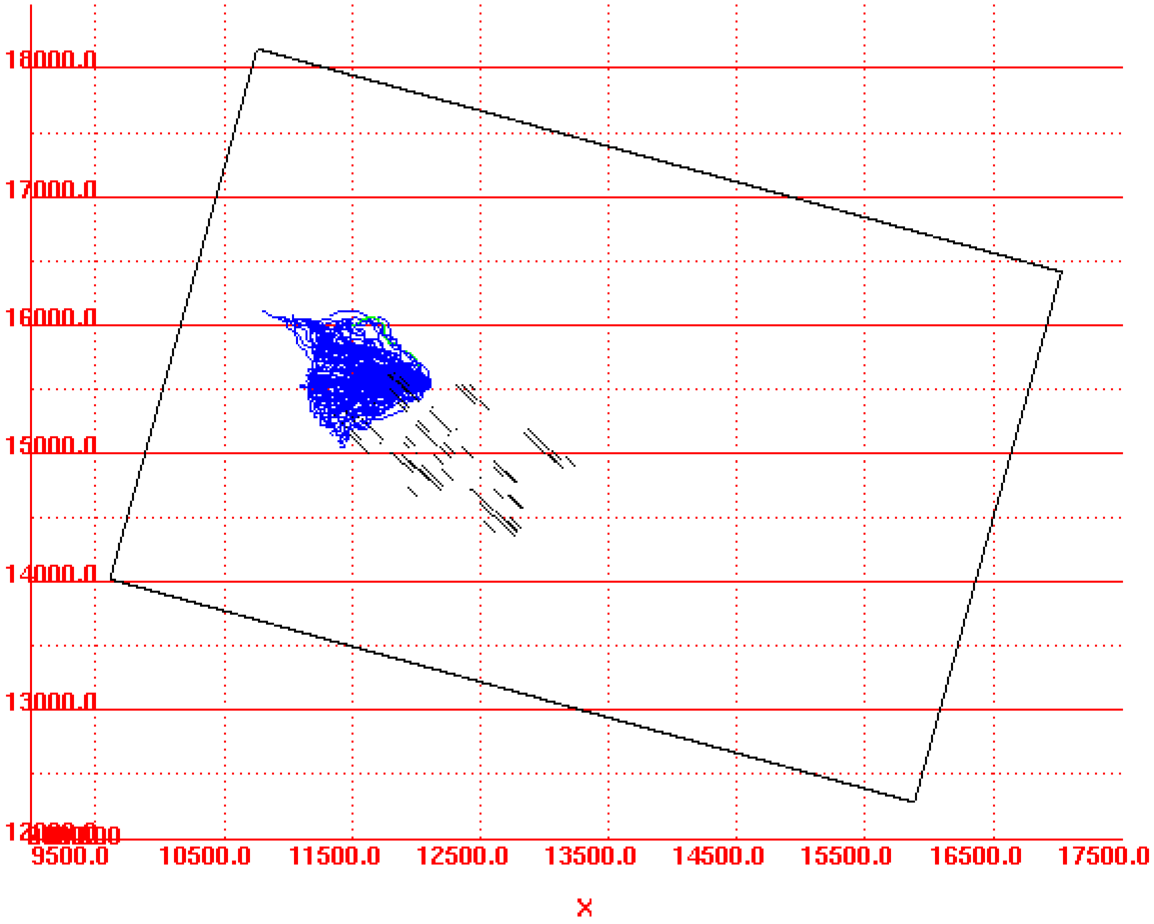

Figure 4.5-4. *Stream tubes from starting position 71, Ceberg Base Case. Results are shown for the first 50 realisations and a flow porosity of* $\varepsilon_f = 1\times10^{-4}$ *(plan view, with North in the y-positive direction, scale in metres).*

Table 4-5. Summary statistics for three starting positions. Results are shown for 100 realisations, a flow porosity of $\varepsilon_f = 1\times10^{-4}$ and flow-wetted surface of $a_r = 0.1\ m^2/(m^3$ rock). Note: No paths exceed 100,000 years; therefore, the statistics represent the full set of travel times. Statistics in bold are discussed in the text.

	Starting Position Number		
Log_{10} Travel Time (years)	**1**	**52**	**71**
Mean	3.461	2.811	3.471
Median	**3.456**	**2.795**	**3.479**
Variance	**0.021**	**0.072**	**0.037**
5th percentile	3.243	2.400	3.174
25th percentile	3.369	2.613	3.324
75th percentile	3.555	2.968	3.615
95th percentile	3.707	3.303	3.792
Log_{10} Canister Flux (m/year)			
Mean	–4.290	–4.552	–4.696
Median	**–4.232**	**–4.503**	**–4.672**
Variance	**0.162**	**0.194**	**0.167**
5th percentile	–5.007	–5.270	–5.515
25th percentile	–4.601	–4.877	–4.983
75th percentile	–4.019	–4.240	–4.436
95th percentile	–3.635	–3.983	–4.048
Log_{10} F-ratio (year/m)			
Mean	6.461	5.811	6.471
Median	**6.456**	**5.795**	**6.479**
Variance	**0.021**	**0.072**	**0.037**
5th percentile	6.243	5.400	6.174
25th percentile	6.369	5.613	6.324
75th percentile	6.555	5.968	6.615
95th percentile	6.707	6.303	6.792

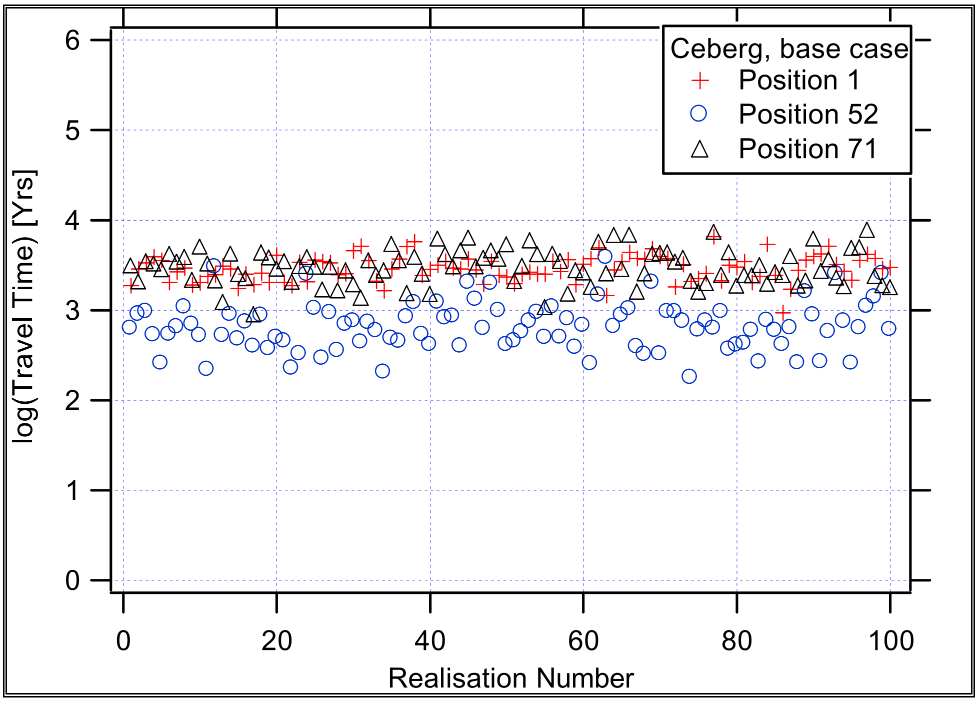

Figure 4.5-5. *Log$_{10}$ travel time versus realisation number for three starting positions in the Ceberg Base Case. Results are shown for100 realisations and a flow porosity of* $\varepsilon_f = 1\times10^{-4}$.

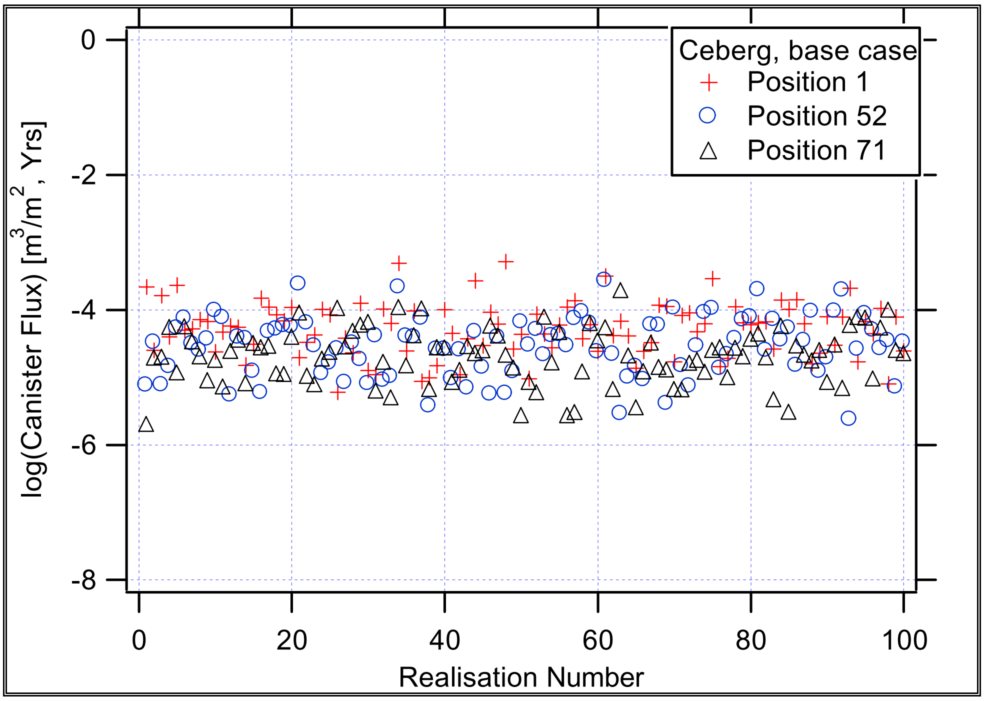

Figure 4.5-6. *Log$_{10}$ canister flux versus realisation number for three starting positions in the Ceberg Base Case. Results are shown for100 realisations.*

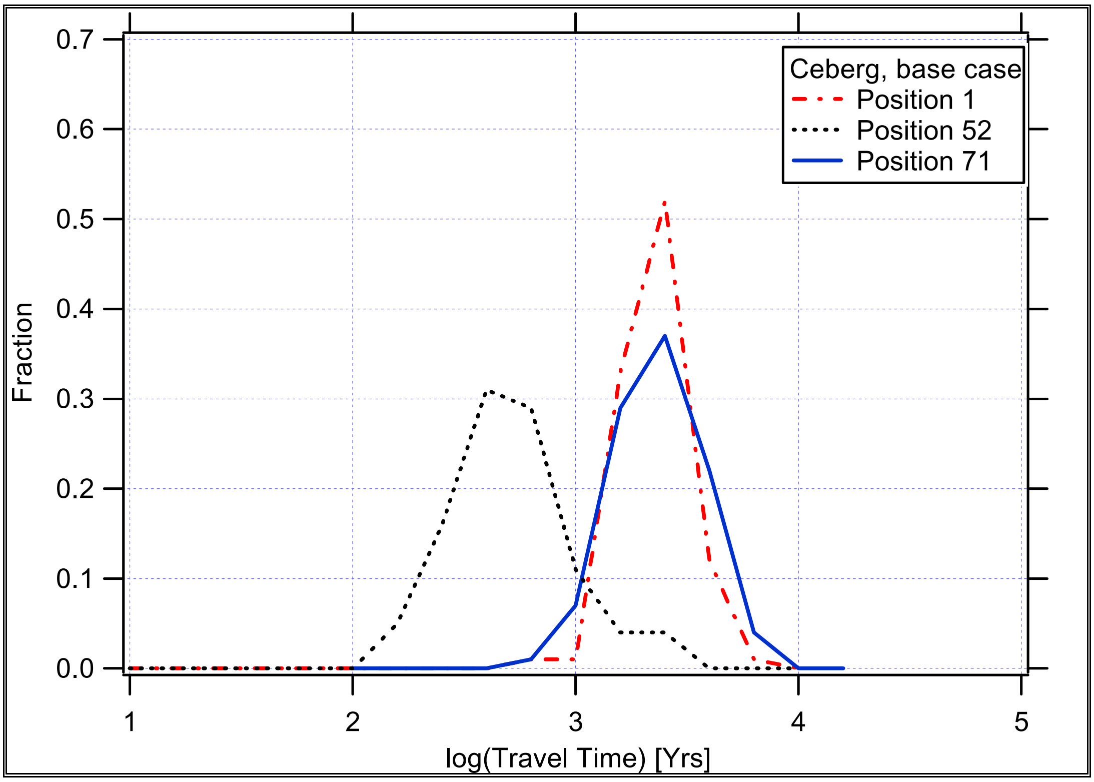

Figure 4.5-7. *Smoothed frequency histogram of* log_{10} *travel time for three starting positions in the Ceberg Base Case. Results are shown for 100 realisations and a flow porosity of* $\varepsilon_f = 1\times10^{-4}$.

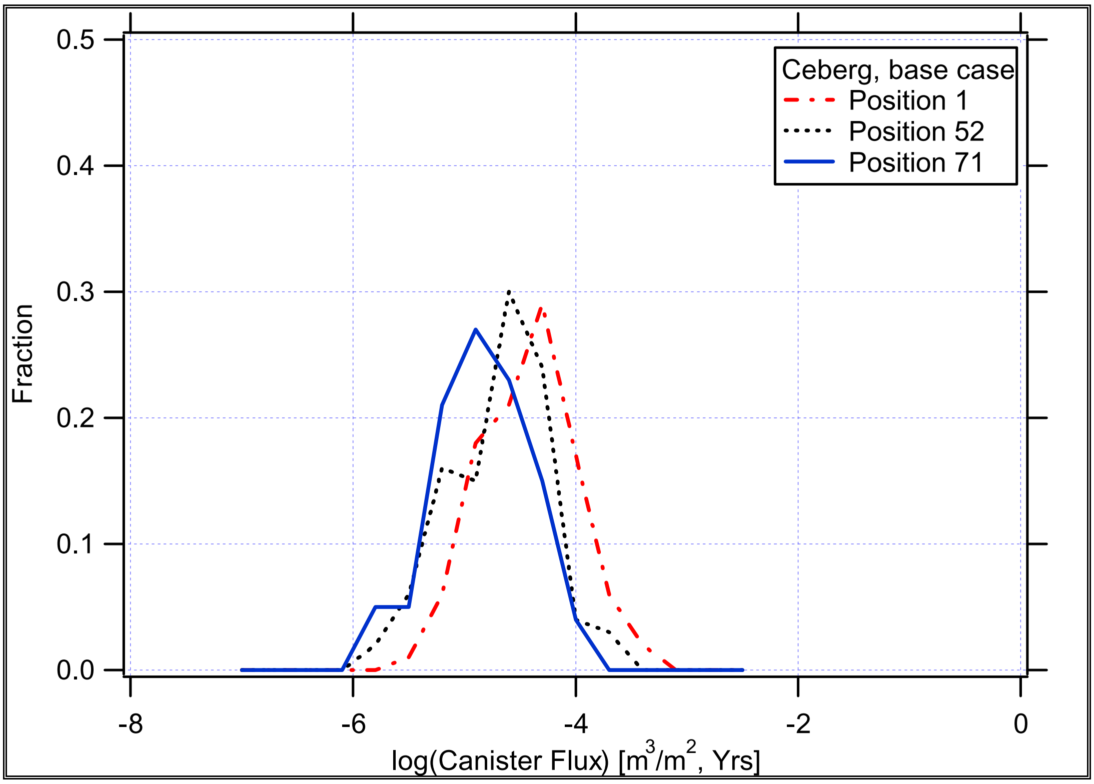

Figure 4.5-8. *Smoothed frequency histogram of* log_{10} *canister flux for three starting positions in the Ceberg Base Case. Results are shown for100 realisations.*

5 Variant Cases

Table 5-1 summarises the Base Case (the reference case for comparison) and the four variant cases evaluated for this study. Each of these variant simulations corresponds to a possible interpretation of the site hydrogeology. These are summarised as follows:

- Base Case: Based on expert opinion, this model represents the expected site conditions. This is the reference case for comparison to all other simulation results.
- Variant 1: Contrast between the conductor and rock domain (CD and RD) hydraulic conductivities increased by a factor of 100.
- Variant 2: Alternative conductive features.
- Variant 3: Increased variance of $\log_{10}$ hydraulic conductivity.
- Variant 4: Simulation with a deterministic hydraulic conductivity field.

The Base Case is thoroughly discussed in Section 4. The motivation behind each variant case is provided in the introductory section for each case. The results of each variant are briefly compared to the Base Case in terms of the median and interquartile ranges of the performance measures. A simple nonparametric hypotheses test determines the statistical significance of the similarity of the performance measure distributions (see Appendix A.2).

Table 5-1. Summary of Base and Variant Cases analysed in Ceberg site-scale modelling study.

Case	**Boundary Conditions**	**Hydraulic conductivity field**			**Remarks**
	Obtained from	**Geostatistical model**	**Hydraulic units**	**EDZ/Backfill**	
Base Case	**TR 97-21, case GRST**	**Exponential, isotropic model, Variance 1.12 Practical range 68 m**	**CD: SCD1** **RD: SRD6 (Walker et al., 1997b)**	**No/10^{-10} m/s**	
Variant #1 Increased Conductivity Contrast	TR 97-21 case GRSFH		K in all CD increased 100×		Case GRSFH: All deterministic CD increased by factor 100. (Note: TR 97-23 proposed only 4 zones, this study applies the increase to all zones
Variant #2 Alternative Conductive Features	New regional simulation case GRSFZ; see Appendix B		K in all CD increased 100×		Additional zones suggested by Saksa and Nummela (1998).
Variant #3 Increased Conductivity Variance		Variance of $\log_{10}$ hydraulic conductivity = 2.0			Corresponding to covariance model based on pooled data (SCD+SRD), i.e., larger variance
Variant #4 Deterministic		Variance of $\log_{10}$ hydraulic conductivity = 0			

5.1 Increased Conductivity Contrast

The Base Case model for the site has assumed that the hydraulic conductivity of the fracture zones is relatively similar to that of the rock mass. Although the values are derived from the available on-site hydraulic tests, this low contrast in hydraulic conductivity is unusual in comparison to the other SR 97 sites, Aberg and Beberg. Some shallow percussion holes and 25 m packer tests suggest that the zones can be quite conductive, even though the median hydraulic conductivity is quite low (Ahlbom et al., 1983; Walker et al., 1997b). It is therefore reasonable to evaluate the possibility that the hydraulic conductivity of the deterministic fracture zones is much higher than that of the rock mass (Ahlbom et al., 1983; Walker et al., 1997b; Hermanson et al., 1997).

As suggested in Walker et al. (1997b), the hydraulic conductivity of the rock mass remains unchanged, but the hydraulic conductivity of the fracture zones given in Table 3-1 is increased by a factor of 100. This variant is similar to that of SCD4 as suggested in Walker et al. (1997b), except that all the fracture zones have increased conductivity. Figure 5.1-1 presents a plot of one realisation of the hydraulic conductivities for this variant. The change in fracture conductivity might be expected to change the boundary fluxes and heads, requiring a different set of boundary conditions from the regional model. The regional model of Boghammar et al. (1997) included a corresponding simulation, GRSFH, which this variant uses for site-scale boundary conditions. The variant is otherwise unchanged from the Base Case, and uses 50 realisations.

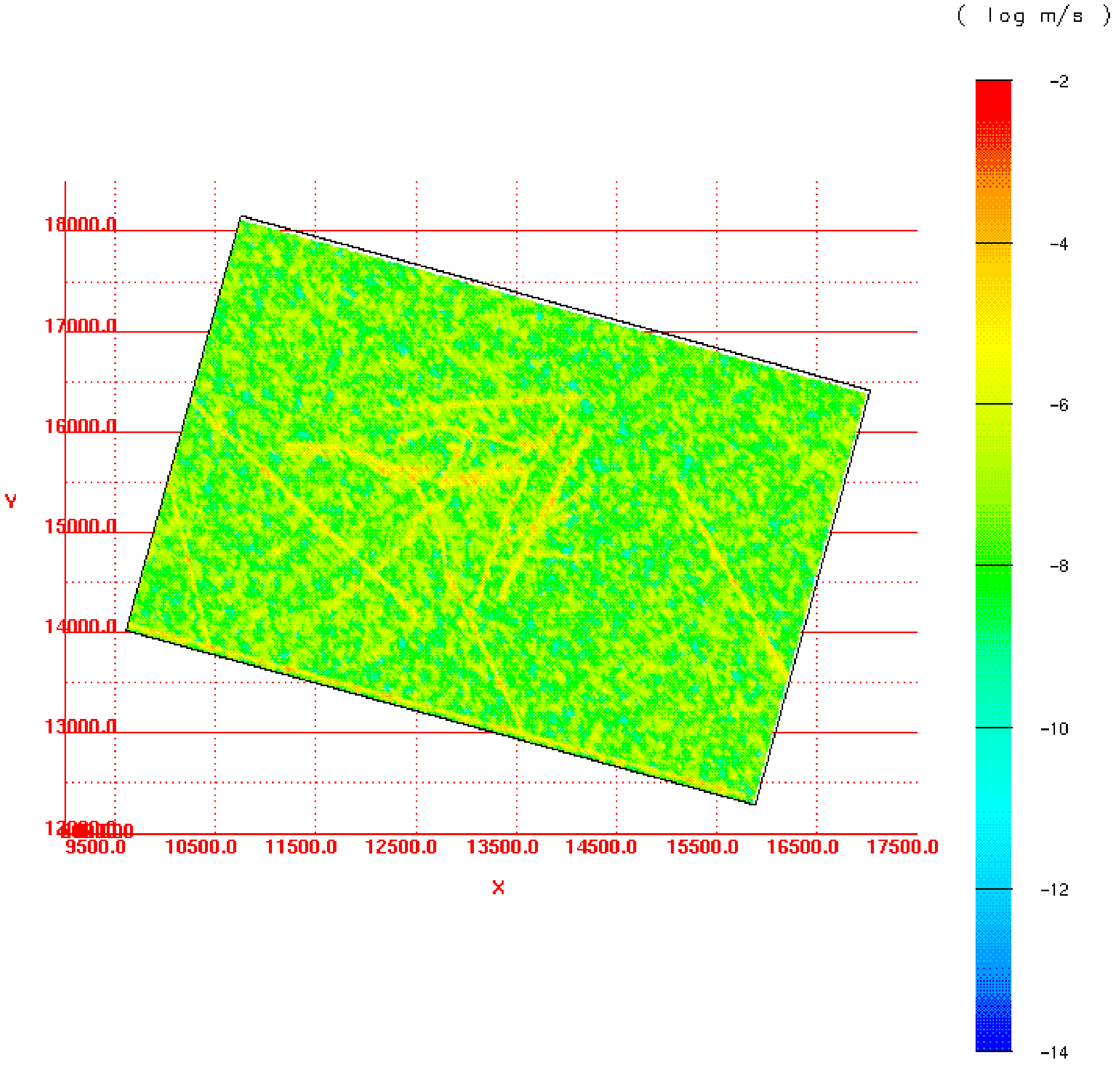

Figure 5.1-1. *Log$_{10}$ hydraulic conductivity in Ceberg Variant 1 (increased contrast) on the upper surface of realisation number 1 (plan view, with North in the y-positive direction, scale in metres).*

Table 5-2 summarises the results of this variant. Relative to the Base Case, the overall effect of increasing the conductivity of the fractures is to reduce the median travel time from 1720 to 998 years, and slightly increase the variance of log$_{10}$ travel time from 0.123 to 0.148. Figure 5.1-2 presents the histogram of log$_{10}$ travel time for this variant, which shows that the number of stream tubes with travel times greater than 100,000 years decreases to approximately 5%. There are statistically significant differences between the log$_{10}$ travel time distributions of this variant and the Base Case (Appendix A.2). The median and variance of log$_{10}$ canister flux for this variant are virtually unchanged relative to the Base Case, although there are statistically significant differences between the distributions of log$_{10}$ canister flux for this variant and the Base Case (Appendix A.2). The plot of log$_{10}$ travel time versus log$_{10}$ canister flux (Figure 5.1-3) shows a trace of correlation, similar to the Base Case.

Table 5-2. Summary statistics for Ceberg Variant 1 (increased contrast). Results are shown for 50 realisations of 119 starting positions, a flow porosity of $\varepsilon_f = 1\times10^{-4}$ and flow-wetted surface $a_r = 0.1$ m^2/(m^3 rock). Statistics in bold are discussed in the text. Approximately 5% of the stream tubes fail to reach the upper surface.

	All values			**Travel Times > 100,000 years deleted**		
	Log$_{10}$ t_w	**Log$_{10}$ q_c**	**Log$_{10}$ F-ratio**	**Log$_{10}$ t_w**	**Log$_{10}$ q_c**	**Log$_{10}$ F-ratio**
Mean	3.061	–4.411	6.061	2.974	–4.407	5.974
Median	3.021	**–4.423**	6.021	**2.999**	–4.419	**5.999**
Variance	0.311	**0.212**	0.311	**0.148**	0.212	**0.148**
5th percentile	2.306	–5.141	5.306	2.291	–5.135	5.291
25th percentile	2.747	–4.712	5.747	2.732	–4.709	5.732
75th percentile	3.291	–4.120	6.291	3.248	–4.114	6.248
95th percentile	3.765	–3.663	6.765	3.560	–3.655	6.560

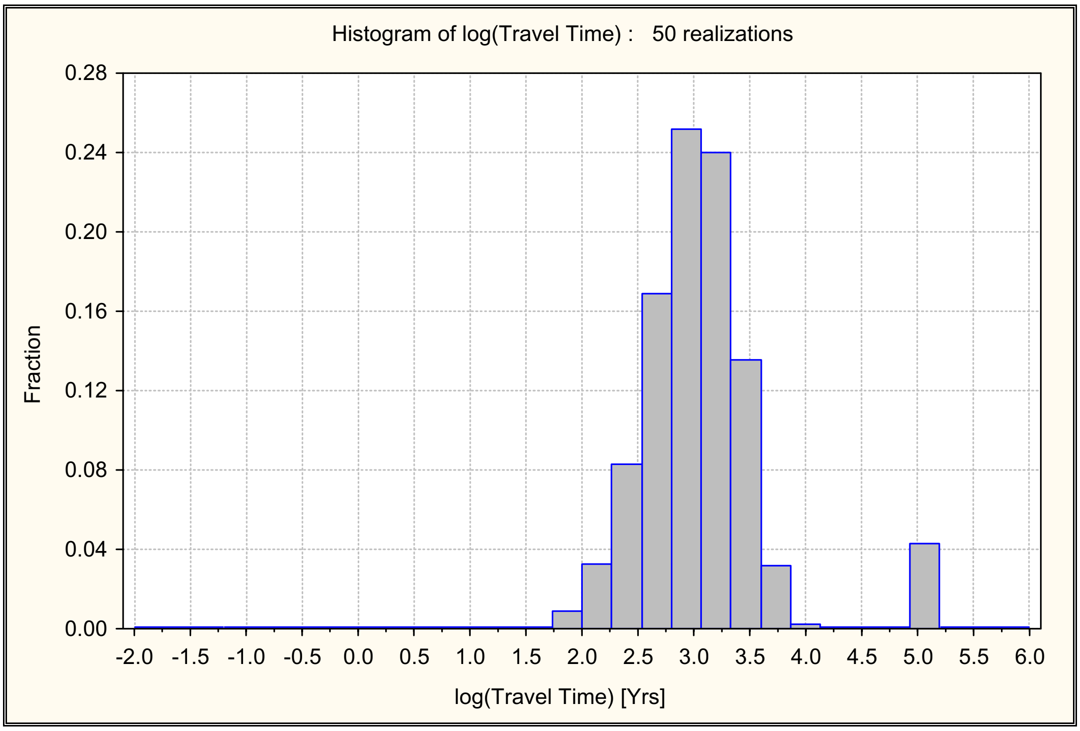

Figure 5.1-2. *Relative frequency histogram of $\log_{10}$ travel time for Ceberg Variant 1 (increased contrast). Results are shown for 50 realisations of 119 starting positions and a flow porosity of $\varepsilon_f = 1\times10^{-4}$.*

Table 5-3 presents a comparison of the net volumetric flow of water across the boundaries of the regional and site-scale models. The boundary flows for the site-scale model have increased by a factor of 2 from the Base Case, reflecting the increased flow in the deterministic fracture zones.

Table 5-3. Boundary flow consistency for Ceberg Variant 1 (increased contrast), regional model versus site-scale model.

	Net Flow Through Site Model Surfaces ($m^3/s \times 10^{-3}$)		
Model Surface	**Regional (GRSFH)**	**Variant 1 (5 realisations)**	**Base Case (5 realisations)**
West	28.3 (in)	0.683 (in)	0.289 (in)
East	16.8 (out)	0.227 (out)	0.150 (in)
South	110.0 (out)	1.90 (out)	0.920 (out)
North	3.84 (out)	0.101 (out)	0.0995 (out)
Bottom	0.0639 (out)	0.152 (in)	0.0221 (in)
Top	273.0 (in)	1.39 (in)	0.557 (in)
Total Inflow	301.3	2.23	1.02
Total Outflow	130.7	2.23	1.02
Mass balance (In – Out)	170.6	–0.003	–0.001

The regional model mass balance residual is greater than 100% of the total outflow from the site-scale domain. This error is attributed to the approximate mass balance calculation technique and is not directly related to the boundary heads calculated by the regional model.

To further investigate the boundary flows, this study constructs a mass balance for both the regional and site-scale models, omitting the upper 200 m of the domain (i.e., the upper surface of the mass balance control volume is lowered to –100 masl for both models). Table 5-4 summarises the results, which show that the regional and site-scale flows are within a factor of approximately 2. These results suggest that most of the discrepancy between the regional and site-scale models occurs in the near surface regions. This is attributed to mismatches in zone geometries and the use of calibrated conductivities in the near surface of the Boghammar et al. (1997) regional model. The regional mass balance residual is reduced to less than 40%, attributed to the approximate method for calculating flows within finite elements of the regional model. The regional mass balance residual of this variant is greater than the residual of the Base Case because the accuracy of the approximation method decreases with increasing hydraulic conductivity contrast (Section 4.2 and Appendix B.2).

These boundary flow comparisons for the reduced domain suggest that the nested modelling and the upscaling of hydraulic conductivity qualitatively preserve mass balance between the models.

Table 5.4. Boundary flow consistency over a reduced domain at z = –100 m for Ceberg Variant 1 (increased contrast), regional model versus site-scale model.

	Net Flow Through Site Model Surfaces ($m^3/s \times 10^{-3}$)	
Model Surface	**Regional (GRSFH)**	**Variant 1 (5 realisations)**
Total Inflow	0.467	0.169
Total Outflow	0.334	0.169
Mass balance (In – Out)	0.132	0.000

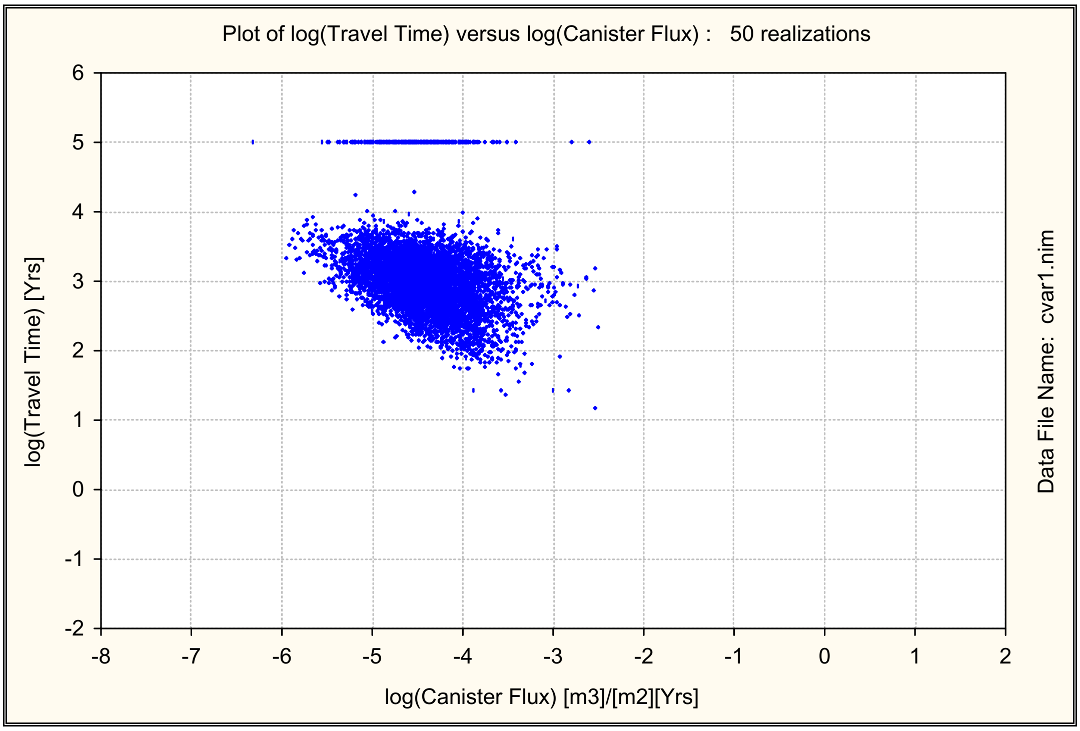

Figure 5.1-3. *Log_{10} travel time versus log_{10} canister flux for Ceberg Variant 1 (increased contrast). Results are shown for 50 realisations of 119 starting positions, and a flow porosity of $\varepsilon_f = 10^{-4}$.*

The stream tubes show increased organisation relative to the Base Case, tending to follow fracture zones to the South and North (Figure 5.1-4). The exit locations are also tightly arranged in areas where fracture zones intersect discharge areas. In the case of stream tubes exiting to the stream Husån, the increased conductivity of the fracture zones results in the exit locations being shifted 1 km west to the western side of the mire Stormyran (Figures 5.1-5).

The travel times, stream tubes and exit locations of this variant suggest that many of the travel paths are diverted and accelerated as a result of increasing the conductivity of the fracture zones. In addition to reducing the median travel times, this also tends to increase the variance of travel time, since not all stream tubes follow fracture zones. Increasing the fracture zone hydraulic conductivity appears to have little effect on the canister flux, since the fracture zones do not intersect the starting positions representing the hypothetical canisters.

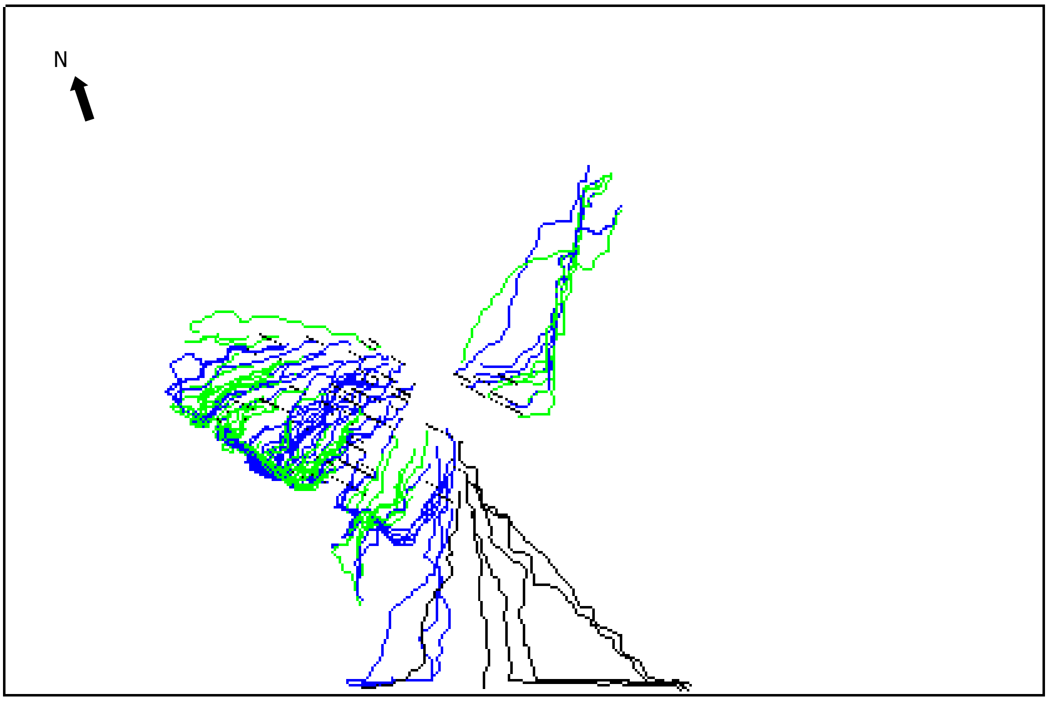

a) Plan view

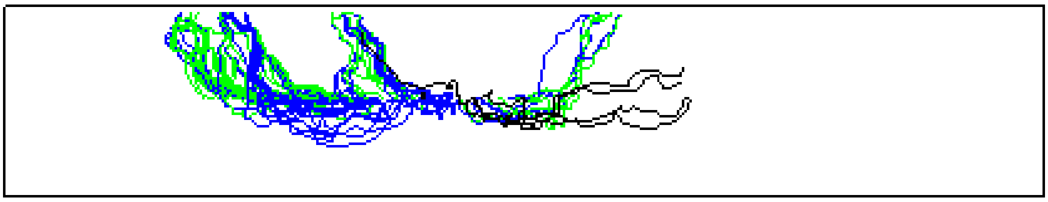

b) Elevation view, from South

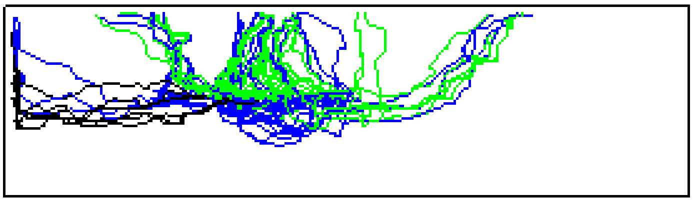

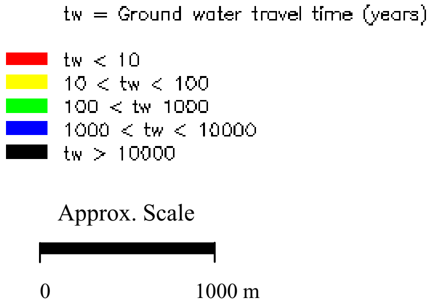

c) Elevation view, from East

Figure 5.1-4. *Stream tubes in realisation number 1 of Ceberg Variant 1 (increased contrast). The y-positive axis of a) is rotated 15 cw from North. Results are shown for 119 starting positions and a flow porosity of* $\varepsilon_f = 1\times10^{-4}$.

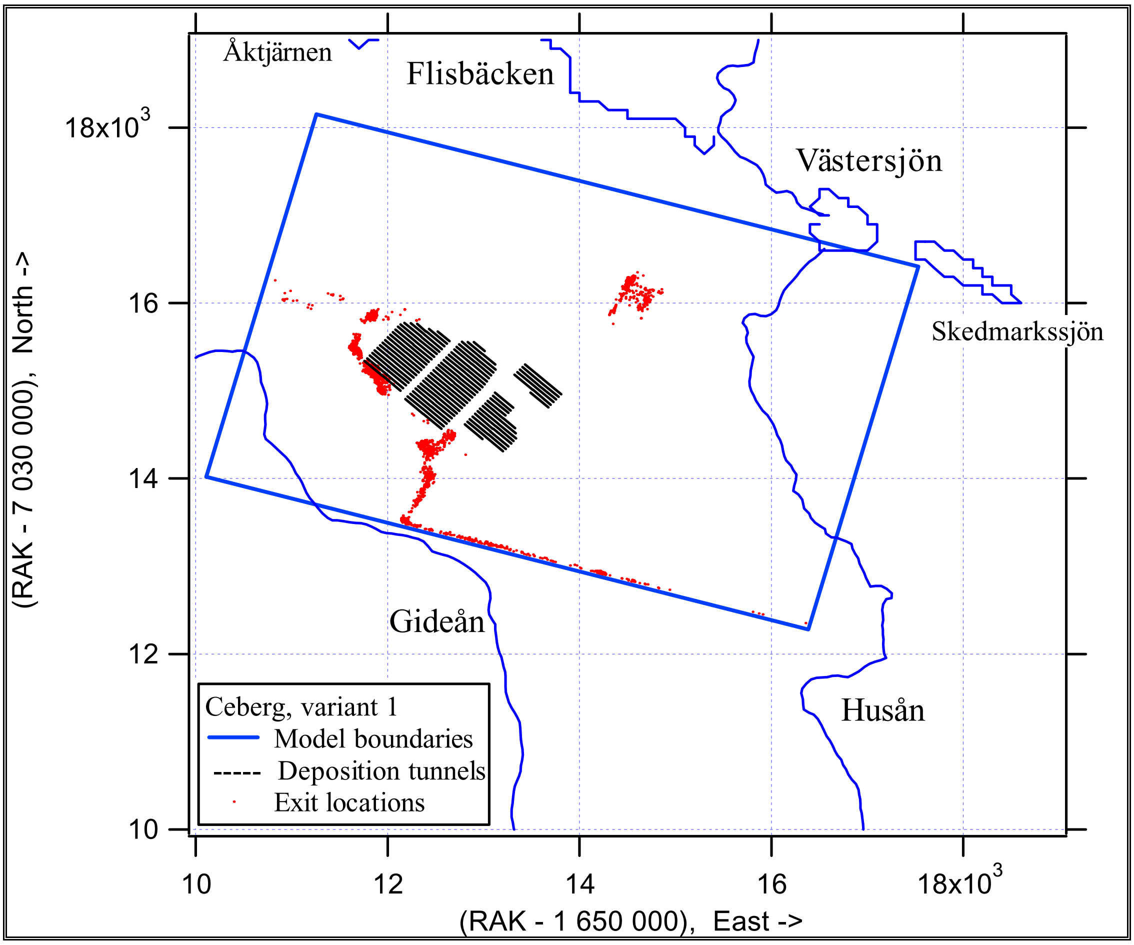

Figure 5.1-5. *Exit locations for Ceberg Variant 1 (increased contrast). Results are shown for 50 realisations of 119 starting positions (plan view, scale in metres).*

5.2 Alternative Conductive Features

In the site characterisation report, Ahlbom et al. (1983) suggests that the intrusive dolerite and pegmatite dykes may be conductive features, with hydraulic conductivities similar to the deterministic fracture zones. This has been questioned in later reports, since such a characterisation cannot be unambiguously supported from the packer test data (Hermanson et al., 1997). Similarly, Ahlbom et al. (1983) and Askling (1997) have mapped an extensive topographic lineament running north-northwest to south-southeast at the eastern margins of the site, which may be a fracture zone. However, the existence of a fracture zone at this location cannot be unambiguously supported from the geophysical data (Hermanson et al., 1997). As part of SR 97, Saksa and Nummela (1998) re-evaluated the site-scale structural model and suggested that both the intrusive dykes and the topographic lineament might reasonably be interpreted as conductive fracture zones.

This variant case evaluates the possibility that all of the fracture zones, the intrusive dykes and the topographic lineaments are highly conductive fracture zones. Similar to the variant discussed in Section 5.1, all of these features are assumed to have a hydraulic conductivity 100 times those given in Table 3-1. Positions of the dykes and the regional lineament are taken from Saksa and Nummela (1998) and are presented in Figure 3.5-2. This variant is similar to that of SCD3, as suggested in Walker et al. (1997b), except that this variant case includes all the intrusive dykes as well as the regional lineament. Because this additional regional lineament might change the boundary fluxes and heads, this variant requires a slightly different regional model than that used by the Base Case. The regional model of Boghammar et al. (1997) was rerun for this study to provide site-scale boundary conditions (Case GRSFZ, described in Appendix B). The variant is otherwise unchanged from the Variant 1, and uses 50 realisations.

Figure 5.2-1 presents the HYDRASTAR representation of the fracture zones used in this variant, and Figures 5.2-2 and 5.2-3 show the additional zones relative to the repository tunnels. These figures illustrate that the additional fracture zones are very close to the hypothetical repository, with one of the east-west trending dolerite dykes (Dolerite 1) running directly through the repository block. The utility program TRAZON checked the additional zones versus the starting positions (Appendix E). In contrast to the Base Case and all other variants, several starting positions fall into the conductive features of this variant. Seven starting positions, numbered 4, 9, 26, 39, 41, 54 and 56, fall into Dolorite 1 (Figure 3.4-2). Figure 5.2-4 presents one realisation of the resulting hydraulic conductivity field.

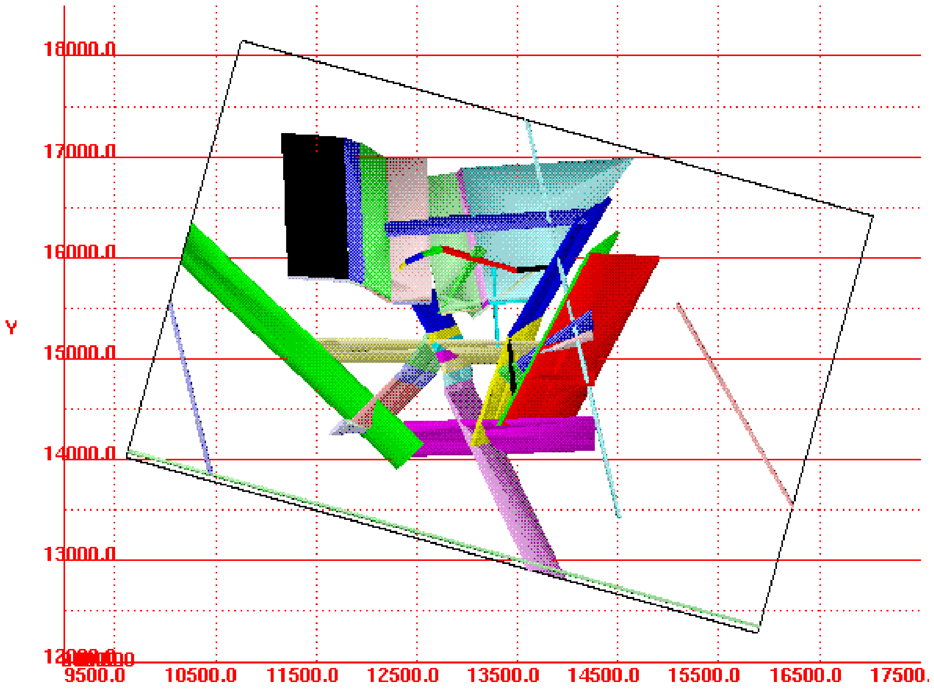

Figure 5.2-1. *HYDRASTAR representation of fracture zones in Ceberg Variant 2 (alternative conductors). (Plan view, with North in the y-positive direction, scale in metres).*

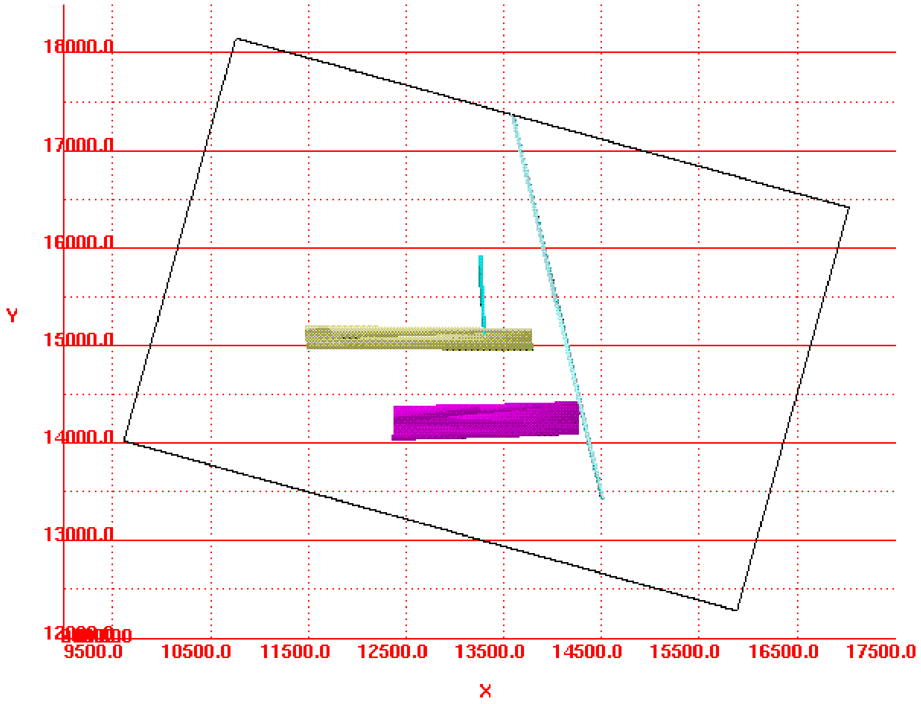

Figure 5.2-2. *HYDRASTAR representation of the four additional fracture zones in Ceberg Variant 2 (alternative conductors). (Plan view, with North in the y-positive direction, scale in metres).*

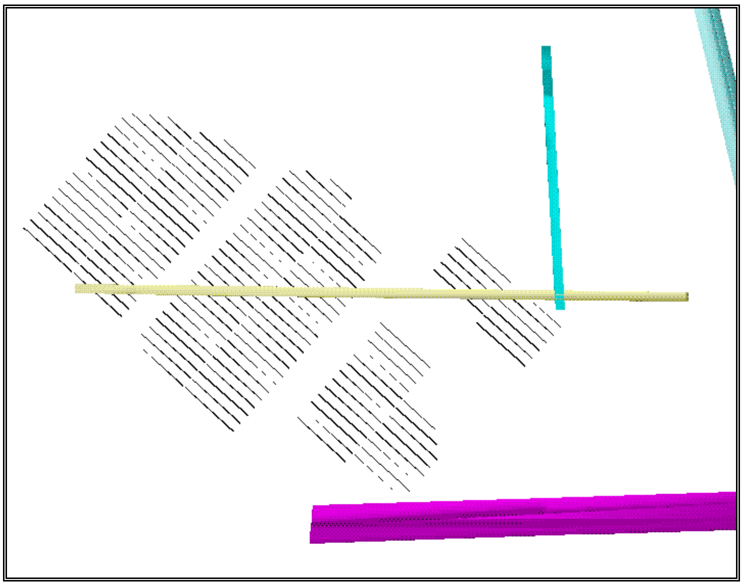

Figure 5.2-3. *The repository tunnels relative to the four additional fracture zones in Ceberg Variant 2 (alternative conductors). (Detail of Figure 5.2-2).*

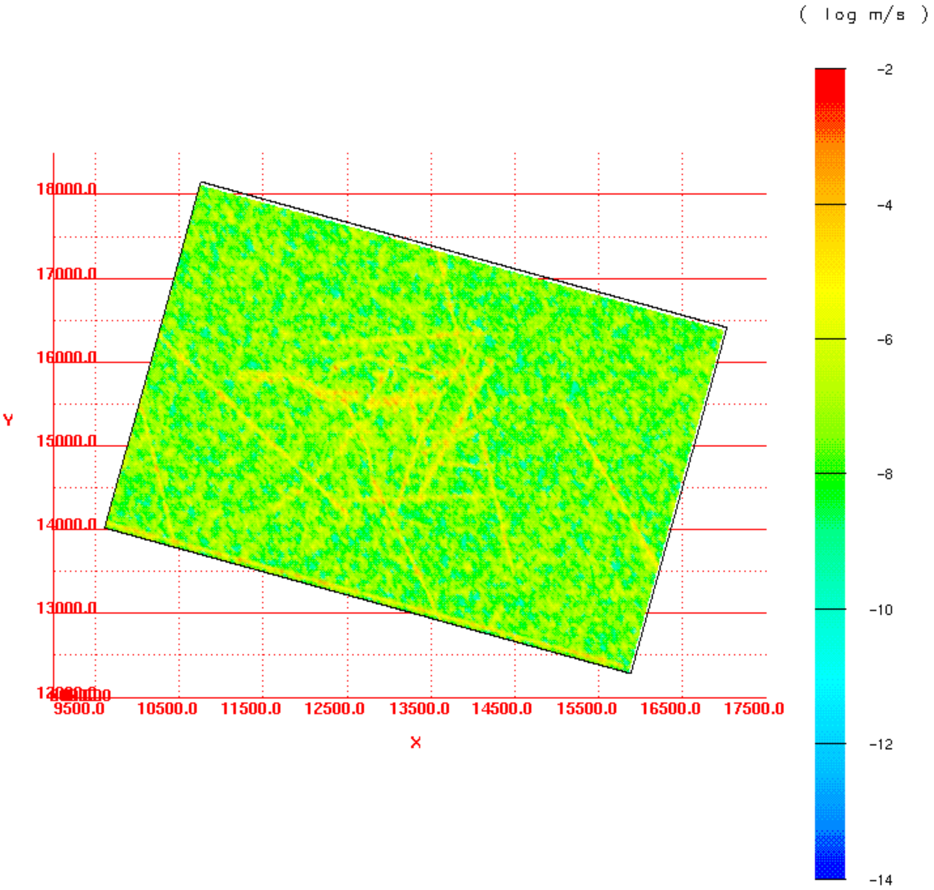

Figure 5.2-4. *Log$_{10}$ hydraulic conductivity field in Ceberg Variant 2 (alternative conductors) on the upper surface of realisation 1. (Plan view, with North in the y-positive direction, scale in metres).*

Table 5-5 summarises the effects of including the additional structures, where approximately 3.6% of the stream tubes fail to reach the upper surface. In comparison to the Base Case, the median travel time is reduced from 1720 to 800 years, and the variance of $\log_{10}$ travel time is increased from 0.123 to 0.307. These results are similar to those of Variant 1, where many of the stream tubes are intercepted by conductive features, decreasing the median of travel time while increasing the variance of $\log_{10}$ travel time. In this variant, the effect is stronger because one of the conductive features runs directly through the repository (Dolerite 1), creating a set of stream tubes that has a much faster travel time than the remainder of the set. The resulting $\log_{10}$ travel time distribution for this variant is markedly skewed and there are statistically significant differences between the $\log_{10}$ travel time distributions of this variant versus those of Variant 1 and the Base Case (Appendix A.2; Figure 5.2-5). Unlike Variant 1, the median canister flux is increased from 3.27×10^{-5} to 4.3×10^{-5} m/year, also a consequence of Dolerite 1 passing directly through the repository zone, intercepting seven starting

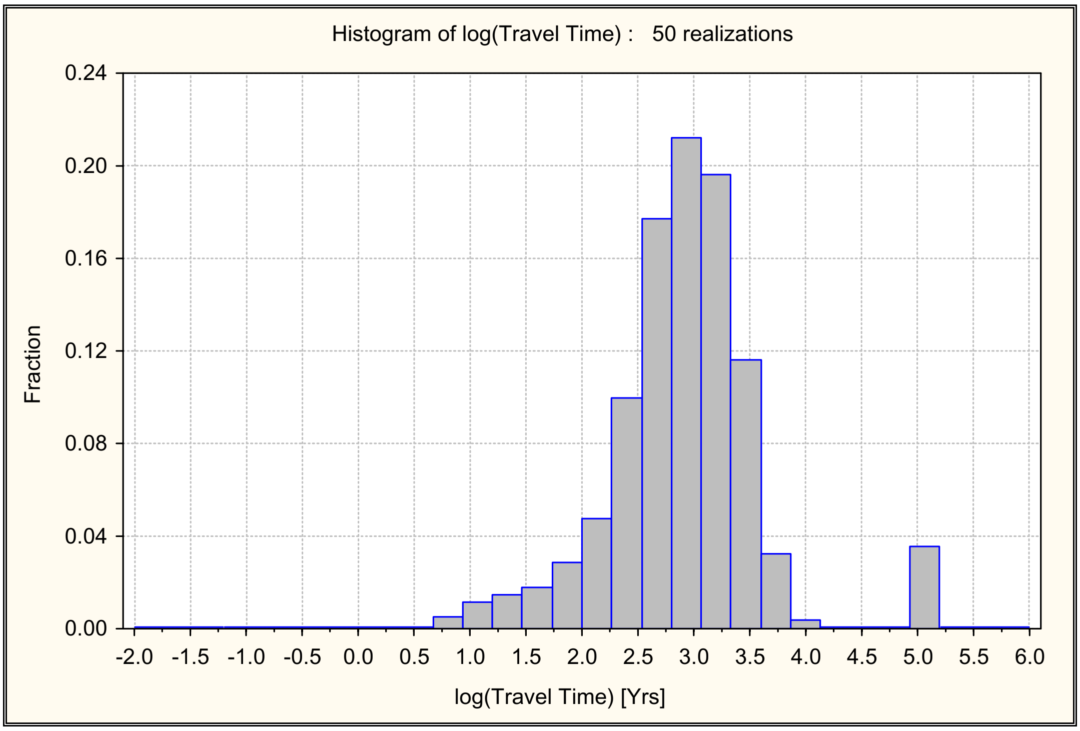

Figure 5.2-5. *Relative frequency histogram for $\log_{10}$ travel time in Ceberg Variant 2 (alternative conductors). Results are shown for 50 realisations of 119 starting positions and a flow porosity of $\varepsilon_f = 1\times10^{-4}$.*

Table 5-5. Summary statistics for Ceberg Variant 2 (alternative conductors). Results are shown for 50 realisations of 119 starting positions, a flow porosity of $\varepsilon_f = 1\times10^{-4}$ and flow-wetted surface $a_r = 0.1\ m^2/(m^3$ rock). Statistics in bold are discussed in the text. Approximately 3.6% of the stream tubes fail to reach the upper surface.

	All values			**Travel Times > 100,000 years deleted**		
	Log_{10} t_w	**Log_{10} q_c**	**Log_{10} F-ratio**	**Log_{10} t_w**	**Log_{10} q_c**	**Log_{10} F-ratio**
Mean	2.900	–4.255	5.900	2.823	–4.248	5.823
Median	2.925	**–4.367**	5.925	**2.903**	–4.363	**5.903**
Variance	0.459	**0.482**	0.459	**0.307**	0.484	**0.307**
5th percentile	1.737	–5.143	4.737	1.720	–5.141	4.720
25th percentile	2.576	–4.698	5.576	2.563	–4.690	5.563
75th percentile	3.239	–3.991	6.239	3.199	–3.983	6.199
95th percentile	3.729	–2.678	6.729	3.552	–2.672	6.552

positions. (See also Section 3.4). This results in statistically significant differences between the $\log_{10}$ canister flux distributions of this variant versus those of the remaining variants and the Base Case (Appendix A.2). Figure 5.2-6 shows that the travel times and canister fluxes are slightly correlated in this variant.

Table 5-6 presents a comparison of the net volumetric flows across the boundaries of the regional and site-scale models. The results are very similar to those of Variant 1, i.e., the boundary flows have increased by a factor of 2 from the Base Case. The regional model has a residual of more than 150% of the total outflow from the site-scale domain. Although this error can be rationalised as not being directly related to the boundary heads calculated by the regional model, the errors should be examined.

Table 5-6. Boundary flow consistency for Ceberg Variant 2 (alternative conductors), regional model versus site-scale models.

	Net Flow Through Site Model Surface ($m^3/s \times 10^{-3}$)		
Model Surface	**Regional (GRSFZ)**	**Variant 2 (5 realisations)**	**Base Case (5 realisations)**
West	27.5 (in)	0.693 (in)	0.289 (in)
East	17.6 (out)	0.228 (out)	0.150 (in)
South	103. (out)	1.92 (out)	0.920 (out)
North	3.77 (in)	0.141 (out)	0.0995 (out)
Bottom	0.0752 (out)	0.178 (in)	0.0221 (in)
Top	289. (in)	1.41 (in)	0.557 (in)
Total Inflow	320.3	2.28	1.02
Total Outflow	120.7	2.28	1.02
Mass balance (In – Out)	200.0	–0.008	–0.0014

To examine the flow balance further, this study constructs a flow balance for both the regional and site-scale models for a reduced domain that omits the upper 200 m of the domain (i.e., the upper surface of the flow balance control volume is lowered to –100 masl for both models). Table 5-7 summarises the results, which show that the regional and site-scale flows are within a factor of 2. These results suggest that most of the discrepancy between the regional and site-scale models occurs in the near-surface regions. This is attributed to mismatches in zone geometries and the use of calibrated conductivities in the near-surface of the Boghammar et al. (1997) regional model. The regional flow balance residual of approximately 70% is attributed to the approximate method for calculating flows within finite elements of the regional model (Section 4.2 and Appendix B.2)

These boundary flow comparisons suggest that the nested modelling and the upscaling of hydraulic conductivity preserves mass between the models only in the most general sense. Further discussion of the flow balance calculations can be found in Section 5.4 (regarding the Deterministic Variant).

Table 5-7. Boundary flow consistency over reduced domain at z =–100 m for Ceberg Variant 2 (alternative conductors), regional model versus site-scale model.

	Net Flow Through Site Model Surfaces ($m^3/s \times 10^{-3}$)	
Model Surface	**Regional (GRSFZ)**	**Variant 2 (5 realisations)**
Total Inflow	0.498	0.196
Total Outflow	0.304	0.196
Mass balance (In – Out)	0.194	0.000

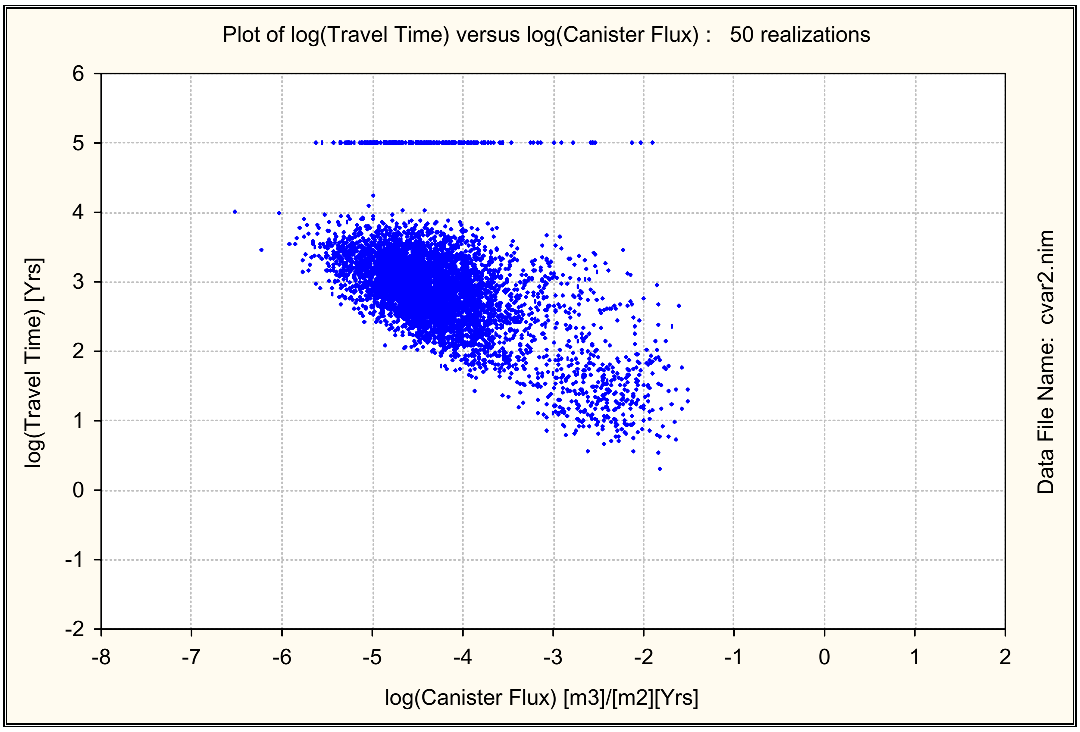

Figure 5.2-6. *Log$_{10}$ travel time versus log$_{10}$ canister flux for Ceberg Variant 2 (alternative conductors). Results are shown for 50 realisations of 119 starting positions and a flow porosity of $\varepsilon_f = 1\times10^{-4}$.*

Similar to Variant 1, the stream tubes show increased organisation relative to the Base Case, tending to follow fracture zones to the South and North (Figure 5.2-7). The exit locations are also tightly arranged in areas where fracture zones intersect discharge areas. In the case of stream tubes exiting to the stream Husån, the increased conductivity of the fracture zones results in the exit locations being shifted 1 km west to the western side of the mire Stormyran (Figures 5.2-8).

The travel times, stream tubes and exit locations of this variant suggest that many of the travel paths are diverted and accelerated as a result of increasing the conductivity of the fracture zones. In addition to reducing the median travel times, this also tends to increase the variance of travel time, since not all stream tubes follow fracture zones. Comparing the results to Variant 1, the canister flux effects of this variant are attributed to the dolerite dykes intersecting the starting positions representing the hypothetical canisters. The results of Variants 1 and 2 taken together suggest that reasonable assumptions regarding the occurrence, extent and properties of the conductive features may have a strong impact on the performance assessment.

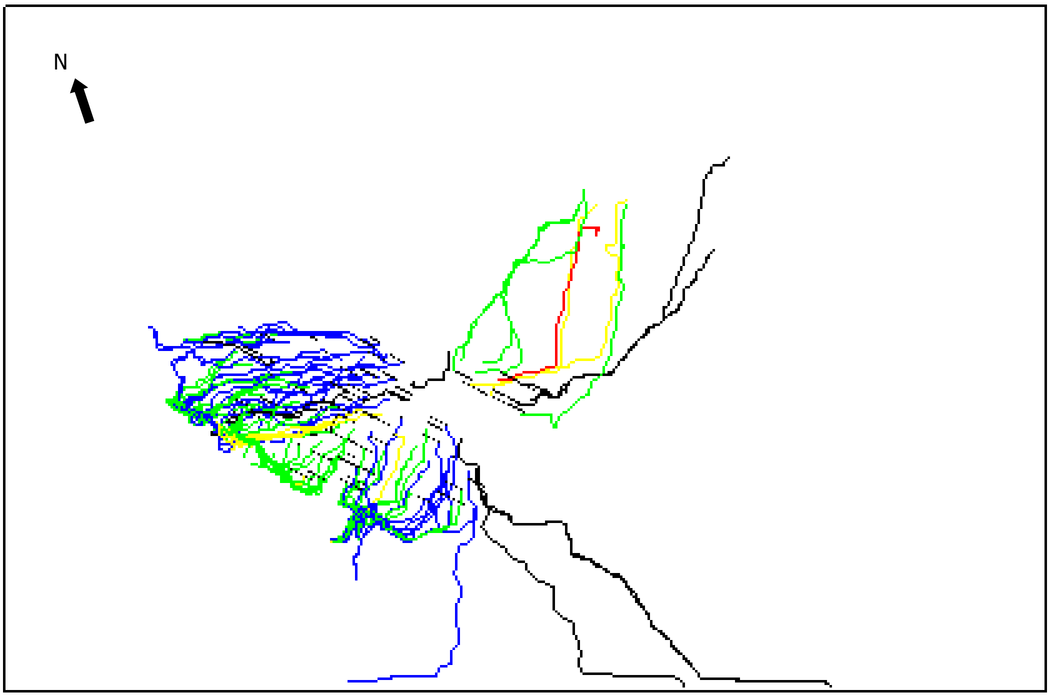

a) Plan view

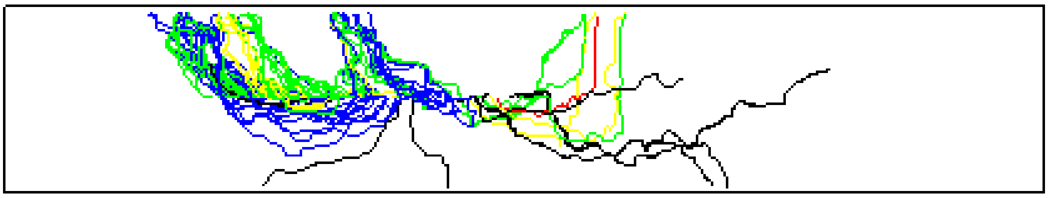

b) Elevation view, from South

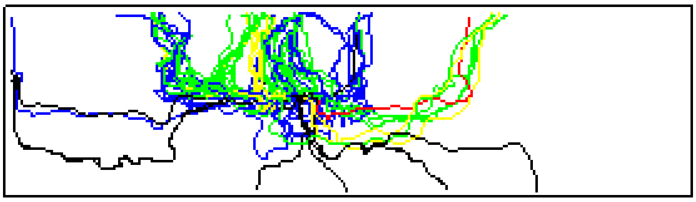

c) Elevation view, from East

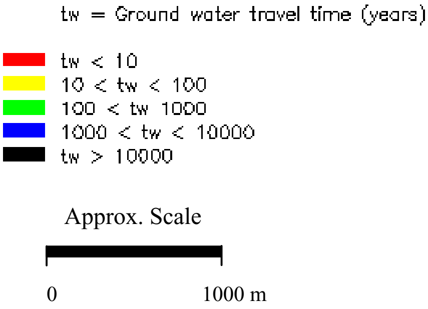

Figure 5.2-7. *Stream tubes in realisation number 1 of Ceberg Variant 2 (alternative conductors). The y-positive axis of a) is rotated 15 cw from North. Results are shown for 119 starting positions and a flow porosity of* $\varepsilon_f = 1\times10^{-4}$.

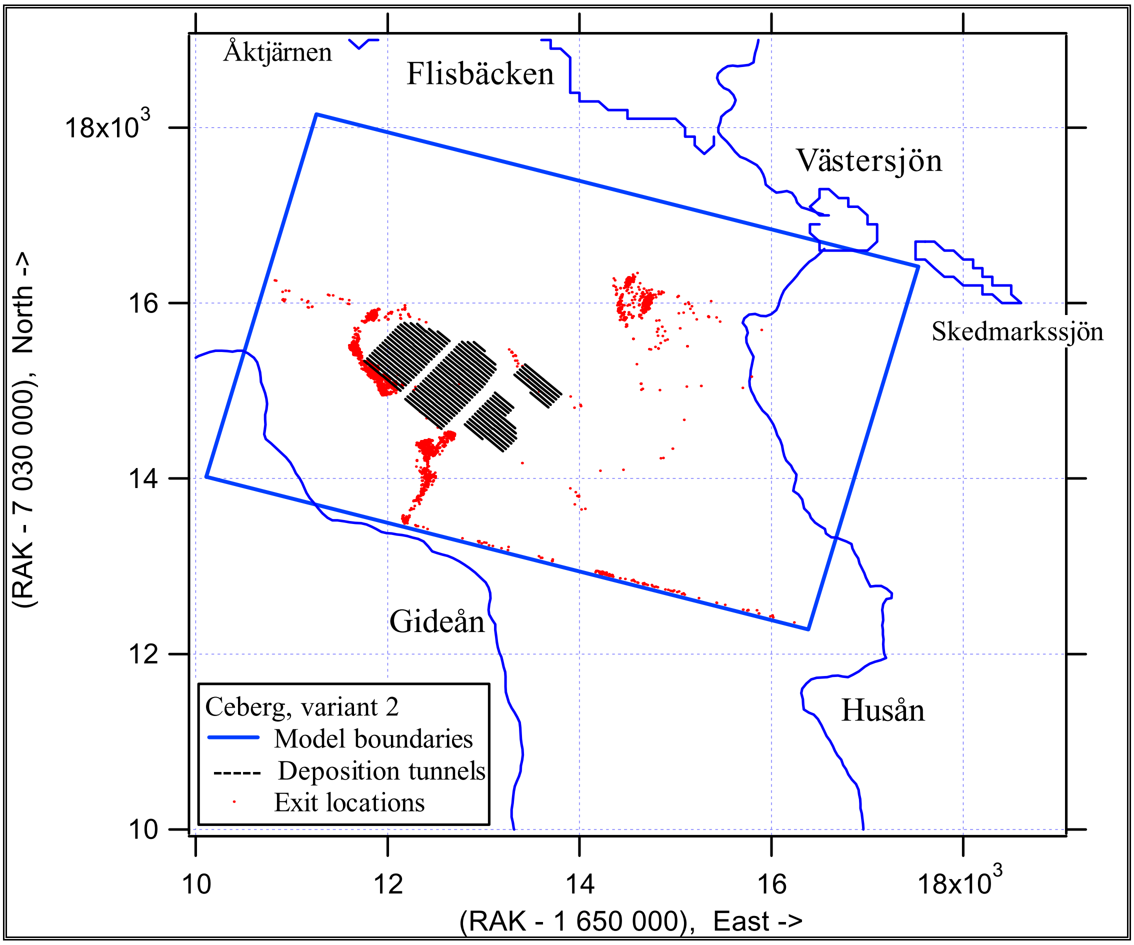

Figure 5.2-8. *Exit locations for Ceberg Variant 2 (alternative conductors). Results are shown for 50 realisations of 119 starting positions (plan view, scale in metres).*

5.3 Increased Conductivity Variance

The Base Case geostatistical model was inferred from the packer test data in the rock mass domain (SRD), resulting in a $\log_{10}$ hydraulic conductivity variance of 1.12 (Appendix C). It is possible that using the SRD data separately may have underestimated the variance; for example, the pooled data set of SRD and SCD data has a variance of 2.5 (Walker et al, 1997b). The simulations in Variant 3 were performed with a $\log_{10}$ hydraulic conductivity variance of 2.0 to evaluate the impacts of this uncertainty. This variant is otherwise unchanged from the Base Case, including the fact that the same mean $\log_{10}$ hydraulic conductivities are used for this variant as for the Base Case.

Figure 5.3-1 presents one realisation of the resulting hydraulic conductivity field. Because the increased variance may reduce the stability of the Monte Carlo simulations, it is important to check the stability of the statistics of interest versus the number of realisations. Figure 5.3-2 presents a plot of the median of $\log_{10}$ travel time. The figure shows little change in the estimates beyond 30 realisations.

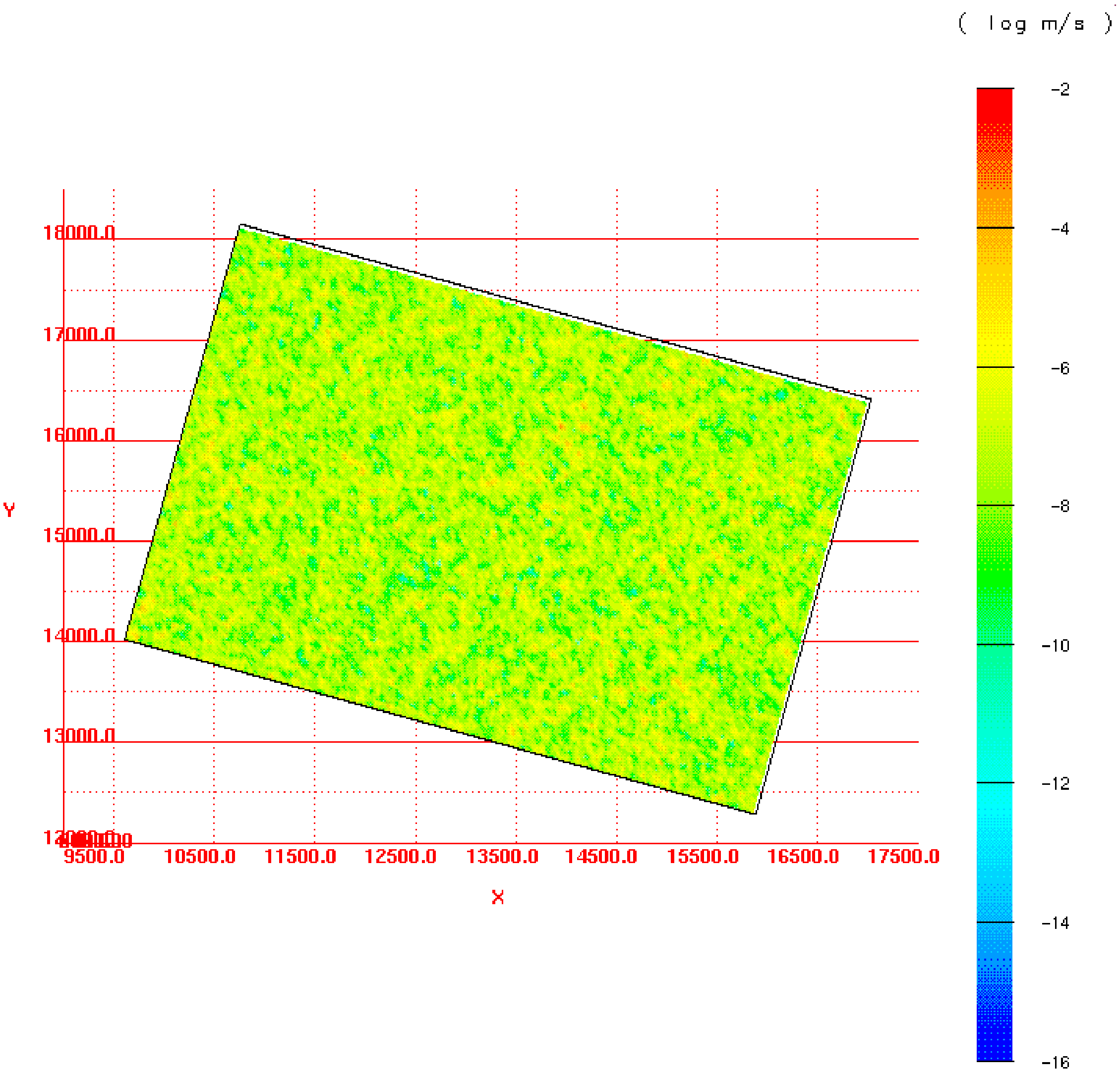

Figure 5.3-1. *Log$_{10}$ hydraulic conductivity in Ceberg Variant 3 (increased variance) on the upper surface of realisation number 1 (plan view, with North in the y-positive direction, scale in metres).*

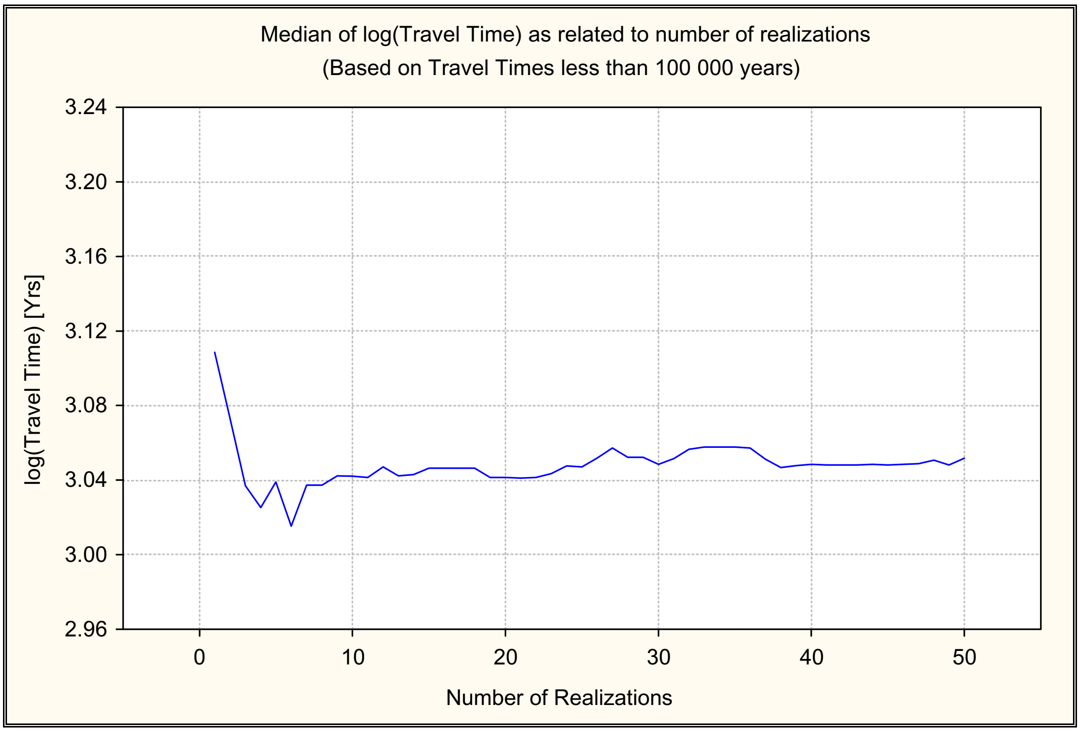

Figure 5.3-2. *Monte Carlo stability of median travel time for Ceberg Variant 3 (increased variance). Results shown for a flow porosity of* $\varepsilon_f = 1\times10^{-4}$.

Table 5-8 summarises the results of this simulation. Relative to the Base Case, the variance of $\log_{10}$ travel time increases from 0.123 to 0.156 and variance of $\log_{10}$ canister flux increases from 0.182 to 0.295. The median $\log_{10}$ travel time decreases from 1720 to 1130 years, and the median $\log_{10}$ canister flux increases from 3.27×10^{-5} m/year to 4.59×10^{-5} m/year. Approximately 11% of the stream tubes fail to reach the upper surface.

Table 5-8. Summary statistics for Ceberg Variant 3 (increased variance). Results are shown for 50 realisations of 119 starting positions, a flow porosity of $\varepsilon_f = 1\times10^{-4}$ and flow-wetted surface $a_r = 0.1$ m²/(m³ rock). Statistics in bold are discussed in the text. Approximately 11% of the stream tubes fail to reach the upper surface.

	All values			**Travel Times > 100,000 years deleted**		
	$\log_{10} t_w$	**$\log_{10} q_c$**	**$\log_{10}$ F-ratio**	**$\log_{10} t_w$**	**$\log_{10} q_c$**	**$\log_{10}$ F-ratio**
Mean	3.258	–4.351	6.258	3.038	–4.350	6.038
Median	3.117	**–4.338**	6.117	**3.052**	–4.337	**6.052**
Variance	0.522	**0.295**	0.522	**0.156**	0.296	**0.156**
5th percentile	2.403	–5.268	5.403	2.382	–5.264	5.382
25th percentile	2.808	–4.709	5.808	2.764	–4.710	5.764
75th percentile	3.439	–3.962	6.439	3.314	–3.955	6.314
95th percentile	5.000	–3.485	8.000	3.671	–3.481	6.671

These reflect the statistically significant differences between distributions of this variant and the Base Case for both $\log_{10}$ travel time and $\log_{10}$ canister flux (Appendix A.2; Figure 5.3-3). Log_{10} travel time and $\log_{10}$ canister flux appear to be slightly correlated, but little different from the Base Case (Figure 5.3-4). The stream tubes and exit locations (Figures 5.3-5 and 5.3-6) appear to be organised along fracture zones, similar to Variant 2.

Although the increased variances can be explained as the result of the increased variance of $\log_{10}$ hydraulic conductivity, the decreased travel times, increased canister flux, and increased boundary flows indicate an overall increase in hydraulic conductivity. A hueristic explanation for this apparent increase is provided by the Gutjahr et al. (1978) solution for the effective conductivity of an isotropic domain:

$$K_e = K_g \left[1 + \frac{\sigma^2_{\ln K}}{6} \right]$$

Where K_e is the effective hydraulic conductivity of the domain, K_g is the geometric mean of point values of hydraulic conductivity (K) within the domain, and $\sigma^2_{\ln K}$ is the variance of lnK. (Dagan, 1993, and Abramovich and Indelman, 1995, discuss higher order approximations). This relationship suggests that increasing only the variance of hydraulic conductivity increases the overall conductivity of the domain, and thus we should expect increased fluxes and decreased travel times.

Table 5-9 indicates that the boundary flows through the domain appear to be increased by a factor of 3, confirming that the increased variance has resulted in an increased effective conductivity. The boundary flow comparison also indicates that the site-scale model underpredicts the regional model flows by a factor of seven. There is also a 10% regional mass balance residual. Although this error can be rationalised as not being directly related to the boundary heads calculated by the regional model, the high error should be examined.

To further investigate the boundary flows, this study constructs a mass balance for both the regional and site-scale models for domain that omits the upper 200 m of the domain (i.e., the upper surface of the mass balance control volume is lowered to –100 masl for both models). Table 5-10 summarises the results, which show that the regional flows are closely approximated by the site-scale flows. These results suggest that most of the discrepancy between the regional and site-scale models occurs in the near surface regions. This is attributed to mismatches in zone geometries and the use of calibrated conductivities in the near surface of the Boghammar et al. (1997) regional model. The regional mass balance residual is reduced to approximately 6% and is attributed to the approximate method for calculating mass balance within finite elements of the regional model (Section 4.1 and Appendix B.2).

Table 5-9. Boundary flow consistency for Ceberg Variant 3 (increased variance) versus Base Case and regional model.

Model Surface	Net Flow Through Site Model Surfaces ($m^3/s \times 10^{-3}$) Regional (GRST)	Base Case Site-Scale	Variant 3 Site-scale
West	2.59 (in)	0.289 (in)	0.453 (in)
East	2.25 (in)	0.150 (in)	0.496(in)
South	16.7 (out)	0.920 (out)	3.23 (out)
North	3.84 (out)	0.0995 (out)	0.451 (in)
Bottom	0.00279 (out)	0.0221 (in)	0.0411 (in)
Top	17.7 (in)	0.557 (in)	1.79(in)
Total Inflow	22.54	1.02	3.23
Total Outflow	20.54	1.02	3.23
Mass balance (In – Out)	2.00	–0.001	–0.002

Table 5-10. Boundary flow consistency for a reduced domain at z = –100 m for Ceberg Variant 3 (increased variance), regional model versus site-scale model.

Model Surface	Net Flow Through Site Model Surfaces ($m^3/s \times 10^{-3}$) Regional (GRST)	Variant 3 (5 realisations)
Total Inflow	0.0413	0.0467
Total Outflow	0.0390	0.0467
Mass balance (In – Out)	0.0023	0.0000

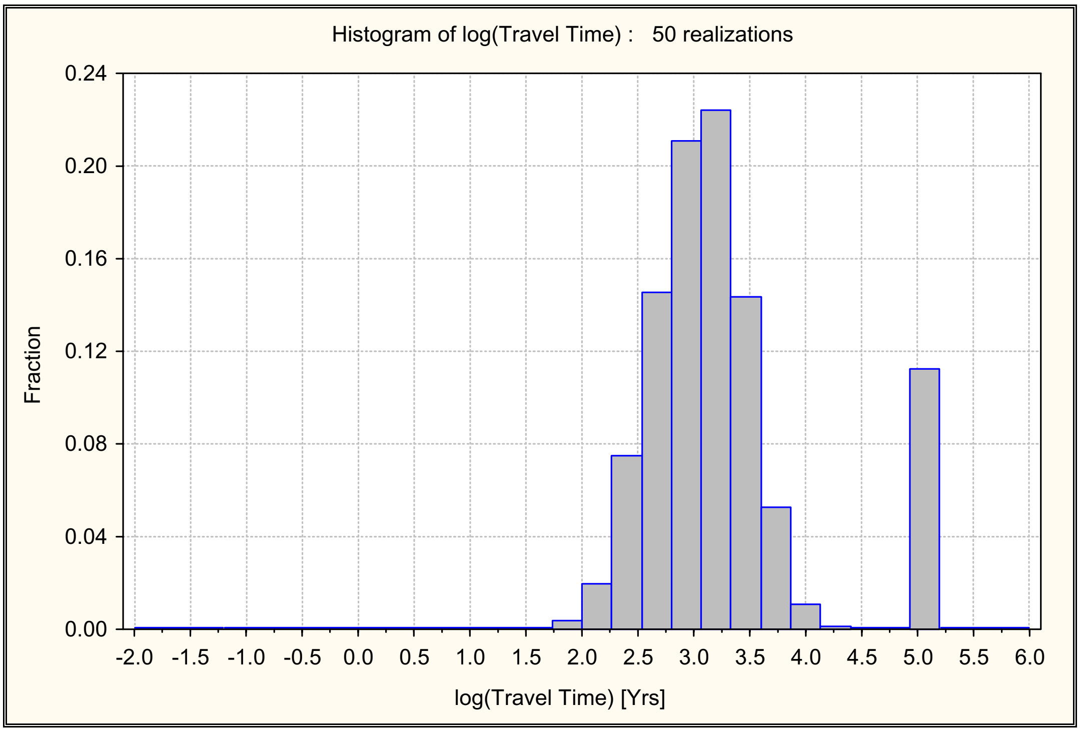

Figure 5.3-3. *Relative frequency histogram for* $\log_{10}$ *travel time for Ceberg Variant 3 (increased variance). Results are shown for 50 realisations of 119 starting positions and a flow porosity of* $\varepsilon_f = 1\times10^{-4}$.

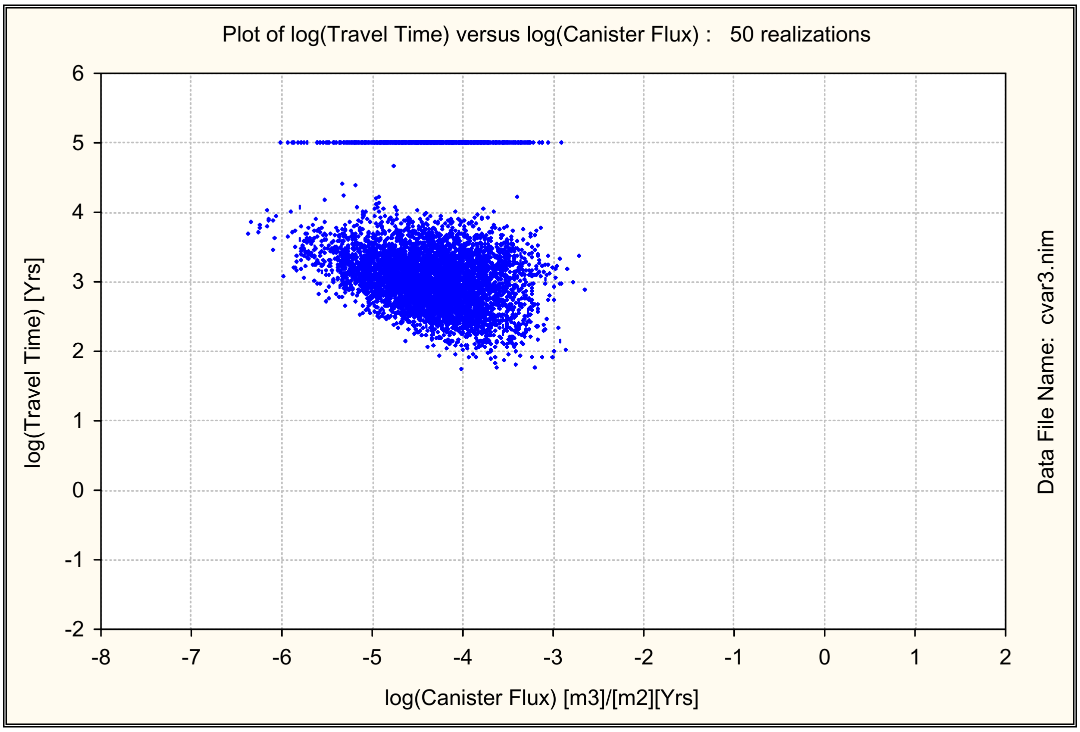

Figure 5.3-4. $\log_{10}$ *travel time versus* $\log_{10}$ *canister flux for Ceberg Variant 3 (increased variance). Results are shown for 50 realisations of 119 starting positions and a flow porosity of* $\varepsilon_f = 1\times10^{-4}$.

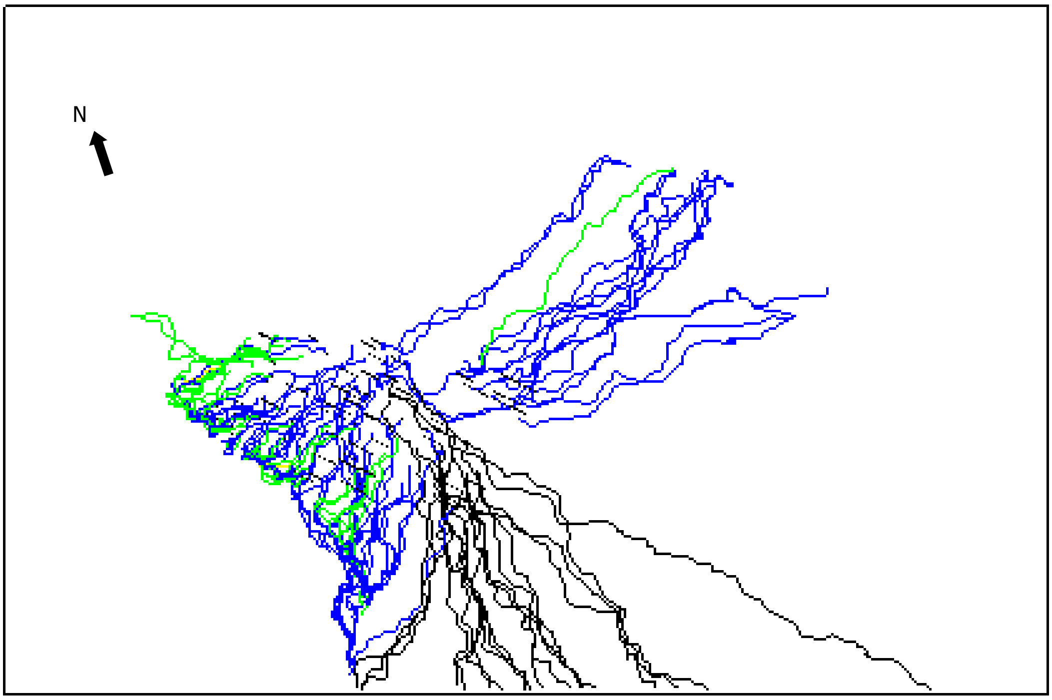

a) Plan view

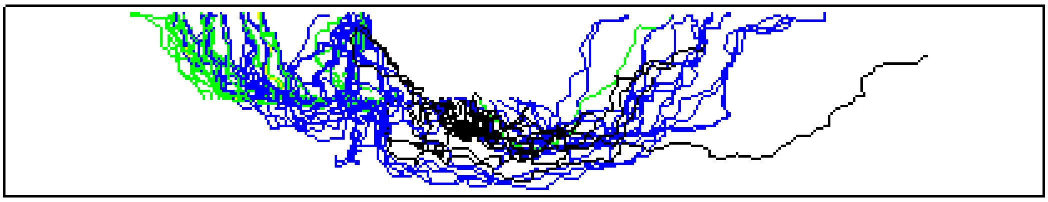

b) Elevation view, from South

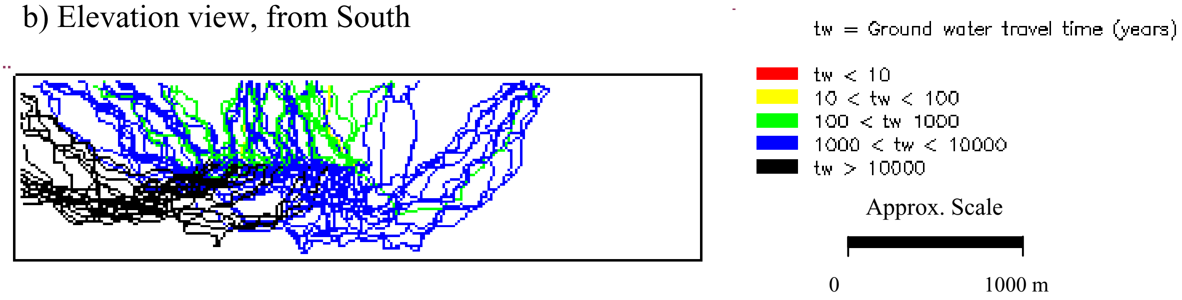

c) Elevation view, from East

Figure 5.3-5. *Stream tubes in realisation number 1 of Ceberg Variant 3 (increased variance). The y-positive axis of a) is rotated 15 cw from North. Results are shown for 119 starting positions and a flow porosity of* $\varepsilon_f = 1\times10^{-4}$.

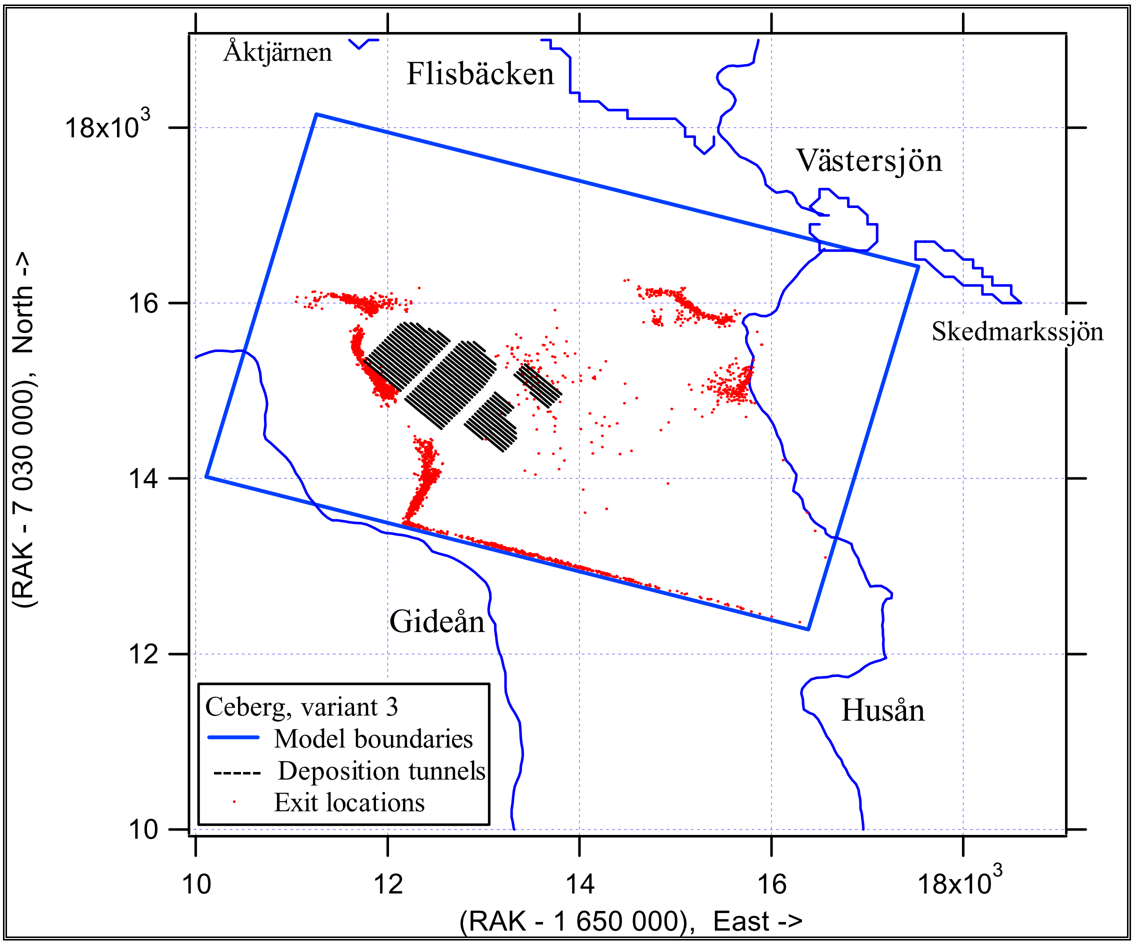

Figure 5.3-6. *Exit locations for Ceberg Variant 3 (increased variance). Results are shown for 50 realisations of 119 starting positions (plan view, scale in metres).*

5.4 Deterministic Simulation

This variant is a simplified representation of the site using a deterministic hydraulic conductivity field (i.e., the field has no random component and thus requires only one ‘realisation’). The objectives of this simulation are to further evaluate the empirical upscaling and nested modelling, and to examine the effects of the large-scale heterogeneity (e.g., the fracture zones and rock blocks). As was discussed in Sections 4.2, 5.1 and Appendix C.1, choosing the appropriate hydraulic conductivities is complicated by the apparent scale dependence of hydraulic conductivity. This study uses the empirical upscaling rule (Appendix C.1) to determine the effective conductivity, K_e, for the SRD and each SCD. If the nested modelling and upscaling are consistent, the boundary flows, travel times and canister fluxes should be approximately the same for both the Base Case and this Deterministic Variant.

Table 5-11 presents the effective conductivities of each unit. Note that for this variant, there is no block-scale variability (zero variance, thus no spatial variability of hydraulic conductivity except for the contrast between the rock domain and conductor domain). Figure 3.5-5 shows the deterministic field.

Table 5-11. Ceberg deterministic model for hydraulic conductivity, with 25 m measurements and 35 m grid scale shown for comparison. Upscaled as in Appendix C.1.

Elevation (masl)	25 m Mean Log_{10} K (m/s)	35 m Mean Log_{10} K (m/s)	Deterministic (100 m) Log_{10} K (m/s)
SCD			
+110 to 0	–7.0	–6.9	–6.4
0 to –100	–8.5	–8.4	–7.9
–100 to –300	–9.5	–9.4	–8.9
Below –300	–9.7	–9.6	–9.1
SRD			
+110 to 0	–7.6	–7.4	–7.2
0 to –100	–9.0	–8.9	–8.7
–100 to –300	–10.0	–9.9	–9.6
Below –300	–10.3	–10.1	–9.9

Table 5-12 summarises the results of this deterministic simulation in terms of the travel time, canister flux and F-ratio averaged over all the starting positions. Approximately 9.2% of the stream tubes fail to reach the upper surface. Note that the median travel time is 1790 years and median canister flux is 3.40×10^{-5} m/year, both very similar to those of the Base Case. In comparison to the Base Case, the variance of $\log_{10}$ canister flux is much lower at 0.007 because the hydraulic conductivity field has no spatial variability. In contrast to the canister flux, the variance of $\log_{10}$travel time for this variant is 0.096, relatively unchanged from the Base Case. This suggests that the variability of travel times is due to the differences in starting position relative to the exit location, and not due to heterogeneity of the host rocks. This low variability is also seen in the smooth, regular patterns of the stream tubes and exit locations (Figures 5.4-1 and 5.4-2). The stream tubes and exit locations also clearly indicate the location and influence of the fracture zones, suggesting that the deterministic zones have an important effect on the performance assessment. The influence of the fracture zones on the exit locations suggests a model refinement of including the fracture zones as stochastic features, rather than as deterministic features.

Table 5-12. Results are shown for Ceberg Variant 4 (deterministic). In this variant, eleven travel times exceeded 100,000 years. Results are shown for 119 starting positions, a flow porosity of $\varepsilon_f = 1 \times 10^{-4}$ and flow-wetted surface $a_r = 0.1$ m^2/(m^3 rock). Statistics in bold are discussed in the text. Approximately 9.2% of the stream tubes fail to reach the upper surface.

	All values			**Travel Times > 100,000 years deleted**		
	Log$_{10}$ t_w	**Log$_{10}$ q_c**	**Log$_{10}$ F-ratio**	**Log$_{10}$ t_w**	**Log$_{10}$ q_c**	**Log$_{10}$ F-ratio**
Mean	3.399	–4.455	6.399	3.236	–4.453	6.236
Median	3.294	**–4.468**	6.294	**3.253**	–4.467	**6.253**
Variance	0.351	**0.007**	0.351	**0.096**	0.008	**0.096**
5th percentile	2.748	–4.594	5.748	2.739	–4.595	5.739
25th percentile	3.009	–4.498	6.009	2.994	–4.491	5.994
75th percentile	3.523	–4.424	6.523	3.454	–4.423	6.454
95th percentile	5.000	–4.279	8.000	3.801	–4.276	6.801

Table 5-13 summarises the boundary flows of this variant, the Base Case and the regional model. Ideally, all three sets of boundary flows should match, since they are designed to be alternative representations of the same system at different levels of detail. The boundary flows of the Base Case and Deterministic Variant agree with respect to the pattern of inflows and outflows, but the deterministic model under-predicts the Base Case flows by a factor of 1/2. In contrast, the regional model is different by an order of magnitude, and predicts outflow from the bottom surface of the domain.

Table 5-14 presents a mass balance for a reduced domain (i.e., the upper surface of the mass balance control volume is lowered to –100 masl for both models), which shows a dramatic improvement. The regional and site-scale boundary flows are within a factor of two. This suggests that most of the discrepancy between the regional and site-scale models occurs near the upper surface of the domain. This is attributed to mismatches in zone geometries and the use of calibrated conductivities in the upper surface of the Boghammar et al. (1997) regional model. The regional mass balance residual of 6% is attributed to the approximate method used for calculating mass balance within finite elements of the regional model (Appendix B.2).

Possible causes for the mass balance residual between the regional and site models have been discussed in Sections 4.2. and 5.3. The relative agreement of travel times and canister fluxes between this variant and the Base Case suggests that the upscaling of means and variances is qualitatively correct. The low level of agreement of the boundary flows between the regional and site-scale models suggests that the nested modelling could be improved, particularly in the upper levels of the domain.

Table 5-13. Boundary flow consistency of Ceberg Variant 4 (deterministic) and Base Case, regional model versus site-scale models.

	Net Flow Through Site Model Surfaces ($m^3/s \times 10^{-3}$)		
Model Surface	**Regional (GRST)**	**Site-scale: Base Case**	**Site-scale: Deterministic**
West	2.59 (in)	0.289 (in)	0.100 (in)
East	2.25 (in)	0.150 (in)	0.0649 (in)
South	16.7 (out)	0.920 (out)	0.411 (out)
North	3.84 (out)	0.0995 (out)	0.0927 (out)
Bottom	0.00279 (out)	0.0221 (in)	0.0196 (in)
Top	17.7 (in)	0.557 (in)	0.320 (in)
Total Inflow	22.54	1.02	0.505
Total Outflow	20.54	1.02	0.504
Mass balance (In – Out)	2.00	–0.0014	0.0008

Table 5-14. Boundary flow consistency for a reduced domain at z = –100 m for Ceberg Variant 4 (deterministic), regional model versus site-scale models.

	Net Flow Through Site Model Surfaces ($m^3/s \times 10^{-3}$)		
Model Surface	**Regional (GRST)**	**Base Case (5 realisations)**	**Deterministic Case (5 realisations)**
Total Inflow	0.0413	0.0262	0.0230
Total Outflow	0.0390	0.0262	0.0230
Mass balance (In – Out)	0.0023	0.000	0.0000

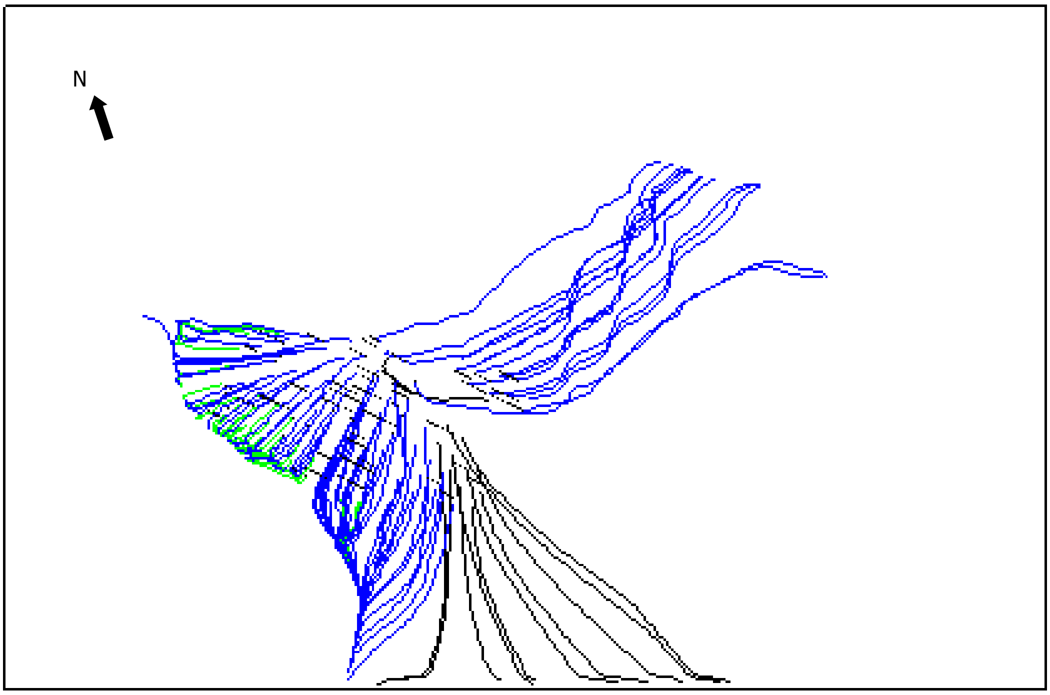

a) Plan view

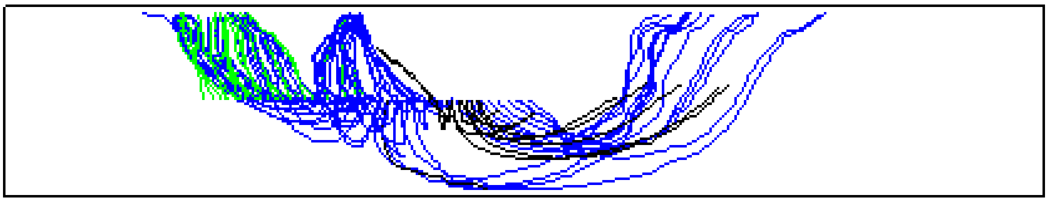

b) Elevation view, from South

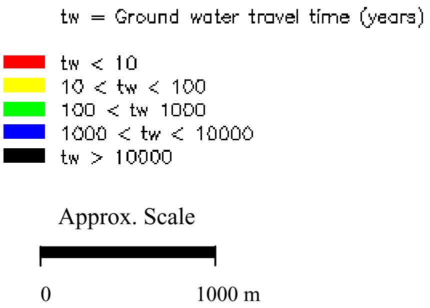

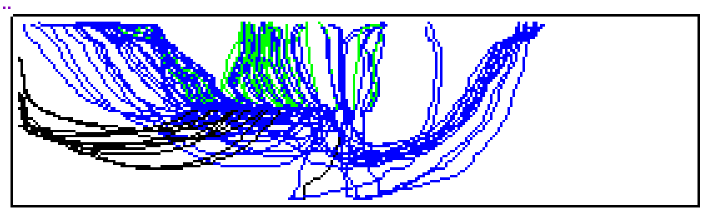

c) Elevation view, from East

Figure 5.4-1. *Stream tubes in realisation number 1 of Ceberg Variant 4 (deterministic). The y-positive axis of a) is rotated 15 cw from North. Results are shown for 119 starting positions and a flow porosity of* $\varepsilon_f = 1\times10^{-4}$.

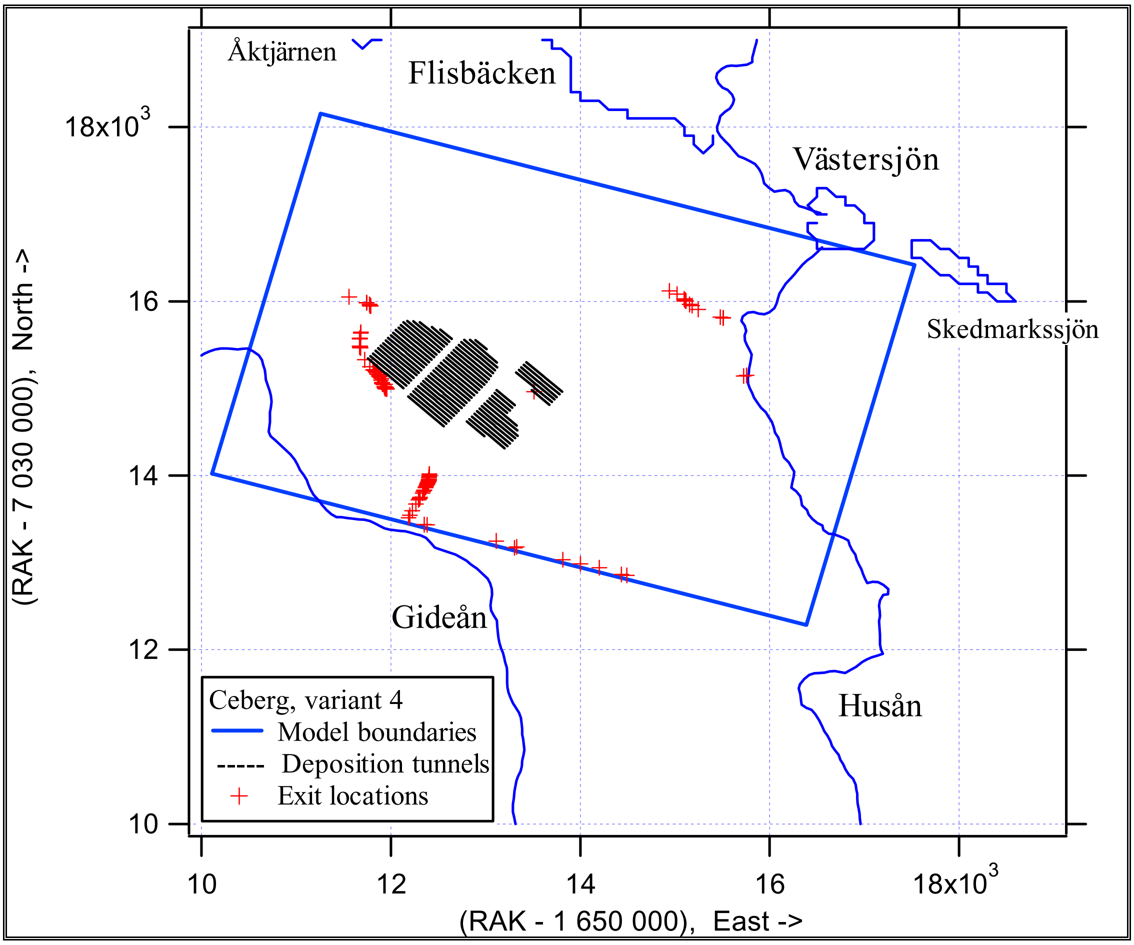

Figure 5.4-2. *Exit locations for Ceberg Variant 4 (deterministic). Results are shown for 119 starting positions (plan view, scale in metres).*

6 Discussion and Summary

The SKB SR 97 study is a comprehensive performance assessment illustrating the results for three hypothetical repositories in Sweden. This study addresses the hydrogeologic modelling of Ceberg, one of three sites, via the application of HYDRASTAR, a stochastic continuum groundwater flow-modelling program. The application is relatively straightforward, with the majority of the model parameters explicitly specified in Walker et al. (1997b). This section of the report summarises the simulations and discusses the results of the study in terms of statistics for travel time, F-ratio and canister flux. It also summarises the findings of the study with regard to model parameter uncertainty, as evaluated by the variant cases.

The study results are broadly summarised by the statistics of the common logarithm transforms of the travel times, canister fluxes and F-ratios to facilitate summary (Table 6.1). The results for the Base Case and the variants are directly compared in plots of their floating histograms in Figures 6.2-1 and 6.2-2 (note that Variant 4 is excluded because its low performance measure variances; see Appendix A.1 for the computation of the floating histograms).

6.1 Input Data

Input data for the model are unmodified from that given in Walker et al. (1997b) except for the empirical rescaling of hydraulic conductivities as suggested by Walker et al. (1997b). The SKB geostatistical analysis code INFERENS is used to infer a regularised variogram model, based on the 25 m interpreted hydraulic conductivities taken from SICADA.

The boundary conditions for this model are constant head boundaries, taken from a deterministic regional scale model of Boghammar et al. (1997). The overall groundwater flow pattern of the regional model is typical of topographically-driven systems, with recharge in the uplands discharging to valleys. The regional heads are transferred to the site-scale model via constant head boundaries, generally preserving the regional flow pattern in the site-scale model. The mass balance between the nested models is presented via a comparison of net volumetric flow of water over the site-scale model boundaries. Adjustment of the scaling of hydraulic conductivity to fine-tune the boundary flows is not pursued.

6.2 Base Case

The Base Case uses 100 realisations of 119 stream tube starting positions to evaluate the canister fluxes, travel times, and F-ratios for the proposed repository. As discussed in Section 4.0, the median travel times and median canister fluxes of the Base Case appear to be stable with respect to the number of simulations. The boundary flows of the regional model and the site-scale model appeared to be consistent with respect to orientation, but the site-scale model underpredicts the boundary flows of the regional model by a factor of 20. Detailed analysis of these flows indicates that the inconsistency occurs near the upper model surface and that the nested models and the upscaling of hydraulic conductivity generally preserve mass balance over the majority of the domain. A comparison of the Base and Deterministic (Variant 4) Cases indicates that the upscaling is approximately self-consistent with respect to median travel time, median canister flux and boundary flows.

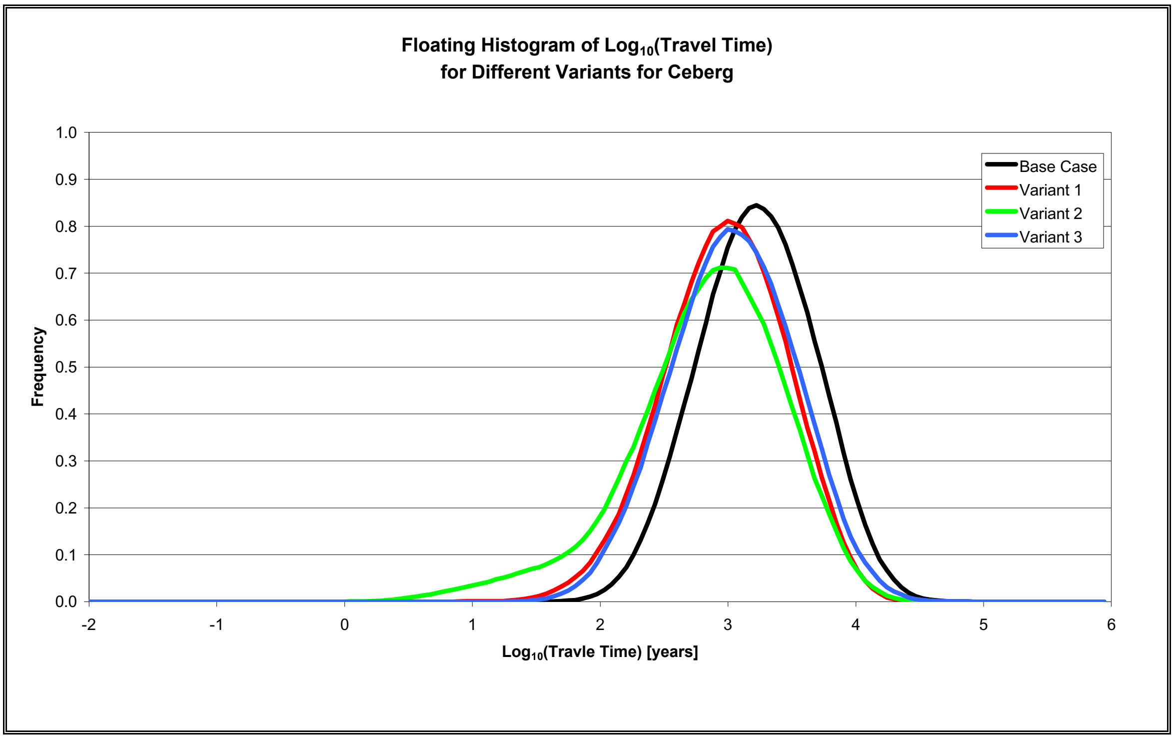

Figure 6.2-1. *Summary of Ceberg modelling results: floating histogram of* $\log_{10}$ *travel time normalised to the number of travel times less than 100,000 years. Results are shown for 119 starting positions and a flow porosity of* $\varepsilon_f = 1\times10^{-4}$.

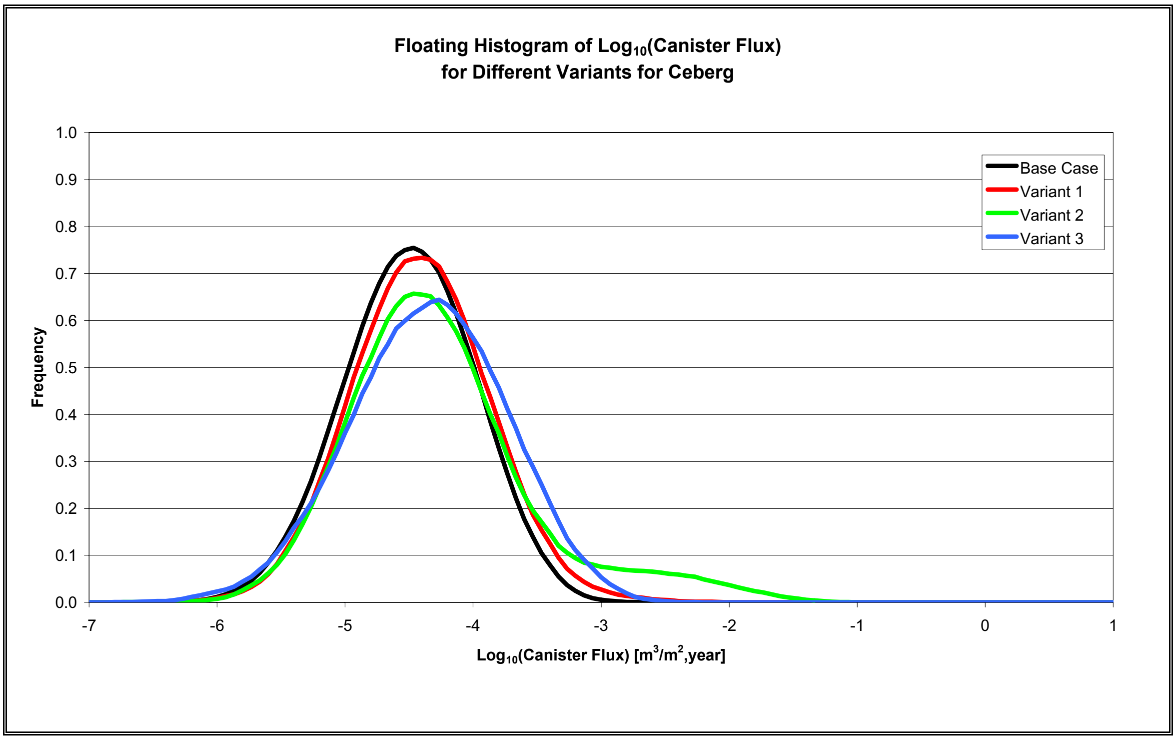

Figure 6.2-2. *Summary of Ceberg modelling results: floating histogram of log_{10} canister flux normalised to the total number of stream tubes.*

The results for 100 realisations of 119 starting positions with a flow porosity of $\varepsilon_f = 1\times10^{-4}$ and a flow-wetted surface area of $a_r = 0.1$ $m^2/(m^3$ rock) suggest the following results for the Base Case:

- The median travel time is 1720 years with an interquartile range from 953 to 2965 years.
- The median canister flux is 3.27×10^{-5} m/year with an interquartile range from 1.66×10^{-5} to 6.25×10^{-5} m/year.
- The median F-ratio is 1.72×10^{6} year/m with an interquartile range from 9.53×10^{5} to 2.97×10^{6} year/m.

The current version of HYDRASTAR is limited to homogeneous flow porosity over the entire domain. Consequently, the F-ratio is a simple multiple of the travel time, and the $\log_{10}$ canister flux has a slight, inverse correlation with travel time. The stream tubes and exit locations of the realisations are compatible with the overall pattern of flow at the site. Approximately 10% of the stream tubes fail to reach the upper surface of the model domain, with most of these stream tubes exiting the southern model boundary. Approximately 1% of the total number of stream tubes exit the bottom surface of the model, directly beneath the site.

Three realisations are examined to illustrate the variability within each realisation, and are compared to illustrate the variability between realisations of the Monte Carlo set. The variability within a realisation due to spatial variability is rather high, but the exit locations are relatively stable between realisations. The variability between realisations for median travel time and median canister flux is relatively low.

Three individual starting positions are examined over all 100 realisations to illustrate variability due to the differences in location. These positions demonstrate that some areas have shorter travel times (e.g., the southwestern side of the repository). This is attributed to the starting position relative to the discharge area and flow pattern, rather than to spatial variability of the host rock hydraulic conductivity.

6.3 Variant Cases

6.3.1 Increased Conductivity Contrast

This variant addresses the possibility that the deterministic fracture zones can be quite conductive, even though the median hydraulic conductivity of the fracture zones inferred from the hydraulic tests is quite low. As suggested in Walker et al. (1997b), the hydraulic conductivity of the rock mass remains unchanged, but the hydraulic conductivity of the fracture zones is increased by a factor of 100. The regional modelling study of Boghammar et al. (1997) provided a set of boundary conditions appropriate for increased fracture zone hydraulic conductivities, different from the regional model used for the Base Case. Most of the boundary flow inconsistencies between the regional and site-scale models occur in the upper model surfaces.

The overall effect of increasing the conductivity of the fractures is to reduce the median travel time to 998 years, and slightly increase the variance of $\log_{10}$ travel time to 0.148. These results reflect travel paths being diverted and accelerated as a result of increasing the conductivity of the fracture zones. Stream tubes and exit locations are organised around fracture zones, and exit locations near the stream Husån are shifted 1 km to the west. Canister flux is essentially unchanged from the Base Case, since the fracture zones do not intersect the starting positions representing the hypothetical canisters. There are statistically significant differences between the results of this variant and those of the Base Case. The inverse correlation of travel times and canister fluxes is stronger in this variant than in the Base Case.

6.3.2 Alternative Conductive Features

This variant case evaluates the possibility that the intrusive dykes and one additional regional lineament are conductive features. Similar to the variant discussed in Section 4.2, these fractures are assumed to have a hydraulic conductivity 100 times that of the Base Case. The additional regional lineament requires a new set of boundary conditions, which are provided by a new simulation based on the regional model of Boghammar et al. (1997) (Appendix B). Most of the boundary flow inconsistencies between the regional and site-scale models occur in the upper model surface.

In comparison to the Base Case, the median travel time is reduced to 800 years, and the variance of $\log_{10}$ travel time is increased to 0.307. The travel time distribution is markedly skewed and the median canister flux is slightly increased to 4.3×10^{-5}, reflecting the fracture zones intersecting the repository zone. The inverse correlation of travel times and canister fluxes is stronger in this variant than in the Base Case. These results are similar to those of Variant 1, where many of the stream tubes are intercepted by conductive features, decreasing the median travel time while increasing the variance of $\log_{10}$ travel time. The effect is stronger in this variant because one of the conductive features runs directly through the repository. Unlike Variant 1, the median canister flux is increased as a consequence of one of the alternative features passing through the repository zone, intercepting seven starting positions. There are statistically significant differences between the results of this variant and those of the Base Case. Similar to Variant 1, the stream tubes are organised along fracture zones, and exit locations near the stream Husån are shifted 1 km to the west.

6.3.3 Increased Conductivity Variance

The simulations in Variant 3 are performed to evaluate the uncertainties associated with the inference of the variance of hydraulic conductivity. For this variant case, the variance of $\log_{10}$ hydraulic conductivity is increased from 1.12 to 2.0. The mean conductivities for the rock mass domain and the fracture zone domain are identical to the Base Case. The increased variance does not appear to have reduced the stability of the Monte Carlo simulations. Excluding the upper model surface, the boundary flows for the regional and site-scale models are in good agreement.

Relative to the Base Case, the variances of $\log_{10}$ travel time and $\log_{10}$ canister flux increase, reflecting the increased variance. The median travel time decreases to 1130 years, and the median canister flux increases to 4.59×10^{-5} m/year. The increased boundary and canister fluxes, and the decreased travel time conceptually agree with the predictions of stochastic continuum theory regarding the effective conductivity of the domain. There are statistically significant differences between the results of this variant and those of the Base Case. Flow patterns for this variant appear little different from those of the Base Case.

6.3.4 Deterministic Simulation

This variant is a simplified simulation of the site using a deterministic representation of the hydraulic conductivity field (i.e., the field has no random component and thus needs only one ‘realisation’). This study uses the empirical upscaling rule to estimate the effective conductivity of the deterministic field. Note that for this variant, there is no block-scale variability (zero variance).

Relative to the Base Case, the variance of $\log_{10}$ travel time is reduced only slightly to 0.096, suggesting that the travel time variability in the Base Case is due to the difference in starting positions relative to the flow pattern. The variance of $\log_{10}$ canister flux is much lower at 0.007, as is expected for a deterministic hydraulic conductivity field. Similar to the Base Case, the median travel time is 1790 years and the median canister flux is 3.40×10^{-5} m/year, suggesting that the upscaling of hydraulic conductivity is approximately self-consistent.

6.3.5 Comparison

Table 6-1 presents a summary of the medians and variances of the performance measures for the Base Case (in bold) and for Variants 1 through 4. Variant 2, Alternative Conductive Features, yields the shortest median travel time. Variant 4, Deterministic Simulation, yields the longest median travel time but is very similar to the Base Case. Variant 3, Increased Variance, yields the maximum median canister flux, and the Base Case yields the minimum median canister flux.

Note that the Base Case variability nearly encompasses the full range of variability exhibited by the variant cases. For example, the Base Case travel time has an inter-quartile range from 953 to 2965 years, while the range of median travel times for the variants is from 800 years (Variant 2) to 1790 years (Variant 4). Thus the variability of the Base Case due to parameter variability is approximately the same as the variability of the cases studied to address uncertainty. Within the limitations of the variant cases studied, this suggests that the Base Case has adequately characterised the Ceberg hypothetical performance. Similarly, although there are statistically significant differences between the distributions of the performance measures among all the cases, the differences between the cases are believed to be minor in the context of performance assessment.

Table 6-1. Summary of Ceberg site-scale modelling study. Results are shown for 119 starting positions, a flow porosity of $\varepsilon_f = 1\times10^{-4}$ and flow-wetted surface $a_r = 0.1$ m^2/(m^3 rock). Statistics in bold are discussed in the text.

Performance Measure	Statistic	Base Case	Variant 1 (FZ Contrast)	Variant 2 (Alt. CD)	Variant 3 (Increased Var.)	Variant 4 (Deterministic)
Log$_{10}$ Travel time (years, for travel times less than 100,000 years)	Median	**3.236**	2.999	2.903	3.052	3.253
	Variance	**0.123**	0.148	0.307	0.156	0.096
Log$_{10}$ Canister Flux (m/year, for all starting positions)	Median	**–4.485**	–4.423	–4.367	–4.338	–4.468
	Variance	**0.182**	0.212	0.482	0.295	0.007
Log$_{10}$ F-ratio (year/m, for travel times less than 100,000 years)	Median	**6.236**	5.999	5.903	6.052	6.253
	Variance	**0.123**	0.148	0.307	0.156	0.096

6.4 Possible Model Refinements

This modelling study evaluates the groundwater flow system at the Ceberg site, using a model that incorporates the processes believed to dominate the site groundwater system. This includes Base Case simulations of the expected site conditions, and several Variant Cases that evaluate uncertainties. Although the study is considered adequate for performance assessment, there are additional variant cases that may be of interest.

It is possible to examine several additional variants and model refinements within the current features of HYDRASTAR. For example, extending the model domain downward and southward might capture and quantify the stream tubes that fail to exit the upper surface of the model. The variability of hydraulic conductivity with depth is uncertain, and could be evaluated with a variant case for an alternative representation of the depth trend of hydraulic conductivity. It should be noted, however, that the uncertainties evaluated by these possible variants are believed to have only a minor effect on the performance assessment.

Other model refinements are possible but are outside of the current features of HYDRASTAR. These include experimentation with alternative upscaling methods and the use of alternative methods of representing the hydraulic conductivities (e.g., nonparametric geostatistical simulation, or discrete feature networks upscaled to numerical block conductivities, stochastic fracture zones, etc.). Ultimately, because of the dominating effect of the boundary conditions, such refinements may not have a profound impact on the performance measures. The relative importance of the boundary conditions, however, suggests a variant case to investigate the effects of using constant flux (Neuman) or third-type boundaries instead of the present constant head (Dirichlet) boundaries. Lastly, Variants 1 and 2 suggest refining the regional model flow balance to reduce the apparent residual of the regional model and make the flow balance a more powerful modelling tool.

6.5 Summary of Findings

The findings of this study can be summarised as follows. With regard to the usage of data and consistency with the regional model, the parameters are consistent with field observations, and are unmodified except for the rescaling of hydraulic conductivity inherent to stochastic continuum modelling. The majority of the boundary flow inconsistencies between the regional and site-scale models appear to occur in the near-surface regions of the models.

With regard to the variability seen within realisations, there is great spatial variability seen in the travel times and canister fluxes within single realisations. This variability appears to be the result of the position of the hypothetical canisters relative to the discharge areas, rather than to the spatial variability of the host rocks.

The results for 100 realisations of 119 starting positions, a flow porosity of $\varepsilon_f = 1\times10^{-4}$ and a flow-wetted surface area of $a_r = 0.1$ m^2/(m^3 rock) suggest the following results for the Base Case:

- The median travel time is 1720 years with an interquartile range from 953 to 2965 years.
- The median canister flux is 3.27×10^{-5} m/year with an interquartile range from 1.66×10^{-5} to 6.25×10^{-5} m/year.
- The median F-ratio is 1.72×10^{6} year/m with an interquartile range from 9.53×10^{5} to 2.97×10^{6} year/m.
- The common logarithm of canister flux appears to be inversely correlated to the common logarithm of travel time.
- The stream tubes and exit locations are compatible with the flow pattern at the site.

The uncertainties of this study are addressed by a series of variant cases that evaluate the sensitivity of the results to changes in assumptions regarding the structural model and the hydraulic conductivities. The results are most sensitive to the occurrence of additional highly conductive features such as fracture zones or intrusive dykes, particularly if such features directly intersect with the waste canisters. However, it is reasonable to assume that such features would be avoided in the placement of waste canisters. Although the approach to upscaling appears to be approximately self-consistent, the nested modelling approach and the regional model mass balance could be re-examined.

Acknowledgements

The authors of this report would like to acknowledge the support and guidance of Anders Ström and Jan-Olof Selroos of the Swedish Nuclear Fuel and Waste Management Company (SKB). This study has benefited enormously from the review comments of Johan Andersson and Sven Follin of Golder Grundteknik, and Ingvar Rhén, VBB VIAK. Raymond Munier of Scandia Consult and Lee Hartley of AEA Technology have contributed data, ideas and useful comments throughout this study. Lydia Biggs (DE&S) contributed a number of illustrations and formatting suggestions to this report. The final text has benefited enormously from the careful editing of Marcie Summerlin (DE&S).

At the end of a long study, it is tempting to list all of modelling team members as coauthors of the final report, but this would be a practical impossibility for this report. The efforts of the following contributors are appreciated and are hereby acknowledged:

- Maria Lindgren and Hans Widén (Kemakta) implemented the structural model and assisted in setting up the HYDRASTAR model for this study.
- Niko Marsic (Kemakta) postprocessed the model output to provide the statistical summaries of results, and Lars Lovius (Hellström and Lovius Data) provided general support for the HYDRASTAR simulations and postprocessing of results.
- Björn Bergman (DE&S) performed the scoping calculations for travel time, and along with Cecilia Andersson (DE&S) assisted in preparing the preliminary sections of the report.
- Gregory Ruskauff (DE&S) assisted in the geostatistical analysis and helped review and summarise the study.
- Lee Hartley (AEA Technology) supported the NAMMU regional model simulations and assisted in the preparation of Appendix B.

This study was funded by The Swedish Nuclear Fuel and Waste Management Company (SKB).

References

Abramovich B and Indelman P, 1995. Effective permeability of log-normal isotropic random media. J. Phys. A: Math. Gen., 28, p 693–700.

Ahlbom K, Albino B, Carlsson L, Nilsson G, Olsson O, Stenberg L and Timje H, 1983. Evaluation of the geological, geophysical and hydrogeological conditions at Gideå. Swedish Nuclear Fuel and Waste Management Co., SKBF/KBS Technical Report TR 83-53, Stockholm, Sweden.

Ahlbom K, Andersson J-E, Nordqvist R, Ljunggren C, Tirén S and Voss C, 1991. Gideå study site. Scope of activities and main results. Swedish Nuclear Fuel and Waste Management Co., SKB Technical Report TR 91-51, Stockholm, Sweden.

Andersson J, 1999. SR 97 – Data and data uncertainties: Compilation of data and evaluation of data uncertainties for radionuclide transport calculations, Swedish Nuclear Fuel and Waste Management Co., SKB Technical Report TR-99-09, Stockholm, Sweden.

Askling P, 1997. Gideå lineament map. An interpretation based on elevation data models. Swedish Nuclear Fuel and Waste Management Co., SKB Progress Report PR U-97-06, Stockholm, Sweden.

Björck S and Svensson N-O, 1992. Climatic changes and uplift patterns – past, present and future. Swedish Nuclear Fuel and Waste Management Co., SKB Technical Report TR 92-38, Stockholm, Sweden.

Boghammar A and Marsic N, 1997. Using Statistica when evaluating results from HYDRASTAR 1.5+. Swedish Nuclear Fuel and Waste Management Co., SKB Progress Report PR U-97-18, Stockholm, Sweden.

Boghammar A, Grundfelt B and Hartley L, 1997. Investigation of the large scale regional hydrogeological situation at Ceberg. Swedish Nuclear Fuel and Waste Management Co., SKB Technical Report TR 97-21, Stockholm, Sweden.

Carlsson L, Winberg A and Grundfelt B, 1983. Model calculations of the groundwater flow at Finnsjön, Fjällveden, Gideå and Kamlunge. SKBS KBS Technical Report TR 83-45, Stockholm, Sweden.

Cliffe K A, Jackson C P and Morris S T, 1995. Assessment Model Validity Document; NAMMU: A program for calculating groundwater flow and transport through porous media. Swedish Nuclear Fuel and Waste Management Co., SKB Working Report AR 95-11, Stockholm, Sweden.

Dagan G, 1986. Statistical theory of groundwater flow and transport: pore to laboratory, laboratory to formation, and formation to regional scale. Water Resources Research, 22(9), p 1205–1345.

Dagan G, 1993. High-order correction of effective permeability of heterogeneous isotropic formations of lognormal conductivity distributions. Transport in Porous Media, 12, p 279–290.

de Marsily G, Lavedan C, Boucher M and Fasanino G, 1984. Interpretation of Interference Tests in a Well Field Using Geostatistical Techniques to Fit the Permeability Distribution in a Reservoir Model, in Geostatistics for Natural Resources Characterisation. Second NATO Advanced Study Institute, GEOSTAT 1983, Tahoe City, California. Edited by G. Verly, M. David, A.G. Journel, and A. Marachal, p 831–849, D. Reidel, Hingham, MA, USA.

Ericsson L O, and Ronge B, 1986. Correlations between tectonic lineaments and permeability values of crystalline bedrock in the Gideå area. Swedish Nuclear Fuel and Waste Management Co., SKB Technical Report TR 86-19, Stockholm, Sweden.

Geier J, 1993. Verification of the geostatistical inference code INFERENS, Version 1.1, and demonstration using data from Finnsjön. Swedish Nuclear Fuel and Waste Management Co., SKB Technical Report TR 93-09, Stockholm, Sweden.

Gutjahr A L, Gelhar L W, Baker A A and MacMillan J R, 1978. Stochastic analysis of spatial variability in subsurface flows. 2. Evaluation and application. Water Resources Research, 14(5), p 953–959.

Gylling B, Lindgren M and Widén H, 1999a. Preparatory hydrogeological calculations for site scale models of Aberg, Beberg, and Ceberg. Swedish Nuclear Fuel and Waste Management Co., SKB Report R-99-06, Stockholm, Sweden.

Gylling B, Walker D and Hartley L, 1999b. Site-scale groundwater flow modelling of Beberg. Swedish Nuclear Fuel and Waste Management Co., SKB Technical Report in preparation, Stockholm, Sweden.

Hammersley J M and Handscomb D C, 1975. Monte Carlo Methods. Methuen, London.

Hermanson J, Hansen L M and Follin S, 1997. Update of the geological models of the Gideå study site. Swedish Nuclear Fuel and Waste Management Co., SKB Report R-97-05, Stockholm, Sweden.

Hodgkinson D P and Barker J, 1985. Specification of a Test Problem for HYDROCOIN Level 1 Case1: Transient Flow from a Borehole in a Fractured Permeable Medium. Report AERE R-11574, UK Atomic Energy Authority, Harwell Laboratories, UK.

Hultman S, 1997. Visualisation of HYDRASTAR Simulation Data in the AVS 5 System. Swedish Nuclear Fuel and Waste Management Co., SKB Progress Report PR U-97-01, Stockholm, Sweden.

Journel A G and Huijbregts Ch J, 1978. Mining Geostatistics. Academic Press.

Laaksoharju J, Skårman C and Gurban I, 1998. SR 97: Summary of Hydrogeochemical conditions at Aberg, Beberg and Ceberg. Swedish Nuclear Fuel and Waste Management Co., SKB Technical Report TR 98-03, Stockholm, Sweden.

Larsen R J and Marx M L, 1986. An Introduction to Mathematical Statistics and Its Applications. Prentice-Hall, London.

Leake S A, Lawson P W, Lilly M R and Claar D V, 1998. Assignment of boundary conditions in embedded groundwater flow models. Ground Water 36(4), p 621–625.

Lovius L, 1998. Calculation of flux through boundaries in HYDRASTAR. Swedish Nuclear Fuel and Waste Management Co., SKB Progress Report PR U-98-08, Stockholm, Sweden.

Lovius L and Eriksson L, 1993. Verification of HYDRASTAR version 1.4. Swedish Nuclear Fuel and Waste Management Co., SKB Working Report AR 93-46, Stockholm, Sweden.

Lovius L and Eriksson L, 1994. Development of a transient version of HYDRASTAR. Swedish Nuclear Fuel and Waste Management Co., SKB Working Report AR 94-12, Stockholm, Sweden.

Lundqvist T, Gee D, Karis L, Kumpulainen R and Kresten P, 1990. Beskrivning till berggrundskartan över Västernorrlands Län (in Swedish with an English summary). SGU ser. BA 31. Geological Survey of Sweden, Uppsala.

Marsic N, 1999. Using STATISTICA and MATLAB when evaluating results from HYDRASTAR 1.5+. Swedish Nuclear Fuel and Waste Management Co., SKB Progress Report TS-99-04, Stockholm, Sweden.

Morris S T and Cliffe K A, 1994. Verification of HYDRASTAR: Analysis of hydraulic conductivity fields and dispersion. Swedish Nuclear Fuel and Waste Management Co., SKB Technical Report TR 94-21, Stockholm, Sweden.

Munier R, Sandstedt H and Niland L, 1997. Förslag till principiella utformningar av förvar enligt KBS-3 för Aberg, Beberg and Ceberg. Swedish Nuclear Fuel and Waste Management Co., SKB Report R 97-09, Stockholm, Sweden.

Neuman S, 1988. A proposed conceptual framework and methodology for investigating flow and transport in Swedish crystalline rocks. Swedish Nuclear Fuel and Waste Management Co., SKB Working Report AR 88-37, Stockholm, Sweden.

Neuman S and Jacobson E, 1984. Analysis of nonintrisic spatial variability by residual kriging with application to regional groundwater levels. Mathematical Geology, 16(5), p 499–521.

Norman S, 1991. Verification of HYDRASTAR – A code for stochastic continuum simulation of groundwater flow. Swedish Nuclear Fuel and Waste Management Co., SKB Technical Report TR 91-27, Stockholm, Sweden.

Norman S, 1992a. Statistical inference and comparison of stochastic models for the hydraulic conductivity at the Finnsjön-site. Swedish Nuclear Fuel and Waste Management Co., SKB Technical Report TR 92-08, Stockholm, Sweden.

Norman S, 1992b. HYDRASTAR – A code for stochastic simulation of groundwater flow. Swedish Nuclear Fuel and Waste Management Co., SKB Technical Report TR 92-12, Stockholm, Sweden.

OECD, 1983. The International HYDROCOIN Project: Groundwater hydrology modelling strategies for performance assessment of nuclear waste disposal. Level: Code verification.

Renard Ph and de Marsily G, 1997. Calculating equivalent permeability: a review. Advances in Water Resources, 20 (5,6), p 253–278.

Rhén I, Gustafson G, Stanfors R and Wikberg P, 1997. Äspö Hard Rock Laboratory – Geoscientific Evaluation 1997/5. Models based on site characterisation 1986–1995. Swedish Nuclear Fuel and Waste Management Co., SKB Technical Report TR 97-06, Stockholm, Sweden.

Rubin Y and Gómez-Hernández J J, 1990. A stochastic approach to the problem of upscaling of conductivity in disordered media: Theory and unconditional numerical simulations. Water Resources Research, 26(4), p 691–701.

Saksa P and Nummela J, 1998. Geological-structural models used in SR 97: Uncertainty analysis. Swedish Nuclear Fuel and Waste Management Co., SKB Technical Report TR 98-12, Stockholm, Sweden.

SKB, 1992. SKB 91: Final disposal of spent nuclear fuel. Importance of bedrock for safety. Swedish Nuclear Fuel and Waste Management Co., SKB Technical Report TR 92-20, Stockholm, Sweden.

SKB, 1996a. SR-95: Template for safety reports with descriptive example. Swedish Nuclear Fuel and Waste Management Co., SKB Technical Report TR 96-05, Stockholm, Sweden.

SKB, 1996b. User's Guide to HYDRASTAR 1.5. Swedish Nuclear Fuel and Waste Management Co., SKB Progress Report PR-U-96-15, Stockholm, Sweden.

Timje H, 1983. Hydrogeological investigations at study site Gideå. Swedish Nuclear Fuel and Waste Management Co., SKBF/KBS Working Report AR 83-26 (in Swedish), Stockholm, Sweden.

Walker D and Bergman B, 1998. Verification of HYDRASTAR v.1.7: Transient simulation and pilot point calibration. Swedish Nuclear Fuel and Waste Management Co., SKB Progress Report in preparation, Stockholm Sweden.

Walker D and Gylling B, 1998. Site-scale groundwater flow modelling of Aberg. Swedish Nuclear Fuel and Waste Management Co., SKB Technical Report TR 98-23, Stockholm, Sweden.

Walker D, Lovius L and Eriksson L, 1997a. Verification of HYDRASTAR 1.7: Nugget effect in geostatistical simulations. Swedish Nuclear Fuel and Waste Management Co., SKB Progress Report, PR U-97-22, Stockholm, Sweden.

Walker D, Rhén I and Gurban I, 1997b. Summary of Hydrogeologic Conditions at Aberg, Beberg and Ceberg. Swedish Nuclear Fuel and Waste Management Co., SKB Technical Report 97-23, Stockholm, Sweden.

Ward D, Buss D, Mercer J and Hughes S, 1987. Evaluation of a groundwater corrective action at the Chem-Dyne hazardous waste site using a telescopic mesh refinement modelling approach. Water Resources Research, 23(4), p 603–617.

Appendix A. Definition of Statistical Measures

A.1 Floating Histograms

This study generally uses binned histograms to display the frequency distributions of the performance measures. The bin width of such histograms is determined by the default algorithms of Statistica. Although the bin width is somewhat subjective, binned histograms do provide a relatively unprocessed image of the data. However, binned histograms are not well suited to graphical comparisons (e.g. overlaying multiple binned histograms is confusing to the eye).

An alternative method of constructing a frequency distribution histogram is to use a floating histogram. Floating histograms are single curved line representations of the frequency of the data. Although floating histograms are smoothed representations of the data, they are more legible when superimposed for the comparison of multiple histograms. Depending on the format and type of data being processed, several software packages (Appendix F) are used to calculate the floating histograms using a moving window as a filter passing over the ordered sequence of the data. For each datum value centred in the window, the smoothed frequency is calculated as the fraction of the data falling within the window. The width of the window is somewhat arbitrarily set to ± ½ an order of magnitude around the datum value in the centre of the window, and the frequency of each window is normalised by dividing by the total number of data. Generally, MATLAB is used to calculate the moving window statistics, and the histograms displayed in Excel. The exception to this is Figure 4.3-11, which is calculated and plotted using Statistica. The floating histograms of Variant 4, the Deterministic Case, are omitted, since the low performance measure variances result in virtually the entire distribution falling within the smoothing window.

A.2 Statistical Significance of the Comparison of Distributions

Section 5 makes a number of comparisons of variant cases versus the Base Case or versus other variants, concluding that ‘there are statistically significant differences between the distributions’. This statement of significance is quantitatively supported by a statistical comparison of the distributions, testing the null hypothesis:

H_0: the distributions are the same

The significance of this test, or p-value, is the probability of rejecting H_0 when it is in fact true (a so-called Type I error). Thus, a small p-value indicates that we can safely reject the hypothesis that the distributions are the same (Larsen and Marx, 1986). Because the distributions to be compared in this study are skewed, they are not suited to test statistics that assume normally (Gaussian) distributed data. This study therefore uses nonparametric (distribution-free) test statistics to compute the p-value of the above test. The Kolmogorov-Smirnov test (K-S) is a nonparametric test used to compare distributional shapes (i.e., skewness, variability, and location), as documented in the Statistica manual. The p-value of a K-S test of H_0 is computed for the various combinations of the Base Case and variant cases (Table A-1).

Note: When computing the p-value for the comparisons of $\log_{10}$ travel time distributions, times greater than the default maximum travel time of 100,000 years are deleted from the distributions prior to the comparison. The resulting K-S p-value therefore ignores the stream tubes failing to exit the upper surface of the model.

Table A-1 Test for Similarity of Travel Time Distributions (Kolmogorov-Smirnov 2-sample).

Case	**Base**	**Variant 1**	**Variant 2**	**Variant 3**
Base		reject(p<0.001)	reject(p<0.001)	reject(p<0.001)
Variant 1	reject(p<0.001)		reject(p<0.001)	reject(p<0.001)
Variant 2	reject(p<0.001)	reject(p<0.001)		reject(p<0.001)
Variant 3	reject(p<0.001)	reject(p<0.001)	reject(p<0.001)	

Canister Flux

Case	**Base**	**Variant 1**	**Variant 2**	**Variant 3**
Base		reject(p<0.001)	reject(p<0.001)	reject(p<0.001)
Variant 1	reject(p<0.001)		reject(p<0.001)	reject(p<0.001)
Variant 2	reject(p<0.001)	reject(p<0.001)		reject(p<0.001)
Variant 3	reject(p<0.001)	reject(p<0.001)	reject(p<0.001)	

Appendix B. Supplemental Regional Simulation

B.1 Variant 2 Regional Model

This appendix reproduces the following memo: Additional Variant of the Regional Scale Hydrogeology at Ceberg, L.J. Hartley, AEA Technology, November 1998.

This memo describes the regional model used to create boundary conditions for Variant Case 2. The memo is included without modification, except for deletion of figures and several minor edits to correct references to other reports.

B.1.1 Introduction

This note documents an additional variant on the regional groundwater flow at Ceberg performed on behalf of SKB as part of the SR 97 safety assessment project. All other SR 97 regional-scale groundwater flow calculations for Ceberg are detailed in Boghammar et al. (1997). The purpose of the variant is to assess the impact of several extra site-scale fracture zones and a high contrast in hydraulic conductivity between the fracture zones and the rock mass. The extra calculation is performed for the small regional model (GRS) only. The resulting pressure distribution has been used to set boundary conditions for an equivalent site-scale variant.

B.1.2 Alternative Conductive Features (GRSFX)

In the site characterisation report, Ahlbom et al. (1983) suggests that the intrusive dolerite and pegmatite dykes may be conductive features, with hydraulic conductivities similar to the deterministic fracture zones. This has been questioned in later reports, since such a characterisation cannot be unambiguously supported from the packer test data (Hermanson et al., 1997). Similarly, Ahlbom et al. (1983) and Askling (1997) have mapped an extensive topographic lineament running north-northwest to south-southeast at the eastern margins of the site, which may be a fracture zone. However, the existence of a fracture zone at this location cannot be unambiguously supported from the geophysical data (Hermanson et al., 1997). As part of SR 97, Saksa and Nummela (1998) re-evaluated the site-scale structural model and suggested that both the intrusive dykes and the topographic lineament might reasonably be interpreted as conductive fracture zones.

This variant case evaluates the possibility that the fracture zones, the intrusive dykes and the topographic lineaments are all highly conductive fracture zones. Similar to the GRSFH variant, these fractures are assumed to have a hydraulic conductivity 100 times that used in the Base Case.

Topographic head boundary conditions are used. Positions of the dykes and the regional lineament are taken from Saksa (personal communication, 1998) and are presented in Saksa and Nummela (1998). This variant is similar to that of SCD3, as suggested in Walker et al. (1997b), except that all the intrusive dykes are included, as is the regional lineament.

The pathlines are similar to the GRSFH variant, except a few paths now reach greater depths (1500 m). This is likely to be caused by the extra zones creating a larger recharge rate, which drives some flow paths deeper. The spatial distribution of discharge areas varies little from the GRSFH and is consistent with the Base Case (GRST), but there are none of the horizontally extensive paths that are seen in the GRST or GRSN Cases. A comparison of initial Darcy velocity and travel time for the GRSFX variant and the Base Case is constructed for a uniform array of 16 start points within the site region at $z = -350$ m. For six of the start positions, the Darcy velocity is 20–100 times larger in the GRSFX case than in the Base Case. The higher velocity is due to these paths starting within one of the site-scale fracture zones. The travel time for these paths is correspondingly shorter, some as low as 10–100 years. For the remaining start positions, the travel time is still on average about 1000 years, suggesting that the initial part of these paths is through the rock mass, causing an increase in the travel time.

B.2 Regional Model Mass Balance Calculations

Several sections of this report have discussed the mass balance of the regional model in terms of the net volumetric flow of water across the boundaries of site-scale domain, but Boghammar et al. (1997) did not document these quantities. The regional flows discussed in this study were provided in a series of personal communications and unpublished memos by Lee Hartley of AEA Technology. What follows is a summary of those memos and discussions describing the post-processing of NAMMU simulations to approximate the regional model flows across the site-scale HYDRASTAR domain for the Base (GRST), Variant 1 (GRSFH) and Variant 2 (GRSFZ) Cases.

The mass balance computations use the small-scale regional NAMMU model for the Gideå (GRS) to determine the net volumetric flows (m^3/s) through the six planar faces of a cube coincident with the boundaries of the site-scale model. The NAMMU code uses the finite element method of solving the governing equations for groundwater flow, a numerical method that inherently preserves mass balance over the element faces. In addition, NAMMU uses a direct solver, so that the solution to the system of equations is exact within the accuracy of the host platform. That is, regardless of the approximate mass balance over arbitrary subdomains, the finite element method and NAMMU's direct solver insure that mass balance is preserved and that the resulting simulated heads are correct (Cliffe et al, 1995).

However, the cube faces of the site-scale model do not necessarily coincide with element faces of the regional model. For this study, the regional flows over the site-scale domain were estimated by sampling the outward normal flux (specific discharge, m/s) at a regular grid of points on each face of the cube. The spacing of sample points was set at

10 m in the horizontal directions and 3 m in the vertical. The finite elements of the regional model are typically about 100 m on a side, so the sample points are close enough to resolve the variation in permeability and hence velocity with depth. The net volumetric flow out of each face was taken as the sum of pointwise fluxes at each sample, multiplied by the cross-sectional area (m^2) represented by each sampling point.

The sampling grid was refined until the calculated flows converged to a stable value, and mass balance residuals were computed for all three regional cases. These residuals reflect the sampling errors of this approximating method, and it is expected that a more rigorous approach (i.e., Gaussian quadrature within each element) would reduce this error dramatically. In addition, the mass balance is particularly poor for GRSFH and GRSFZ because groundwater velocity is very heterogeneous in these cases, reducing the accuracy of the approximation.

(Lee Hartley, personal communication, 1998).

Appendix C. Supplemental Calculations

C.1 Upscaling of Hydraulic Conductivity Model

C.1.1 Approach

The injection tests performed in the cored boreholes are the principal source of hydraulic conductivity data. These tests were interpreted and the measurements reported for various depths, rock types, etc. as described by Ahlbom et al. (1983). The interpreted hydraulic conductivities for the 25 m packer tests were taken directly from the SKB SICADA database and analysed with the SKB geostatistical inference code INFERENS.

The scale of these measurements (as inferred from the packer length) is much different from the proposed model grid scale. As discussed in Walker et al. (1997b) and Renard and de Marsily (1997), hydraulic conductivity is a scale-dependent parameter, which requires that the measured hydraulic conductivities be upscaled to the finite difference grid scale of the model. Thus, HYDRASTAR requires rescaling the geometric means of interpreted hydraulic conductivities found in SICADA. This study uses the scaling relationship provided in Rhén et al. (1997), which assumes that the geometric mean of hydraulic conductivity at the measurement scale, L_m, may be adjusted for scale using the regression equation:

$$Log_{10} K_{gu} = Log_{10} K_{gm} + 0.782(Log_{10} L_u - Log_{10} L_m)$$

where:

K_g = geometric mean of hydraulic conductivity (m/s)

L = length scale (m), assumed equal to the packer interval.

The subscripts *m* and *u* refer to the measurement and upscaled values, respectively. Rhén et al. (1997) developed this empirical scaling relationship using the 3 m, 30 m, 100 m packer tests and full-length tests in the same cored boreholes.

C.1.2 Base Case (35 m scale) Model

The inference of spatial correlation models for Ceberg site-scale hydraulic conductivity begins by dividing the domain into SRD, SCD and elevation zones. The elevation zones and SCD are treated as step changes in the mean of $\log_{10}$ conductivities, and a single variogram model is inferred for the entire domain (i.e., the same variogram for SRD and SCD). The Äspö scaling relationships of Rhén et al. (1997) are used to determine the geometric mean of hydraulic conductivity in each SRD and depth zone (Appendix C.1). The effect of upscaling on the variogram is determined by applying the Moye's formula-based regularisation algorithm and fitting a variogram–trend model via iterative generalised least squares estimation (IGLSE; see Neuman and Jacobsen, 1984) to the regularised data. The SKB program INFERENS, which includes the Moye's formula-based regularisation, automates the IGLSE fitting algorithm. Program restrictions of HYDRASTAR and INFERENS limit the geostatistical model to one variogram model for both domains. Because the majority of the 25 m packer tests fall in the SRD and these data yield a clearer variogram, the geostatistical model will be developed from the interpreted hydraulic conductivities in the SRD.

The Moye's formula-based regularisation has one additional restriction, in that it only works for regularisation scales that are multiples of the packer interval; e.g., 25 m data can be regularised to 50 m, 75 m, etc. for the Gideå data. That is, the regularisation imbedded in INFERENS cannot directly calculate a regularised value for the 35 m scale. As an indirect route, this study interpolates between the inferred models at 25 m and 50m scale to infer a model at the 35 m scale for the Base Case.

Walker et al. (1997b) explores the data and fits a model for the 25 m scale. An additional INFERENS calculation fitted a 50 m model for this study (Figure C-1). The sill and range parameters of 35 m model are determined by linear interpolation between the 25 and 50 m models (Table C-1). The effect of the upscaling is to decrease the total variance of the experimental variogram and to increase the practical range.

The geometric mean (K_g) at the 50 m scale are determined via the Äspö scale relationships. The resulting experimental and model variograms are shown in Figure 5.2-1, and the upscaled K_g are presented in Table 5.2-1.

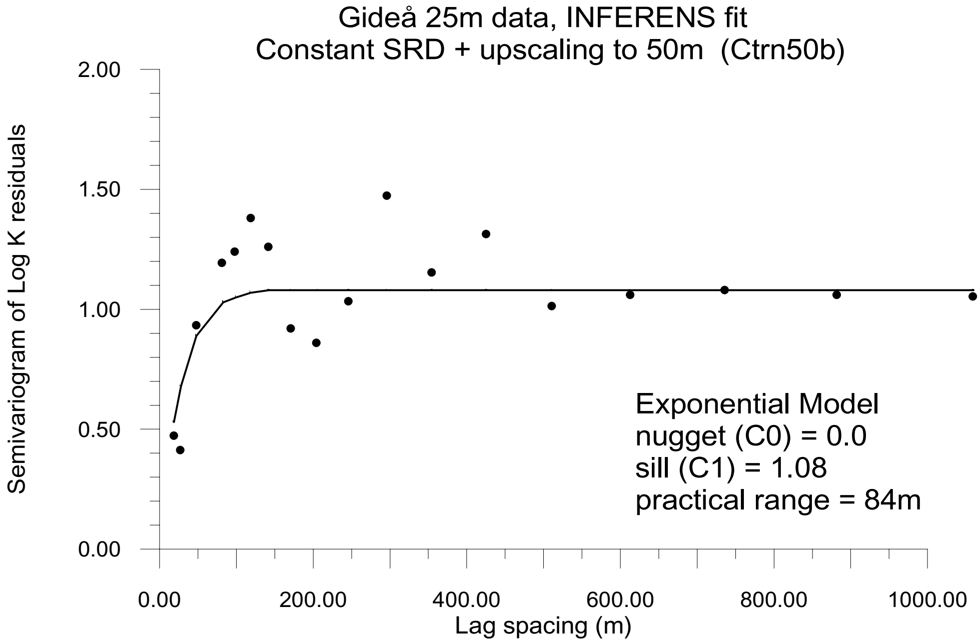

Figure C-1. *Semivariogram of Ceberg* $\log_{10}$ *hydraulic conductivity for rock domain. 25 m data regularised to 50 m and fitted via INFERENS.*

Table C-1 Inferred variogram models for Ceberg.

	25 m (Fitted)	35 m (Interpolated)	50 m (Fitted)
Nugget (C0)	0	0	0
Sill (C1)	1.15	1.12	1.08
Practical Range (m)	57	68	84

C.2 Scoping Calculation for Approximate Travel Times

The purpose of this section is to provide rough estimations of travel times to be used as check on the model results. It applies Darcy's law to a single travel path, with the hydraulic gradient roughly estimated from the observed water table.

C.2.1 Approach

The approach is to apply Darcy's Law and use the hydraulic gradient (∇h) and hydraulic conductivity (K) from various reports. The apparent velocity (V_a) is found by:

Darcy's Law: $V_a = K\nabla h$ (C.2.1)

The gradient is calculated by using the difference in water table divided by the horizontal distances between the release and the exit locations.

Hydraulic gradient: $\nabla h = \frac{h_{exit} - h_{start}}{Distance}$ (C.2.2)

The average particle velocity (V_{mean}) is given by dividing the apparent velocity (V_a) by the porosity ρ.

Average particle velocity: $V_{mean} = \frac{V_a}{\rho}$ (C.2.3)

The porosity is given a fixed value of ρ =1e–4 for all calculations. The travel times for the average particle is then given by

Travel times: $travel\,time = \frac{Travel\ length}{V_{mean}}$ (C.2.4)

C.2.2 Application

The gradient is difficult to estimate due to the complexity of the flow pattern. For this scoping calculation, we assumed that the hydraulic head at the starting position could be estimated as the water table elevation immediately above the starting position of interest. For head at the exit location, the water table elevation was used. For Ceberg, the water table elevations are taken from Figure 4-14, SKB TR 97-23.

The horizontal distances were measured at the map provided in Figure 4-14, SKB 97-23 with the block location found in SKB R-97-09. The values for the hydraulic conductivity used are taken from Walker et al (1997b). Two paths are considered:

- Path one: Start point in east part of block 2 at depth 500 m, through rock mass following a straight line to the exit point in Husån, 1.8 km east of the start point.

- Path two: Start point in south part of block 2 at depth 500 m, through rock mass following a straight line to the exit point in Gideälven, 2.1 km SSE of the start point.

Table C-2 presents the resulting travel times. For the effective conductivity (K_{100}), the results range from 1200 to 1500 years.

Table C-2. Travel paths considered.

Path 1				
Hydraulic Gradient		0.01944444		
Rock mass	Travel length	Log$_{10}$ K_{25}	Log$_{10}$ K_{35}	Log$_{10}$ K_{100}
0–200 m	633	–8.26	–8.14	–7.87
200 m<	1266	–10.14	–10.03	–9.745
Travel Times	Log$_{10}$ K_{25}	Log$_{10}$ K_{35}	Log$_{10}$ K_{100}	
0–200 m	18.7845832	14.2495636	7.65246873	
200 m<	2849.91272	2212.23653	1147.7084	
Total (years)	2868.6973	2226 yr	**1155 yr**	
Path 2				
Hydraulic Gradient		0.01761905		
Rock mass	Travel length	Log$_{10}$ K_{25}	Log$_{10}$ K_{35}	Log$_{10}$$K_{100}$
0–200 m	728	–8.26	–8.14	–7.87
200 m<	1456	–10.14	–10.03	–9.745
Travel Times	Log$_{10}$ K_{25}	Log$_{10}$ K_{35}	Log$_{10}$ K_{100}	
0–200 m	23.8419813	18.0859924	9.71275297	
200 m<	3617.19847	2807.83988	1456.70744	
Total (years)	3641.04045	2826 yr	**1466 yr**	

Appendix D. Summary of Input Parameters

Mechanisms and model parameters considered in this study when modelling groundwater flow using HYDRASTAR.

Mechanism	HYDRASTAR model parameter		Source
	Symbol (unit)	**Description**	
Topographically driven flow	—	Fracture zone and rock domain geometries	Based on the interpreted geologic structural model for the site, R 97-05. Variant 2 model from Saksa and Nummela, TR 98-12.
	T (m^2/s)	Fracture zone transmissivities	Based on the interpreted geohydrological model for the site, TR 97-23. 25 m injection tests rescaled as described in Section 3.0
	K (m/s)	Rock mass hydraulic conductivity	Based on the interpreted geohydrological model for the site (TR 97-23) and single-hole water injection tests on 25 m scale. These tests are the basis for geostatistical analysis. Upscaling as described in Section 3.0. See Appendix C.
		Variant 1, 2, 3, 4.	Alternative interpretation of K distribution / contrast / statistical models. See Appendix C.
	S_s (m^{-1})	Specific storativity. Necessary for transient simulations.	Not used
	—	Top boundary condition	Constant head, as provided from Boghammar, 1998. See Append. C. Files: tbcsta.bcs
	—	Vertical/lower boundary conditions	Constant head, as provided from Boghammar, 1998. See Append. B. Files: tbcsta.bcs
	—		Variant 1: See Appendix B. Files: tbcsfn.bcs
	ε_f (–)	Flow porosity Necessary for travel time calculation, but is poorly known in general	From TR 97-23, uniform throughout model
Thermally and/or salinity driven flow	ρ (kg/m^3)	Groundwater density	Constant density.
Repository	Tunnel Layout		Single level layout from R 97-09, Figure 6-39. File: c_koord.xls
	Canister Locations		119 representative starting positions, spread uniformly over the tunnels given in R 97-09 (see Section 3.0)
	EDZ / Backfill K (m/s)		No / 10^{-10} m/s, based on SKB AR D-96-011
Model Domain			

Appendix E. Data Sources

The input data consist of coordinates for fracture zones, deposition tunnels, and boundary conditions.

E.1 SICADA Logfile for Coordinates and 25 m Interpreted K Values

```
Date :970411 14:54:47

Tables :sic_dba.transient_inj_cd

Columns :transient_inj_cd.idcode, transient_inj_cd.seclen, transient_inj_cd.secup,

Criteria: (transient_inj_cd.idcode >='KGI01' AND

transient_inj_cd.idcode <='KGI13') AND transient_inj_cd.seclen =25

Result: 309 rows written

Filename: gi_tr.csv

Fileformat: csv

Coordinate system: RT

Coordinate calculation column: secup
```

E.2 SICADA Logfile for Coordinates, 2 m and 3 m Interpreted K Values

```
Output to: File

--------------------

Date :970423 15:47:22

Table(s) :sic_dba.steady_state_inj_cd

Columns: steady_state_inj_cd.idcode, steady_state_inj_cd.start_date, steady_state_inj_cd.seclen, steady_state_inj_cd.secup,
steady_state_inj_cd.k, steady_state_inj_cd.comment, steady_state_inj_cd.midpoint,

New column: midpoint=secup+seclen/2

Criteria: (steady_state_inj_cd.idcode='KGI07'OR steady_state_inj_cd.idcode='KGI09' OR
```

```
steady_state_inj_cd.idcode ='KGI11') AND (steady_state_inj_cd.seclen =2 OR

steady_state_inj_cd.seclen =3)

Result : 225 rows written to file.

Coordinate calculations done.

Coordinate system : RT

Coordinate calculation column: secup

Filename : /home/skbee/gi_secup.csv

File format : csv

Output to: File

--------------------

Date :970423 15:48:40

Table(s) :sic_dba.steady_state_inj_cd

Columns: steady_state_inj_cd.idcode, steady_state_inj_cd.start_date, steady_state_inj_cd.seclen, steady_state_inj_cd.secup,
steady_state_inj_cd.k, steady_state_inj_cd.comment, steady_state_inj_cd.midpoint,

New column: midpoint=secup+seclen/2

Criteria:(steady_state_inj_cd.idcode='KGI07'OR steady_state_inj_cd.idcode ='KGI09' OR

steady_state_inj_cd.idcode ='KGI11') AND (steady_state_inj_cd.seclen =2 OR

steady_state_inj_cd.seclen =3)

Result : 225 rows written to file.

Coordinate calculations done.

Coordinate system : RT

Coordinate calculation column: midpoint

Filename : /home/skbee/gi_mid.csv

File format : csv
```

E.3 Structural Data

Coordinates for the fracture zones were received April 10 1997 from Golder Associates in a file called zonecoord.xls. The information was transformed and checked with SKB R-97-05. The hydraulic properties of the fracture zones and rock mass were obtained from Walker et al. (1997b).

E.4 Repository Lay-out

The data used in the final layout of the repository were received from Munier, SCC. The data for Ceberg were submitted in two files, c_koord.xls and kapkoord.xls. The file c_ koord.xls contains tunnel coordinates for a layout based on structures and the file kapkoord.xls contains canister positions. The latter file was used to check that all the positions fall into the designed tunnels. (See Figure 3-4.2).

File	**Main contents here**	**Date received**	**Source**
C_koord.xls	Tunnel coordinates	April 16 1998	Munier, SCC
Kapkoord.xls	Canister positions	April 16 1998	Munier, SCC

E.5 Boundary Conditions

Three sets of boundary conditions were obtained from Hartley, AEA Technlogy, UK. The approach used in the regional modelling is described in Boghammar et al. (1997). The different sets correspond to the Base Case, Variant 1 (increased contrast in conductivity fracture zones vs. rock mass) and Variant 2 (additional structures). Variant 3 (other geostatistical parameters) and 4 (deterministic case) were using the same boundary conditions as the Base Case. (Table E-5.1).

The path to the boundary conditions from NAMMU on the SUN machines is:

/opt/src/nammu/2119sr97/ceberg/grs/nam/bcs

Table E-5.1. Boundary condition file deliveries.

Case	Files	Main Contents	Date received	Source
Base	tbcsta.bcs	Pressure, [Pa]	March 19 1998	Hartley, AEA
Variant 1	tbcsfh.bcs	Pressure, [Pa]	March 20 1998	Hartley, AEA
Variant 2	tbcsv2.bcs	Pressure, [Pa]	April 1998	Hartley, AEA

E.6 File Locations

The following input files and simulation results are located within the following directories on the SKB Convex or on the SKB SUN machines. The path on Convex starts with

/slow/s92/tmp-hyd/ceberg

or on the SUN machines (e.g. sultan):

/net/s92/export/home/tmp-hyd/ceberg

In each directory, there is a file with a short description of the performed simulations in addition to the necessary files for HYDRASTAR and result files:

README.txt	Description of the problem

The necessary HYDRASTAR files and results may be found at:

cbas/	Base Case with unconditional stochastic simulations, HYDRABOOT
cvar1/	Variant 1, Fracture zone contrast
cvar2/	Variant 2, Additional fracture zone
cvar3/	Variant 3, Geostatistical parameters
determ/	Variant 4, Deterministic calculations
holes/	Borehole information

Appendix F. Additional Software Tools

INFERENS (Norman, 1992b; Geier, 1993). INFERENS is a FORTRAN program developed by SKB that incorporates the HYDRASTAR regularisation algorithm and Universal Kriging via iterative generalised least squares estimation (IGLSE). It is necessary in this study because each of the sites in SR 97 divides the model domain into a series of fracture zones, rock masses and depth zones that represent stepwise changes in the hydraulic conductivity. HYDRASTAR represents this complex hydraulic conductivity field as a multivariate lognormal regionalised variable with local trends in $\log_{10}$ hydraulic conductivity. A single variogram model is inferred for the entire domain (i.e., the same variogram for SRD, SCD, etc.). Although not a restriction of HYDRASTAR itself, this study will consider the trends as constants within well-defined volumes in the domain (0 order trends in $\log_{10} K_b$). This complex model of trend and spatial correlation violates the assumptions of ordinary least squares estimation (i.e., fitting trends by simple least squares regression). This study instead uses the more versatile IGLSE for universal kriging suggested by Neuman and Jacobsen (1984). INFERENS is an SKB computer program for geostatistical inference that automates the IGLSE fitting and data exploration (Norman, 1992b). INFERENS is unique in that it includes the same regularisation algorithm as HYDRASTAR to upscale the data and apply universal kriging. Thus the resulting model of trends and variogram are compatible with the conditioning data and the chosen grid scale.

A program limitation prohibited using the crossvalidation option in INFERENS for this study. Alternative methods that met QA standards were not readily available during this study; therefore, crossvalidation was omitted.

HYDRAVIS (Hultman, 1997) HYDRAVIS is a graphical post-processor for HYDRASTAR, permitting users to view the repository layout, deterministic zones, hydraulic conductivities, stream tubes, and hydraulic heads. HYDRAVIS is an Advanced Visual Systems (AVS) system 5 application module developed by Cap Gemeni under contract to SKB. HYDRAVIS scans the HYDRASTAR input <casename>.hyd file and the output files for the required information, which is then displayed in a GUI format for the user. The system runs under Sun/OS, and requires a compatible version of AVS to be available. (AVS is a commercial software package for scientific visualisation on Windows NT and UNIX platforms.)

IGOR Pro (WaveMetrics) IGOR Pro is a commercial Mac and MS/Windows package used in this study to produce exit location plots, some of the floating histograms, and special plots; e.g., for studying single realisations and single starting positions. IGOR Pro is an interactive programmable environment for data analysis and plotting. It handles large data sets (more than 100,000 points) and it includes a wide range of capabilities for analysis and graphing.

MATLAB (MathWorks) MATLAB is a commercial software package for numerical computation, visualisation and programming. It supplies a large number of high-level mathematical operations that are convenient for data analysis and visualisation. In this study, several MATLAB programs are used to post-process HYDRASTAR results, e.g., displays of boundary conditions, smoothing window statistics for floating histograms for subsequent display in Excel, etc. These programs include the following:

GENERAL SCRIPTS FOR PRE-PROCESSING TO THE STATISTICA PACKAGE:

Path: 2149ac\matlab

`layerabc.m`	These files start up and run the GUI in **`MATLAB`**.
`layerfunc.m`	Reads the input data files and generates *`casename.nim`*. The definitions of layers and end point areas are also made here as well as the definition of the string variable `'HomeDir'`. This string must be adjusted to match the installation path of the **`MATLAB`** files.
`perfm.m`	Calculates the performance measures for the entire data file as well as for separate canisters (defined here) and layers or end point areas (depending on which model domain is being studied).
`perfmout.m`	Generates a text file called *`casename_s.txt`* containing performance measures for the entire data file and the chosen canisters.
`perfplot.m`	Draws graphs of accumulated mean and median (including standard deviation) of $\log_{10}$ (TT) and $\log_{10}$ (CF) for each one of the three canisters selected and also scatter plots for the three canisters.
c_out.m	Generates text files containing performance measures for the different end point areas of path lines in Ceberg. They are given the names *CebergX.txt* where *X* is the number of the end point area.

Scripts for visualisation of boundary conditions (*Path:* 2149ac\ceberg\bc):

rand_c.m	Creates a figure containing the boundary conditions of Ceberg visualised as six sides of an opened box.
boxplot.m	Creates two figures containing the boundary conditions of Ceberg visualised as boxes showed from different angles. This file is a subroutine used by rand_c.m.
cntrl_1.m	Function used by boxplot.m.
cntrl_2.m	Function used by boxplot.m.

Statistica (StatSoft) Statistica is commercial MS/Windows software package that performs general statistical analysis of data. One of its strengths is a macro scripting language that allows users to automate a series of sorting, analysis and plotting operations. Under contract to SKB, Kemakta has developed scripts that translate HYDRASTAR output and compute summary statistics of the simulation results. The first script, statistica.pl, is a Perl script that scans and extracts the raw HYDRASTAR travel time and canister flux files and organises them into a format for Statistica input. A second Perl script, endpoints.pl, extracts the exit locations from the HYDRASTAR travel path files. A Statistica Basic program, Hydrast_.STB, is a Statistica Basic program that acts as a macro for the Statistica GUI. Optional outputs include tables of summary statistics, histograms, and box plots of canister fluxes, travel time and F-ratio. This study uses Statistica version 5.1 and the scripts documented in Boghammar and Marsic (1997). Marsic (1999) updated the script Hydrasta_.STB for use in this study. Additional statistical post-processing was provided by MATLAB.

TRAZON

This program is a modification of HYDRASTAR 1.7.2 that helps identify the canister locations versus the deterministic zones. It reads the HYDRASTAR input <casename>.hyd file and compares the stream tube starting position versus the ZONE and XALFA definitions. If the starting position falls within a defined ZONE or XALFA, a comment is written to the logfile. This feature is intended to be included as an option in future versions of HYDRASTAR.

Appendix G. HYDRASTAR Input file for Base Case

```
# AVS
#-----------------------------------------------------------
#
#  NAME: cbas.hyd
#  DESC: Deterministic case  HYDRASTAR LOCAL
CEBERG MODEL
#  DATE: 980227
#  USER: BJORN GYLLING, KEMAKTA
#
#  VERSION: HS 1.7.1
#
#-----------------------------------------------------------
#
SYSTEM SAVE_SCRATCH_FILES
SYSTEM IGNORE_ERRORS
#SYSTEM SKIP_USER_INTERFACE
#SYSTEM VERBOSE
#
#
BEGIN_BLOCK COVARIANCE
# DETERMINISTIC   YES
#SPHERIVAL MODEL
#EXPONENTIAL MODEL
 VARIANCE      1.12
# NUGGET_VARIANCE 0.5
# VARIANCE      1.7
#
# RANGE         -117.
 RANGE          -22.67
BEGIN_DEF   ANISOTROPY
   KXX      1.0
   KXY      0.0
   KXZ      0.0
   KYY      1.0
   KYZ      0.0
   KZZ      1.0
 END_DEF
 RELATIVE_TOL   1.0E-02
 NUM_ICOSAHEDRON 40
 NUM_LINES      0
 ORIGIN         0.0 0.0 0.0
 MUL_FACTOR     0.2
 TRUNCATION     999.
END_BLOCK
#
BEGIN_BLOCK GEOM
#
# 34 METER BLOCK SCALE
# NAMMU BC
#
# AXISLENGTH     3000. 2200. 1200.
# AXISLENGTH     5202 5610. 1190.
 AXISLENGTH     6510 4290. 1190.
# 35 m block scale
 NUMBER_OF_NODES  187 124  35
 BOUNDARY       NAMMU
#  BOUNDARY       SIMPLE #
[SIMPLE,NOFLOW,NAMMU,HYRV11]
#  GRADIENT       -1.0  0.0  0.0
#  LEVEL          10.0
#
```

```
#
 BEGIN_DEF USER_SYSTEM
  XY_ROTATE  344.524
  ZY_ROTATE  0.
#Top surface at 60 m above sea level
  TRANSLATE  10111  14020 -1130
  SYSTEM RIGHT
 END_DEF
  BEGIN_DEF WORLD_SYSTEM
   XY_ROTATE   344.524
   ZY_ROTATE  0.0
  TRANSLATE  10111  14020 -1130
  SYSTEM RIGHT
 END_DEF
END_BLOCK
#
#
BEGIN_BLOCK KRGE_NBH
  BEGIN_DEF SECONDARY
    NORMAL      0.  0. 1.
    WIDTH       3000.0
    OVERLAP     50.0
    MEASUREMENTS 16
  END_DEF
END_BLOCK
#
#
#
BEGIN_BLOCK KRIGE
  NUM_ITERATIONS  60
#  NUM_ITERATIONS  200
  RESIDUAL_TOL   1.0E-02
  METHOD         CG
  RESTART
  PATH           .
END_BLOCK
#
#
#
BEGIN_BLOCK HYDROLOGY_EQ
  NUM_ITERATIONS  16000
  RESIDUAL_TOL   1.0E-09
  PRECOND        DIAGONAL
END_BLOCK
#
BEGIN_BLOCK TRANSPORT
  TRANSPORT_MODEL STREAM
  PLOT_TIMES     1
  BACK_INTERPOL  NOBACKINT
  INTERVALS      FIXED
  DELIMITERS
                1.0
                10.0
                100.0
                1000.0
  END_LIST
#  BEGIN_DEF EXTERNAL
#   NEIGHBOURS 2
#   SCALE      NOSCALING
#   VEL1DIST   40.0
#  END_DEF
  LOGON
  TOLERANCE      0.2
  PRESENTATION   0.0
```

```
  CELL_SHIFTS     1024
  PLOTTING_MOMENTS 1.0E5
  STREAM_TUBES    119
  DIVISION        SPATIAL
  VIEW            ALL
END_BLOCK
#
BEGIN_BLOCK RESULT_ESTIMATION
   PERIOD          1
   SAVE_TRANSPORT   TRANSPORT
END_BLOCK
#
BEGIN_BLOCK PRESENTATION
   POST_PROCESSOR    AVS
   VIEW              ZDIR
   PRESENT           ALL
   NUM_REALIZATIONS
     1
   END_LIST
   INTERACTIVE      NO
   MODEL_NAME       FAA

   BEGIN_DEF PSLICE
     NORMAL        0. 0. -1.
     DISTANCE      1üâ€
à €€

à v$€
                              TYPE UPPER
END_DEF
#                    14120.26583          15071.67812
             0
#                    14128.58185          15055.66401
             0
#                    14046.19069          15012.87885
             -37.16351311
#                    14128.58185          15055.66401
             0
#                    14136.89787          15039.6499
             0
BEGIN_DEF ZONE
             NAME Z45 #GL11B2
             ALFA -9.61
             BETA 0
             TEST_POINT          14272.94466
           15081.30339          -133.329834
             PLANE Q43 #GL11B2_U        # Distance to
testpoint = -17.49987642
             PLANE Q44 #GL11B2_L        # Distance to
testpoint = 17.50012358
             PLANE Q45 #GL11A1_V        # Distance to
testpoint = -80.36199087
             PLANE Q41 #GL11B2_V        # Distance to
testpoint = -88.66774176
             P_TYPE UPPER
END_DEF
# Start defining fracture Z46 #GL12-----------------------------
---------------------------------------
BEGIN_DEF PLANE
             NAME Q46 #GL12_U
             EQUATION            -0.595061183
           0.801065505          0.064778432            -
4307.625488
             TYPE UPPER
END_DEF
#                    13757.21834          15666.11585
             8.281590154
#                    13837.32489          15725.62197
             1.803746929
#                    13777.81877          15805.72852
             8.281590154
```

```
#                    13837.32489          15725.62197
             1.803746929
#                    13917.43144          15785.12809
             8.281590154
BEGIN_DEF PLANE
             NAME Q47 #GL12_L
             EQUATION            -0.595061183
           0.801065505          0.064778432            -
4272.625488
             TYPE LOWER
END_DEF
#                    13736.39119          15694.15314
             10.54883528
#                    13816.49775          15753.65926
             4.070992058
#                    13756.99163          15833.76581
             10.54883528
#                    13816.49775          15753.65926
             4.070992058
#                    13896.6043           15813.16538
             10.54883528
BEGIN_DEF PLANE
             NAME Q48 #GL04e
             EQUATION            0.072161004            -
0.994844139          -0.071259439          14796.99219
             TYPE LOWER
END_DEF
#                    14120.26583          15071.67812
             0
#                    14128.58185          15055.66401
             0
#                    14046.19069          15012.87885
             -37.16351311
#                    14128.58185          15055.66401
             0
#                    14136.89787          15039.6499
             0
BEGIN_DEF PLANE
             NAME Q49 #F11
             EQUATION            -0.856527209           -
0.516063869          0.00626401           19557.61719
             TYPE UPPER
END_DEF
#                    14345.12404          15127.6863
             0
#                    14350.66565          15110.98114
             0
#                    14255.83643          15079.52338
             -4.222290712
#                    14350.66565          15110.98114
             0
#                    14356.20727          15094.27598
             0
BEGIN_DEF ZONE
             NAME Z46 #GL12
             ALFA -9.61
             BETA 0
             TEST_POINT          13853.89429
           15703.31641          -700
             PLANE Q46 #GL12_U            # Distance to
testpoint = -17.50003407
             PLANE Q47 #GL12_L            # Distance to
testpoint = 17.49996593
             PLANE Q48 #GL04e             # Distance to
testpoint = 224.2324314
             PLANE Q49 #F11    # Distance to testpoint =
           -416.919252
END_DEF
# Start defining fracture Z47 #GR05b---------------------------
----------------------------------------
BEGIN_DEF PLANE
             NAME Q50 #GR05b_U
```

```
        EQUATION        0.87014246
      0.492800236       0       -21235.6543
        TYPE UPPER
END_DEF
#               16249.49272     14328.89184
      0
#               16298.77275     14241.8776
      0
#               16385.78699     14291.15762
      0
#               16298.77275     14241.8776
      0
#               16348.05277     14154.86335
      0
BEGIN_DEF PLANE
        NAME Q51 #GR05b_L
        EQUATION        0.87014246
      0.492800236       0       -21200.6543
        TYPE LOWER
END_DEF
#               16279.94771     14346.13985
      0
#               16329.22773     14259.1256
      0
#               16416.24198     14308.40563
      0
#               16329.22773     14259.1256
      0
#               16378.50776     14172.11136
      0
BEGIN_DEF PLANE
        NAME Q52 #GR05a_V
        EQUATION        -0.285761391
      0.958300802       0       -7546.57515
        TYPE LOWER
END_DEF
#               17063.20533     12963.13267
      0
#               17045.99944     12958.00194
      0
#               17017.4233      13053.83202
      0
#               17045.99944     12958.00194
      0
#               17028.79355     12952.87121
      0
BEGIN_DEF PLANE
        NAME Q53 #F12
        EQUATION        -0.901027381
      0.433762193       0       7297.842773
        TYPE UPPER
END_DEF
#               14345.12404     15127.6863
      0
#               14350.66565     15110.98114
      0
#               14255.83643     15079.52338
      -4.222290712
#               14350.66565     15110.98114
      0
#               14356.20727     15094.27598
      0
BEGIN_DEF ZONE
        NAME Z47 #GR05b
        ALFA -9.61
        BETA 0
        TEST_POINT      16314   14250.50146
      -700
        PLANE Q50 #GR05b_U      # Distance to
testpoint = -17.49972516
        PLANE Q51 #GR05b_L      # Distance to
testpoint = 17.50027484
```

```
        PLANE Q52 #GR05a_V      # Distance to
testpoint = 1447.78051
        PLANE Q53 #F12  # Distance to testpoint =
      -1220.189164
END_DEF
# Start defining fracture Z48 #GR14a---------------------------
-----------------------------------------
BEGIN_DEF PLANE
        NAME Q54 #GR14a_U
        EQUATION        0.97285372
      0.231420875       0       -13868.23242
        TYPE UPPER
END_DEF
#               10474.11329     15743.83659
      0
#               10497.25538     15646.55122
      0
#               10594.54075     15669.69331
      0
#               10497.25538     15646.55122
      0
#               10520.39747     15549.26585
      0
BEGIN_DEF PLANE
        NAME Q55 #GR14a_L
        EQUATION        0.97285372
      0.231420875       0       -13833.23242
        TYPE LOWER
END_DEF
#               10508.16317     15751.93632
      0
#               10531.30526     15654.65095
      0
#               10628.59063     15677.79304
      0
#               10531.30526     15654.65095
      0
#               10554.44735     15557.36558
      0
BEGIN_DEF PLANE
        NAME Q56 #GR15b
        EQUATION        -0.266835183    -
0.963742197     0       16286.76074
        TYPE UPPER
END_DEF
#               17063.20533     12963.13267
      0
#               17045.99944     12958.00194
      0
#               17017.4233      13053.83202
      0
#               17045.99944     12958.00194
      0
#               17028.79355     12952.87121
      0
BEGIN_DEF PLANE
        NAME Q57 #GR40a_V
        EQUATION        0.237961405     -
0.971274611     0       14528.07994
        TYPE LOWER
END_DEF
#               10073.9946      17425.86665
      0
#               10090.99229     17430.03107
      0
#               10114.78843     17332.90361
      0
#               10090.99229     17430.03107
      0
#               10107.98998     17434.19549
      0
BEGIN_DEF ZONE
```

```
            NAME Z48 #GR14a
            ALFA -9.61
            BETA 0
            TEST_POINT        10514.28027
          15650.60107         -700
            PLANE Q54 #GR14a_U          # Distance to
testpoint = -17.49995422
            PLANE Q55 #GR14a_L          # Distance to
testpoint = 17.50004578
            PLANE Q56 #GR15b            # Distance to
testpoint = -1601.963814
            PLANE Q57 #GR40a_V          # Distance to
testpoint = 1829.041384
END_DEF
# Start defining fracture Z49 #GR15b--------------------------
----------------------------------------
BEGIN_DEF PLANE
            NAME Q58 #GR15b_U
            EQUATION          -0.266835183           -
0.963742197       0           16269.26074
            TYPE UPPER
END_DEF
#                 12613.86386         13425.20622
          0
#                 12517.48964         13451.88974
          0
#                 12490.80612         13355.51552
          0
#                 12517.48964         13451.88974
          0
#                 12421.11542         13478.57326
          0
BEGIN_DEF PLANE
            NAME Q59 #GR15b_L
            EQUATION          -0.266835183           -
0.963742197       0           16304.26074
            TYPE LOWER
END_DEF
#                 12604.52463         13391.47524
          0
#                 12508.15041         13418.15876
          0
#                 12481.46689         13321.78454
          0
#                 12508.15041         13418.15876
          0
#                 12411.77619         13444.84228
          0
BEGIN_DEF PLANE
            NAME Q60 #GR05a
            EQUATION          0.997933686
          0.064252369         0           -17843.35938
            TYPE UPPER
END_DEF
#                 17063.20533         12963.13267
          0
#                 17045.99944         12958.00194
          0
#                 17017.4233          13053.83202
          0
#                 17045.99944         12958.00194
          0
#                 17028.79355         12952.87121
          0
BEGIN_DEF PLANE
            NAME Q61 #GR15a_V
            EQUATION          0.936133433            -
0.351644985       0           -2251.578187
            TYPE LOWER
END_DEF
#                 7922.456069         14687.81877
          0
#                 7928.63443          14704.26653
          0
#                 8022.247773         14669.10203
          0
#                 7928.63443          14704.26653
          0
#                 7934.812791         14720.71428
          0
BEGIN_DEF ZONE
            NAME Z49 #GR15b
            ALFA -9.61
            BETA 0
            TEST_POINT        12512.82007
          13435.02441         -700
            PLANE Q58 #GR15b_U          # Distance to
testpoint = -17.49982906
            PLANE Q59 #GR15b_L          # Distance to
testpoint = 17.50017094
            PLANE Q60 #GR05a            # Distance to
testpoint = -4493.162577
            PLANE Q61 #GR15a_V          # Distance to
testpoint = 4737.732064
END_DEF
# Start defining fracture Z50 #GR79-GL07--------------------
----------------------------------------------
BEGIN_DEF PLANE
            NAME Q62 #GR79-GL07_U
            EQUATION          0.87871033
          0.422993124         0.221235037            -
17899.57422
            TYPE UPPER
END_DEF
#                 14572.07708         12678.56338
          52.51332888
#                 14614.3764          12590.69234
          30.38982519
#                 14702.24743         12632.99166
          52.51332888
#                 14614.3764          12590.69234
          30.38982519
#                 14656.67571         12502.82131
          52.51332888
BEGIN_DEF PLANE
            NAME Q63 #GR79-GL07_L
            EQUATION          0.87871033
          0.422993124         0.221235037            -
17864.57422
            TYPE LOWER
END_DEF
#                 14602.83195         12693.36814
          60.2565553
#                 14645.13126         12605.4971
          38.13305161
#                 14733.00229         12647.79642
          60.2565553
#                 14645.13126         12605.4971
          38.13305161
#                 14687.43057         12517.62607
          60.2565553
BEGIN_DEF PLANE
            NAME Q64 #F16
            EQUATION          0.869803071            -
0.493399024       0           -8405.542969
            TYPE UPPER
END_DEF
#                 7922.456069         14687.81877
          0
#                 7928.63443          14704.26653
          0
#                 8022.247773         14669.10203
          0
```

```
#                       7928.63443              14704.26653
        0
#                       7934.812791             14720.71428
        0
BEGIN_DEF ZONE
        NAME Z50 #GR79-GL07
        ALFA -9.61
        BETA 0
        TEST_POINT         14493.67285
      12532.58813            -700
        PLANE Q62 #GR79-GL07_U   # Distance to
testpoint = -17.50009595
        PLANE Q63 #GR79-GL07_L   # Distance to
testpoint = 17.49990405
        PLANE Q04 #GR79-GL07_V   # Distance to
testpoint = -2364.29083
        P_TYPE UPPER
        PLANE Q64 #F16    # Distance to testpoint =
      -1982.468566
END_DEF
#
# End New struct 980422
# Assign mean conductivity at 4 different depths for rock
mass
#
BEGIN_DEF PLANE
   NAME R1
   EQUATION 0.0 0.0 1.0 -100.0
   TYPE UPPER
END_DEF
BEGIN_DEF PLANE
   NAME R2
   EQUATION 0.0 0.0 1.0 0.0
   TYPE LOWER
END_DEF
BEGIN_DEF ZONE
   NAME S1
   ALFA -7.44
   BETA 0.0
   PLANE R1
   PLANE R2
   TEST_POINT 13369. 15210. 10.
END_DEF
BEGIN_DEF PLANE
   NAME R3
   EQUATION 0.0 0.0 1.0 100.0
   TYPE LOWER
END_DEF
BEGIN_DEF ZONE
   NAME S2
   ALFA -8.92
   BETA 0.0
   PLANE R2
   P_TYPE UPPER
   PLANE R3
   TEST_POINT 13369. 15210. -10.
END_DEF
BEGIN_DEF PLANE
   NAME R4
   EQUATION 0.0 0.0 1.0 300.0
   TYPE LOWER
END_DEF
BEGIN_DEF ZONE
   NAME S3
   ALFA -9.91
   BETA 0.0
   PLANE R3
   P_TYPE UPPER
   PLANE R4
   TEST_POINT 13369. 15210. -200.
END_DEF
BEGIN_DEF PLANE
   NAME R5
   EQUATION 0.0 0.0 1.0 1500.0
   TYPE LOWER
END_DEF
BEGIN_DEF ZONE
   NAME S4
   ALFA -10.14
   BETA 0.0
   PLANE R4
   P_TYPE UPPER
   PLANE R5
   TEST_POINT 13369. 15210. -400.
END_DEF
END_BLOCKüâ€
à €€

à €€
       à €€
```

Appendix H. Coordinate Transforms

The Ceberg simulations use a local coordinate system based on a translation (off-set) of the Swedish National grid (the RAK system). This means that all input data in the form of e.g. stream tube starting positions and fracture zones must be defined for the local system. The model is set up in the local system with the origin for the model cube at (10111, 14020, -1190). The HYDRASTAR modelling terms “user system” and “world system” are defined using that point in the local system. The HYDRASTAR “cube system” is rotated 15.48 degrees clock-wise in relation to the local system. The used definitions of coordinate systems give output data for e.g. exit locations, which could be extracted from the lines_<real>.hyp files, in the local system (that is, the rotation of the cube system is made internally in HYDRASTAR).

The Ceberg local coordinate system used in the groundwater simulations uses a translation of 1,650,000 m and 7,030,000 m from RAK grid coordinates, in east and north, respectively (Boghammar et al., 1997). The coordinate systems for Ceberg are right-hand-rule with X towards east and Y towards north. The Z-direction is given in metres above sea level (masl). To translate the modelling coordinates to RAK, the following equations have been used:

$X_{RAK} = X_{Off\text{-}set} + X_C$

$Y_{RAK} = Y_{Off\text{-}set} + Y_C$

where X_{RAK} and Y_{RAK} stand for east and north, respectively; X_C and Y_C are Ceberg modelling coordinates; $X_{Off\text{-}set} = 1\ 650\ 000$; and $Y_{Off\text{-}set} = 7\ 030\ 000$.